Surface Science Reports 13 (1991) 1–72
North-Holland

A review of theoretical models of adsorption, diffusion, desorption, and reaction of gases on metal surfaces

Stephen J. Lombardo and Alexis T. Bell

Center for Advanced Materials, Lawrence Berkeley Laboratory, and Department of Chemical Engineering, University of California, Berkeley, CA 94720, USA

Manuscript received in final form 20 March 1991

A review is presented of the theoretical approaches available for describing the kinetics of gas adsorption, diffusion, desorption, and reaction on metal surfaces. The prediction of rate and diffusion coefficients based on molecular dynamics, transition-state theory, stochastic diffusion theory, and quantum mechanics is discussed, and the success of these theoretical approaches in representing experimental observation is examined. Consideration is also given to the effects of lateral interactions between adsorbates and to the ability of lattice-gas models to provide a representation of the dependences of rate and diffusion coefficients on adsorbate coverage. Finally, the utility of continuum and Monte Carlo models for describing the kinetics of complex surface processes in terms of elementary processes is addressed.

1. Introduction

The kinetics of chemical reactions occurring on the surfaces of metals is of continuing interest to researchers working in the areas of catalysis, chemical vapor deposition, etching, and corrosion. While it has been known for some time that the kinetics of such reactions depend on the properties of the metal, as well as those of the adsorbed reactants, intermediates and products, it has only been in the past two decades that it has become possible to understand the dynamics of surface reactions at the atomic and molecular level. Progress has come through careful experimental measurements of the rates of elementary processes such as adsorption, diffusion, desorption, and reaction, and through the development of theoretical methods for predicting the dynamics of such processes. Theoretical studies have also proven useful for interpreting the experimentally observed effects of surface composition/structure and adsorbate coverage on rate and diffusion coefficients, and for describing the kinetics of complex surface processes in terms of a sequence of elementary steps. It is therefore timely to examine the current state of the art of theoretical methods for predicting rate and diffusion coefficients for elementary processes occurring on metal surfaces and the extent to which mechanistic models are successful in representing the overall kinetics of complex surface processes (e.g., catalysis).

Previous reviews on the subjects of adsorption [1–4], surface diffusion [5–8], desorption [1–3,9–10], and surface reaction [2–4,11] have been primarily concerned with summarizing experimental results and with presenting techniques for interpreting experimental data. While theoretical methods for predicting rate and diffusion coefficients are discussed in some of these publications, none has included a comprehensive overview of all four elementary processes. In other reviews [12–14], the theoretical approaches used to model gas–surface dynamics are described, but the success or failure of a given approach to produce results consistent with experimental observation is not treated. The purpose of this review is to put into perspective the different theoretical approaches available for describing rate and diffusion coefficients and to evaluate the success of a given approach in providing quantitative agreement with experiment. The simulation of complex surface processes in which the dynamics of individual elementary processes are represented explicitly is also discussed. To limit the scope of this review, attention is restricted to the interactions of gases with metal surfaces.

The remainder of the text is contained in sections 2–7. Section 2 reviews the theoretical concepts used to represent rate and diffusion coefficients and discusses the relative merits and limitations of each approach. The effects of adsorbate coverage on these coefficients is also examined in this section. Sections 3–6 illustrate the success of different theoretical approaches in predicting the magnitude of the coefficients for adsorption, diffusion, desorption, and reaction, respectively. Sections 5 and 6 also discuss the simulation of temperature-programmed desorption and reaction experiments. A set of concluding remarks summarizing the present state of knowledge in gas–surface dynamics is presented in section 7.

2. Theoretical concepts

2.1. Adsorbate–surface potentials

The dynamics of processes occurring at a metal surface are governed by the adsorbate–surface potential. This function is comprised of contributions due to metal–adsorbate interactions and lateral interactions between adsorbates. Ideally, the adsorbate–surface potential should be

obtained by an accurate ab-initio calculation of the energy hypersurface via the solution of the electronic Schrödinger equation. However, even with currently available supercomputers, it is not possible to produce complete energy hypersurfaces that are accurate enough for use in dynamical studies. As a consequence, all theoretical analyses of elementary processes occurring at surfaces are based on semi-empirical expressions, the exact form of the potential depending on the nature of the problem being addressed [15].

2.1.1. Metal–adsorbate interactions

For weakly bonding situations between an adsorbate, A, and n metal atoms, the metal–adsorbate interaction can be described by a sum of Lennard-Jones contributions:

$$V = \sum_{i=1}^{n} 4\epsilon\left[\left(\frac{\sigma}{r_i}\right)^{12} - \left(\frac{\sigma}{r_i}\right)^{6}\right], \tag{2.1}$$

where r_i is the separation distance between the adsorbate and the ith metal atom, and ϵ and σ are Lennard-Jones parameters. Where covalent bonding between the adsorbate and surface occurs, the metal–adsorbate interaction can be described by a sum of two-center Morse potentials

$$V = V_{0A}\sum_{i=1}^{n}\left(x_i^2 - 2x_i\right), \tag{2.2}$$

$$x_i = \exp\left[-(r_i - r_0)/a\right], \tag{2.3}$$

where V_{0A} is the equilibrium (minimum) potential energy, x_i is the Pauling bond order, r_i is the bond distance, r_0 is the equilibrium bond distance, and a is a scaling parameter.

More complex forms of the adsorbate–surface potential have also been used. An example is the London, Eyring, Polanyi and Sato (LEPS) potential surface, which has been used in studies of the adsorption of diatomic molecules on metal surfaces [16]. The LEPS potential for the molecule AB is given by

$$V = \rho_{AS} + \rho_{BS} + \rho_{AB} + \left[\chi_{AB}(\chi_{AB} - \chi_{AS} - \chi_{BS}) + (\chi_{AS} + \chi_{BS})^2\right]^{1/2}, \tag{2.4}$$

where ρ_{ij} and χ_{ij} are the Coulomb and exchange contributions between i and j, and subscript S denotes the surface. The quantities ρ_{ij} and χ_{ij} are expressed in the form of modified Morse potentials.

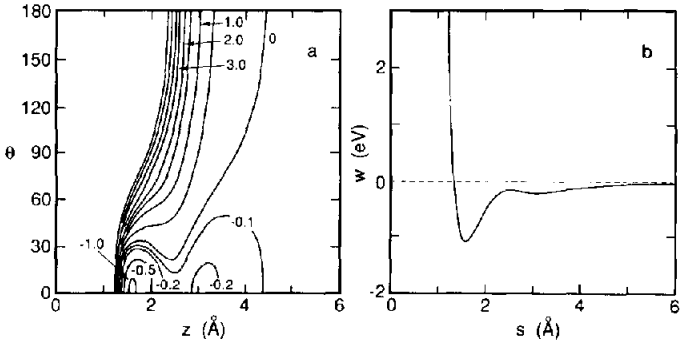

Fig. 1. (a) Potential energy surface for molecular adsorption as a function of orientation angle θ and distance from the surface z. The energy contours are in eV. (b) One-dimensional potential versus reaction coordinate s [44].

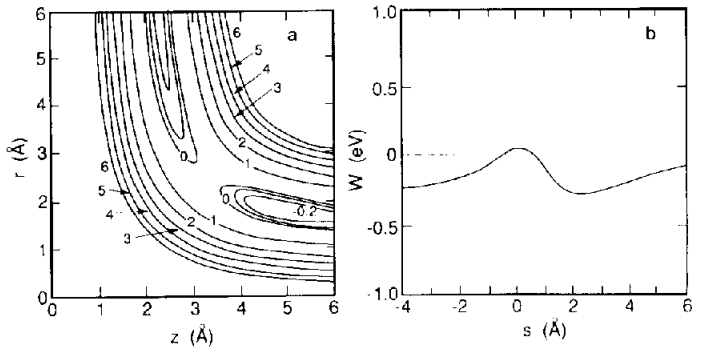

Fig. 2. (a) Potential energy surface for dissociative adsorption as a function of distance from the surface z and internal bond distance r. The energy contours are in eV. (b) One-dimensional potential versus reaction coordinate s [44].

While the adsorbate–surface potential is a multi-dimensional function in general, critical features of the potential energy surface are best characterized by examining the variation of the potential along a trajectory corresponding to the so-called reaction coordinate, s. Illustrations of two-dimensional potential surfaces and their one-dimensional representations corresponding to trajectories along the reaction coordinate are presented in figs. 1 and 2 for the cases of non-dissociative and dissociative adsorption, respectively.

For non-dissociative adsorption of a molecule AB, the one-dimensional potential in fig. 1b is zero for large distances from the surface. As the adsorbate–metal distance is reduced, the potential goes through a weak minimum and then a weak maximum before it reaches the final minimum corresponding to the adsorbed state. The first minimum is associated with the presence of a weakly bound precursor state, whereas the maximum corresponds to the activation energy barrier for adsorption. For dissociative adsorption, a qualitatively similar picture is observed. In fig. 1a $s = z$, whereas in fig. 2b s is the distance along the minimum energy trajectory connecting reactant and product states.

2.1.2. Lateral interactions

While interactions between adsorbates can be ignored at low coverages, experimental evidence indicates that with increasing coverage, such interactions can become significant. Several processes can contribute to lateral interactions. Repulsive interactions can arise from mutually aligned dipoles and from changes in adsorbate–site orbital overlap due to the interaction of multiple adsorbates with a single adsorption site. The direct interactions of orbitals on adjacent species may lead to either attractive or repulsive contributions to the total energy. The classification of an interaction between two species as purely attractive or purely repulsive, however, is not always precise. Quantum models have demonstrated that the nature of an interaction between adsorbates depends upon the separation distance and the crystallographic direction on the surface [17,18].

The description of lateral interactions depends upon the nature of the system considered. For the adsorption of weakly bound (physisorbed) species, lateral interactions between adsorbates can be handled by the addition of appropriate Lennard-Jones terms to eq. (2.1). For strongly bound (chemisorbed) species, the effects of lateral interactions can be expressed as a perturbation in the heat of adsorption of the adsorbate in the absence of lateral interactions.

The simplest representation of lateral interactions for chemisorbed species is based on the

assumption that all contributions are pairwise additive. If attention is restricted to interactions with nearest neighbors, the heat of adsorption of species A is given by

$$Q_A = Q^0 - n_1 w_{AA}, \tag{2.5}$$

where Q^0 is the heat of adsorption of A in the absence of lateral interactions, w_{AA} is the energy of each A–A interaction between nearest neighbors (w_{AA} is positive for repulsive interactions and negative for attractive interactions), and n_1 is the number of nearest-neighbor sites occupied by an adsorbate. If next-nearest-neighbor interactions are also included, then Q_A is written as

$$Q_A = Q^0 - n_1 w_{AA} - n_2 w_{AA'}, \tag{2.6}$$

where n_2 is the number of occupied next-nearest-neighbor sites and $w_{AA'}$ is the interaction energy between an adsorbate A and its next-nearest neighbor A′. Eqs. (2.5) and (2.6) are both derived empirically and, hence, are not based on any physical model for lateral interactions.

Recently, an alternative to eq. (2.5) has been developed based on the bond-order-conservation-Morse-potential (BOC-MP) approach pioneered by Shustorovich [19–21]. This method describes each two-center interaction between an adsorbate atom A and a surface metal atom M by a Morse potential, and the total heat of adsorption is given by the sum of all two-center interactions. A further assumption of the BOC method is that along a reaction path describing the interactions of a molecular or atomic species with a metal surface, the total bond order, x, is conserved and normalized to unity. In this context, the bond order for a given atom pair is defined in terms of the logarithm of the displacement of the equilibrium bond distance for that atom pair [19–21].

Within the BOC-MP framework, the heat of chemisorption for an isolated atom A on a surface is given by

$$Q_{A,n} = Q_{0A}(2 - 1/n), \tag{2.7}$$

where Q_{0A} is the heat of chemisorption of A in the on-top position, and n is the number of metal atoms to which A is coordinated. For an isolated molecular adsorbate AB coordinated via atom A to n metal atoms, the heat of chemisorption can be approximated by

$$Q_{AB,n} = \frac{Q_{0A}^2}{D_{AB} + Q_{0A}/n}, \tag{2.8}$$

where D_{AB} is the gas-phase A–B bond energy.

Eqs. (2.7) and (2.8) are valid for isolated adsorbate atoms or molecules on a surface. For higher coverages, however, situations may arise in which more than one adsorbate is bonded to a metal atom and, furthermore, the adsorbates may interact directly with each other. To account for these metal–adsorbate (M–A) and adsorbate–adsorbate (A–A) interactions, the total binding energy of species A is partitioned as follows:

$$Q_{A,n}^* = Q_{A,n}^{(1)} + Q_{A,n}^{(2)}, \tag{2.9}$$

where $Q_{A,n}^{(1)}$ is the heat of adsorption due to M–A interactions and $Q_{A,n}^{(2)}$ is the heat of adsorption due A–A interactions. Both $Q_{A,n}^{(1)}$ and $Q_{A,n}^{(2)}$ can be calculated explicitly as a function of the total occupancy of nearest-neighbor sites, under the constraint that the total bond order of A for both M–A and A–A interactions is conserved to unity.

The value of $Q_{A,n}^{(2)}$ can be expressed as

$$Q_{A,n}^{(2)} = \sum_{i=1}^{n} \sum_{l=1}^{L} 0.5 D_{AA}\left(2\delta_{il} - \delta_{il}^2\right), \tag{2.10}$$

where D_{AA} is the A–A bond dissociation energy, and δ_{il} is the bond order for the A–A interaction between the A atom coordinated with metal i and the lth nearest-neighbor A atom also coordinated with metal atom i. The summation over l in eq. (2.10) is to account for all nearest-neighbor A atoms. The occurrence of A–A interactions weakens the bond order associated with the M–A interactions and, as a consequence, the bond order for each component of an M_n–A bond is given by

$$x_{i,n} = \frac{1}{n} - \sum_{l=1}^{L} \delta_{il}. \tag{2.11}$$

The value of $Q^{(1)}_{A,n}$ when more than one adsorbate is bonded to an individual metal atom is given by

$$Q^{(1)}_{A,n} = \sum_{i=1}^{n} \left[\frac{Q_{0A}}{m_i} \left(2 - \frac{1}{m_i}\right)\left(2x_{i,n} - x^2_{i,n}\right)\right], \tag{2.12}$$

where m_i is the number of adsorbates bonded to the ith metal atom, and $x_{i,n}$ is given by eq. (2.11).

2.1.3. Activation energy barriers

The characteristic of the potential energy hypersurface having the greatest effect on the dynamics of an elementary process is the height of the activation barrier, E, for movement from the region of the potential surface associated with the reactant state to that associated with the product state. Since the full, multi-dimensional potential surface cannot be described in most instances, semiempirical expressions must be used to relate E to the properties of the reactants and describe the effects of lateral interactions between adsorbates.

The simplest representation of E when lateral interactions occur is based on the assumption that all contributions are pairwise additive. When only nearest-neighbor interactions are considered, E is given by

$$E = E^0 - n_1 w_{AA}, \tag{2.13}$$

where E^0 is the activation energy in the absence of lateral interactions, w_{AA} is the contribution of nearest-neighbor A–A interactions to E, and n_1 is the number of nearest neighbors. The form of eq. (2.13) is empirical and is not based on any physical model for the interactions of nearest-neighbor adsorbates.

The BOC-MP [21] approach provides an alternative method for estimating the magnitude of E. The activation energy for dissociative adsorption from the gas phase ($AB_g \rightarrow A_s + B_s$), E_a, can be written as

$$E_a = \tfrac{1}{2}\left[D_{AB} - (Q_A + Q_B) + \frac{Q_A Q_B}{Q_A + Q_B} - Q_{AB}\right]. \tag{2.14}$$

For non-associative desorption ($A_s \rightarrow A_g$ or $AB_s \rightarrow AB_g$), E_d is given by

$$E_d = Q_A \quad \text{or} \quad E_d = Q_{AB}, \tag{2.15}$$

whereas for associative desorption ($A_s + B_s \rightarrow AB_g$), E_d is given by

$$E_d = Q_A + Q_B - D_{AB} + E_a, \quad \text{if } E_a > 0, \tag{2.16}$$

or

$$E_d = Q_A + Q_B - D_{AB}, \qquad \text{if } E_a < 0. \tag{2.17}$$

Expressions similar to eqs. (2.16) and (2.17) can be used to calculate the activation energy for reactions, E_r. In the BOC-MP framework, the activation energy for atomic diffusion across a bridge site, E_{diff}, is given by

$$E_{diff} = [(n-2)/(4n-2)]\,Q_A, \tag{2.18}$$

where n is the coordination number for the adsorbed species in a hollow site (viz., $n = 3,4,5$). The influence of lateral interactions on the activation energy can be determined using eq. (2.9) to calculate Q_i for each species i appearing in eqs. (2.14)–(2.18).

2.2. Kinetics of adsorption, desorption, and surface reaction

The relationship between the rate of a surface process and the adsorbate coverage – the kinetics of the process – depends on the nature of the process and the extent to which lateral interactions are important. In the absence of such interactions, and assuming that all adsorbed species are randomly distributed, simple expressions can be written to relate the rate of a process to the surface coverage, θ. The dependence of the rate of elementary processes on θ are much more complex when lateral interactions are included.

2.2.1. Non-interacting adsorbates

For non-interacting adsorbates, the rate of adsorption of gas-phase species, r_a, can be written as:

$$r_a = S^{(\alpha)}(\theta)\,F, \tag{2.19}$$

where F is the flux of the adsorbate and $S^{(\alpha)}(\theta)$ is the sticking coefficient. The superscript α on $S^{(\alpha)}(\theta)$ is 1 for non-dissociative and 2 for dissociative adsorption. The form of $S^{(\alpha)}(\theta)$ depends on whether adsorption occurs directly from the gas phase or via a precursor state. For direct adsorption,

$$S^{(\alpha)}(\theta) = S^{(\alpha)}(0)(1-\theta)^{\alpha}, \tag{2.20}$$

where $S^{(\alpha)}(0)$ is the sticking coefficient at zero coverage. If $S^{(\alpha)}(0)$ is assumed to obey an Arrhenius expression, then

$$S^{(\alpha)}(0) = S_0^{(\alpha)} \exp(-E_a/k_b T), \tag{2.21}$$

where $S_0^{(\alpha)}$ and E_a are the pre-exponential factor and activation energy for adsorption, respectively, and k_b is the Boltzmann constant.

When adsorption is assumed to proceed via a precursor state, the mechanism of adsorption can be represented by [22]:

$$A \underset{k_d^*}{\overset{\zeta F_A}{\rightleftarrows}} A^* \xrightarrow{k_a^*} A_s,$$

$$A_2 \underset{k_d^*}{\overset{\zeta F_{A_2}}{\rightleftarrows}} A_2^* \xrightarrow{k_a^*} 2A_s,$$

where the precursor species for non-dissociative adsorption is denoted by A* (A_2^* for dissociative adsorption) and the chemisorbed species by A_s, ζ is the trapping probability from the gas phase into the precursor state, k_a^* is the rate constant for adsorption from the precursor state into the chemisorbed state, and k_d^* is the rate constant for desorption from the precursor state. The precursor state can be located over an empty site (an intrinsic precursor) or over an occupied site (an extrinsic precursor). Two different approaches have been used to represent the

adsorption rate. The first is based on a continuum description and uses the stationary-state approximation to determine the concentration of precursor species [23,24]. The second approach is based on a successive-site statistical model of the type first proposed by Kisliuk [25,26]. Although conceptually different, both approaches have been shown to lead to equivalent forms of the adsorption rate in many cases [24,27].

If the intrinsic and extrinsic precursors are energetically equivalent and each occupies only a single adsite, then the rates of non-dissociative and dissociative adsorption can be written as [22]:

$$r_a = \frac{\zeta F_A k_a^* (1-\theta_A)}{k_d^* + k_a^* (1-\theta_A)}, \tag{2.22}$$

$$r_a = \frac{\zeta F_{A_2} k_a^* (1-\theta_A)^2}{k_d^* + k_a^* [(1-\theta_A)]^2}. \tag{2.23}$$

Eqs. (2.22) and (2.23) can be used together with eq. (2.19) to write expressions for $S^{(\alpha)}(\theta)/S^{(\alpha)}(0)$. Thus,

$$S^{(1)}(\theta)/S^{(1)}(0) = \frac{(1+K)(1-\theta_A)}{1+K(1-\theta_A)}, \tag{2.24}$$

$$S^{(2)}(\theta)/S^{(2)}(0) = \frac{(1+K)(1-\theta_A)^2}{1+K(1-\theta_A)^2}, \tag{2.25}$$

where $K = k_a^*/k_d^*$. A plot of $S^{(1)}(\theta)/S^{(1)}(0)$ versus θ is shown in fig. 3. When $K \gg 1$, $S^{(1)}(\theta)/S^{(1)}(0) = 1$ and when $K \ll 1$, $S^{(1)}(\theta)/S^{(1)}(0) = 1 - \theta$. Since the value of K is temperature-dependent, the shape of $S^{(\alpha)}(\theta)/S^{(\alpha)}(0)$ versus θ will depend on temperature.

The rate of desorption for a randomly distributed adsorbate in the absence of lateral interactions can be written as

$$r_d = k_d^{(\alpha)} \theta^\alpha, \tag{2.26}$$

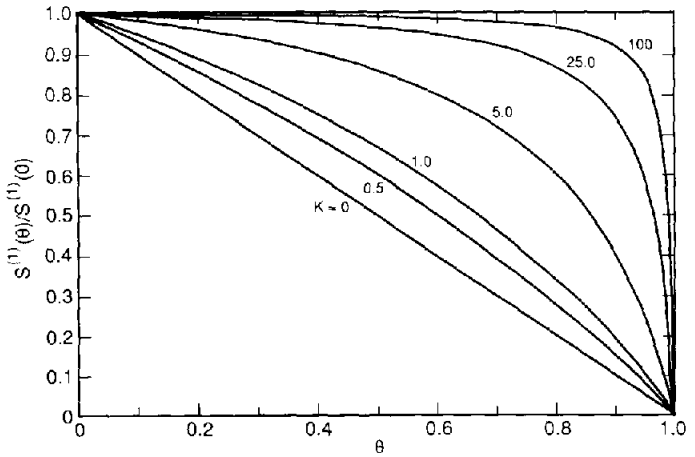

Fig. 3. Variation of $S^{(1)}(\theta)/S^{(1)}(0)$ with θ for adsorption via a precursor mechanism. The precursor parameter $K = k_a^*/k_d^*$.

where $k_d^{(\alpha)}$ is the rate coefficient for desorption. If $k_d^{(\alpha)}$ is assumed to obey an Arrhenius expression, then

$$k_d^{(\alpha)} = \nu_d^{(\alpha)} \exp(-E_d/k_b T), \tag{2.27}$$

where $\nu_d^{(\alpha)}$ and E_d are the pre-exponential factor and activation energy for desorption, respectively.

Implicit in the formulation of eq. (2.27) is the assumption that desorption occurs directly from the adsorbed state. This assumption is unnecessarily restrictive since it is conceivable that the adsorbate passes through a weakly bound precursor state before leaving the catalyst surface. Making the same assumptions used in deriving eqs. (2.22) and (2.23), the rates of non-associative and associative desorption can be written as [22]:

$$r_d = \frac{k_d^{(1)} k_d^* \theta_A}{k_a^*(1-\theta_A) + k_d^*}, \tag{2.28}$$

$$r_d = \frac{k_d^{(2)} k_d^* \theta_A^2}{k_a^*(1-\theta_A)^2 + k_d^*}. \tag{2.29}$$

In the limit $k_a^*(1-\theta)^\alpha \ll k_d^*$, eqs. (2.28) and (2.29) reduce to eq. (2.26).

Surface reactions can be classified into two generic types. The first includes reactions between two adsorbed species or an adsorbed species and a vacant site (Langmuir–Hinshelwood processes). For randomly distributed adsorbates on a surface in the absence of adsorbate–adsorbate interactions, the rate of reaction is given by:

$$r_r = k_r \theta_A \theta_B \tag{2.30}$$

or

$$r_r = k_r \theta_A \theta_V, \tag{2.31}$$

where k_r is the rate coefficient, θ_i is the surface coverage of species i and θ_V is the fraction of vacant sites. If k_r follows an Arrhenius expression, then

$$k_r = \nu_r \exp(-E_r/k_b T), \tag{2.32}$$

where ν_r and E_r are the pre-exponential factor and the activation energy for reaction, respectively.

The second class of reactions includes the direct interaction of a gas-phase species with an adsorbed species to form a product which may either remain adsorbed or desorb into the gas phase (Eley–Rideal processes). For such processes, the rate of reaction can be written as

$$r_r = k_r \theta_A P_B, \tag{2.33}$$

where P_B is the partial pressure of reactant B. The form of eq. (2.33) is similar to that for adsorption and so k_r can be represented as a reactive sticking coefficient, S_0, by the expression

$$k_r = \frac{S_0 a_s}{(2\pi m_B k_b T)^{1/2}} \exp(-E_r/k_b T), \tag{2.34}$$

where a_s is the area per reaction site, and m_B is the molecular weight of species B.

2.2.2. Interacting adsorbates

When lateral interactions become significant, the relationships between the rate of an elementary process and the adsorbate coverage become quite complex and cannot, in general,

be written in closed form. An exception to this occurs in the case where a lattice-gas model is used to describe the effects of lateral interactions. In such a model, each adsorbate is assumed to be localized on a two-dimensional array of surface sites, and each site is assumed to be either vacant or occupied by a single adsorbate. A given adsorbate can interact with adsorbates on nearest-neighbor sites, next-nearest-neighbor sites, etc., but in most variants of the lattice-gas model, only nearest-neighbor interactions are taken into account. Using these assumptions, relationships can be derived between the adsorbate coverage and the rate of adsorption, desorption, and surface reaction [28–30].

The rate of non-dissociative adsorption is defined as

$$r_a = FS_0^{(1)} \sum_{n_1} P_{V,n_1} \exp\left[\frac{-\left(E_a^0 - E_s\right)}{k_b T}\right](1-\theta), \tag{2.35}$$

where $S_0^{(1)}$ is the initial sticking coefficient, P_{V,n_1} is the probability of finding a vacant site with n_1 occupied nearest-neighbor sites, E_a^0 is the activation energy for adsorption in the absence of nearest-neighbor interactions, and E_s is the interaction energy of A with its neighbors. E_s can be related to the energy for a given pairwise interaction, w_{AA}, by $E_s = n_1 w_{AA}$. For dissociative adsorption, the rate of adsorption can be expressed as

$$r_a = FS_0^{(2)} \sum_{n_1,m_1} P_{VV;n_1,m_1} \exp\left[\frac{-\left(E_a^0 - E_s\right)}{k_b T}\right], \tag{2.36}$$

where $P_{VV;n_1,m_1}$ is the probability that two nearest-neighbor sites are vacant such that one is surrounded by n_1 nearest neighbors and the other is surrounded by m_1 nearest neighbors.

To complete the description of the lattice-gas model, it is necessary to develop expressions for P_{V,n_1} and $P_{VV;n_1,m_1}$ in terms of θ_A and w_{AA}. Since an exact solution to this problem can only be achieved for a coverage of 0.5, an approximation must be made to obtain a solution in closed form. One of the more widely used postulates is the quasi-chemical approximation (QCA) which assumes that the adsorbates maintain an equilibrium distribution on the surface. The QCA treats the probabilities P_{V,n_1} and $P_{VV;n_1,m_1}$ in terms of the probabilities P_{AA}, P_{AV}, and P_{VV}, where P_{AA} is the probability that two nearest-neighbor sites are occupied by species A, P_{VV} is the probability that two nearest-neighbor sites are vacant, and P_{AV} is the probability that of two nearest-neighbor sites, one is occupied and the other is vacant. These probabilities are described by the equations:

$$P_{AA} + P_{AV} + P_{VV} = 1, \tag{2.37}$$

$$2P_{AA} + P_{AV} = 2\theta, \tag{2.38}$$

$$P_{AA}P_{VV}/P_{AV}^2 = \tfrac{1}{4}\exp(-w_{AA}/k_b T). \tag{2.39}$$

The solution to eqs. (2.37)–(2.39) is given by

$$P_{AA} = \theta - \left\{1 - \left[1 - 2\eta\theta(1-\theta)\right]^{1/2}\right\}/\eta, \tag{2.40}$$

$$P_{AV} = 2\left\{1 - \left[1 - 2\eta\theta(1-\theta)\right]^{1/2}\right\}/\eta, \tag{2.41}$$

$$P_{VV} = 1 - \theta - \left\{1 - \left[1 - 2\eta\theta(1-\theta)\right]^{1/2}\right\}/\eta, \tag{2.42}$$

where $\eta = 2[1 - \exp(-w_{AA}/k_b T)]$.

In the QCA, different pairs of sites are considered to be independent and hence

$$P_{V,n_1} = \frac{z!}{n_1!\,(z-n_1)!} \frac{(0.5P_{AV})^{n_1}(P_{VV})^{z-n_1}}{(0.5P_{AV} + P_{VV})^z}, \tag{2.43}$$

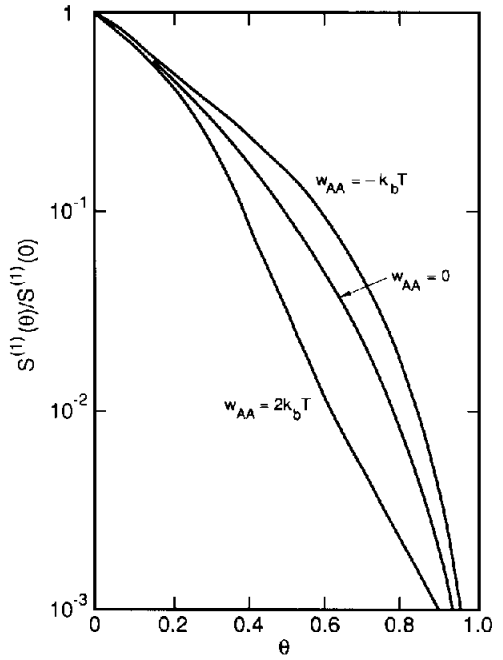

Fig. 4. Variation in $S^{(1)}(\theta)/S^{(1)}(0)$ versus θ when nearest-neighbor interactions occur [31].

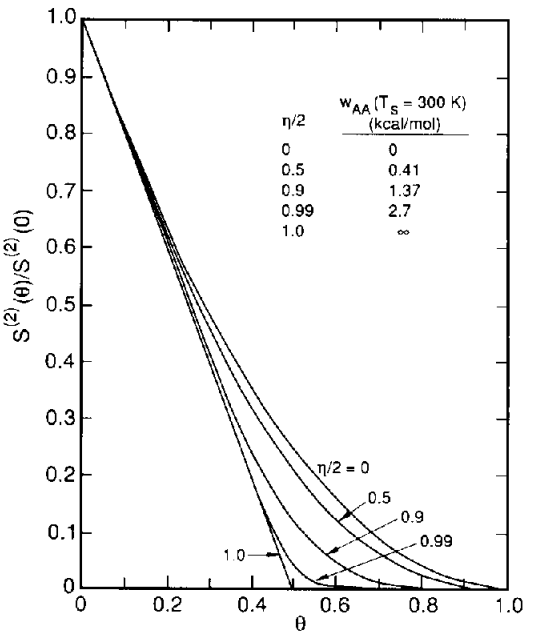

Fig. 5. Variation in $S^{(2)}(\theta)/S^{(2)}(0)$ versus θ for repulsive nearest-neighbor interactions [32].

where z is the number of nearest-neighbor sites. Using eqs. (2.40)–(2.43), the following functions can be defined to represent the sums appearing in eqs. (2.35) and (2.36), respectively [29]:

$$f_a'(\theta, w_{AA}) = \sum_{n_1} P_{V,n_1} \exp(n_1 w_{AA}/k_bT) = \left[\frac{0.5P_{AV}\exp(w_{AA}/k_bT) + P_{VV}}{1-\theta}\right]^z, \tag{2.44}$$

$$f_a''(\theta, w_{AA}) = \sum_{n_1,m_1} P_{VV;n_1,m_1} \exp[(n_1+m_1)w_{AA}/k_bT]$$

$$= P_{VV}\left[\frac{0.5P_{AV}\exp(w_{AA}/k_bT) + P_{VV}}{1-\theta}\right]^{2z-2}. \tag{2.45}$$

When $w_{AA} = 0$, $f_a'(\theta_A, w_{AA}) = 1$ and $f_a''(\theta_A, w_{AA}) = (1-\theta)^2$, and eqs. (2.35) and (2.36) become identical to eqs. (2.19)–(2.21). Thus, f_a' and f_a'' represent corrections to eqs. (2.19)–(2.21) due to lateral interactions.

The influence of lateral interactions on the sticking coefficient for non-dissociative adsorption is illustrated in fig. 4 for different values of w_{AA} [31]. For a fixed value of θ, $S^{(1)}(\theta)/S^{(1)}(0)$ is largest for attractive interactions. When $w_{AA} = 0$, $S^{(1)}(\theta)/S^{(1)}(0)$ reduces to $1-\theta$.

Fig. 5 illustrates the effects of lateral interactions on the sticking coefficient for dissociative adsorption [32]. At low coverages, $S^{(2)}(\theta)/S^{(2)}(0)$ is practically independent of $\eta/2$ ($\eta/2 = [1 - \exp(-w_{AA}/k_bT)]$), whereas at high coverage, $S^{(2)}(\theta)/S^{(2)}(0)$ decreases more rapidly with increasing $\eta/2$. When $w_{AA} = 0$, $S^{(2)}(\theta)/S^{(2)}(0) = (1-\theta)^2$, which is equivalent to the expression for non-activated adsorption for randomly distributed adsorbates. For large repulsive

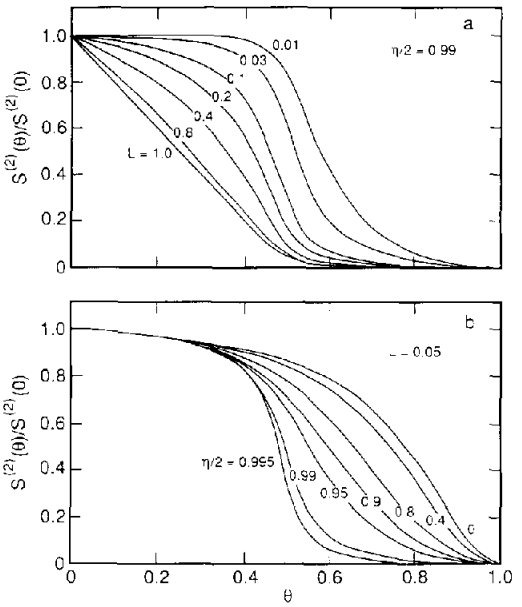

Fig. 6. (a) Variation in $S^{(2)}(\theta)/S^{(2)}(0)$ versus θ when precursor states exist for a fixed value of η. (b) Variation in $S^{(2)}(\theta)/S^{(2)}(0)$ versus θ when precursor states exist for a fixed value of L [32].

interactions ($w_{AA} \to \infty$), $S^{(2)}(\theta)/S^{(2)}(0) = 1 - 2\theta$ for $\theta \leq 0.5$, which represents pseudo-first-order dissociative adsorption kinetics.

The influence of lateral interactions on adsorption kinetics has also been investigated for the case of dissociative adsorption via a precursor mechanism. King and Wells [32] have shown that when intrinsic and extrinsic precursor states exist, $S^{(2)}(\theta)/S^{(2)}(0)$ can be written as

$$\frac{S^{(2)}(\theta)}{S^{(2)}(0)} = \frac{1}{1 + L(1/P_{VV} - 1)}, \tag{2.46}$$

where $L \propto r_d^*/(r_a^{**} + r_d^{**})$. The desorption rates from extrinsic and intrinsic precursor states are denoted by r_d^* and r_d^{**}, respectively, and the adsorption rate from the intrinsic precursor state is denoted by r_a^{**}. If $r_a^{**} \gg r_d^*$, r_d^{**}, then $L \to 0$, whereas when $r_a^{**} \ll r_d^*$, r_d^{**}, then $L \to 1$. L is thus a measure of the relative importance of the adsorption and desorption processes. A plot of $S^{(2)}(\theta)/S^{(2)}(0)$ parametric in L for a fixed value of $\eta/2$ is shown in fig. 6a. When $L \to 0$, $S^{(2)}(\theta)/S^{(2)}(0)$ is larger than when $L \to 1$. Fig. 6b show a plot of $S^{(2)}(\theta)/S^{(2)}(0)$ parametric in $\eta/2$ for a fixed value of L. At high coverage, $S^{(2)}(\theta)/S^{(2)}(0)$ is strongly dependent on the magnitude of w_{AA} and decreases with increasingly repulsive values of w_{AA}. It is significant to note that the shape and magnitude of the plots of $S^{(2)}(\theta)/S^{(2)}(0)$ differ considerably depending on whether precursor states do (see figs. 6a and 6b) or do not exist (see fig. 5).

The rate of non-associative desorption is defined as

$$r_d = \nu_d^{(1)} \sum_{n_1} P_{A,n_1} \exp\left[-\left(E_d^0 - E_s\right)/k_b T\right] \theta, \tag{2.47}$$

where P_{A,n_1} is the probability of finding an adsorbate A with n nearest-neighbors, E_d^0 is the activation energy for desorption in the absence of nearest-neighbor interactions, and E_s is the

interaction energy of A with its neighbors. E_s can be related to the energy for a given pairwise interaction, w_{AA}, by $E_s = n_1 w_{AA}$. For associative desorption, the rate of desorption can be expressed as

$$r_d = \nu_d^{(2)} \sum_{n_1,m_1} P_{AA;n_1,m_1} \exp\left[-\left(E_d^0 - E_s\right)/k_b T\right], \tag{2.48}$$

where $P_{AA;n_1,m_1}$ is the probability that two nearest-neighbor sites are occupied by A atoms such that one is surrounded by n_1 nearest neighbors and the other is surrounded by m_1 nearest neighbors.

Expressions for P_{A,n_1} and $P_{AA;n_1,m_1}$ can be written using the QCA. Thus, for $P_{A,n}$ one can write

$$P_{A,n_1} = \frac{z!}{n_1!\,(z-n_1)!} \frac{P_{AA}^{n_1}(0.5P_{AV})^{z-n_1}}{(P_{AA}+0.5P_{AV})^z}. \tag{2.49}$$

Using eqs. (2.40)–(2.42) and (2.49), one can define the following functions [28,29]:

$$f_d'(\theta, w_{AA}) = \sum_{n_1} P_{A,n_1} \exp(n_1 w_{AA}/k_b T) = \left[\frac{P_{AA}\exp(w_{AA}/k_b T) + 0.5P_{AV}}{\theta}\right]^z, \tag{2.50}$$

$$f_d''(\theta, w_{AA}) = \frac{\sum_{n_1,m_1} P_{AA;n_1,m_1} \exp\left[(n_1+m_1)w_{AA}/k_b T\right]}{\theta^2}$$

$$= P_{AA}\left[\frac{P_{AA}\exp(w_{AA}/k_b T) + 0.5P_{AV}}{\theta}\right]^{2z-2}. \tag{2.51}$$

Substitution of eqs. (2.50) and (2.51) into eqs. (2.47) and (2.48), respectively, gives:

$$r_d = \nu_d^{(1)} \exp\left(-E_d^0/k_b T\right)\theta f_d'(\theta, w_{AA}), \tag{2.52}$$

$$r_d = \nu_d^{(2)} \exp\left(-E_d^0/k_b T\right) f_d''(\theta, w_{AA}). \tag{2.53}$$

When $w_{AA} = 0$, $f_d'(\theta_A, w_{AA}) = 1.0$ and $f_d''(\theta_A, w_{AA}) = \theta_A^2$, and eqs. (2.52) and (2.53) become identical to eqs. (2.26) and (2.27). Thus, f_d' and f_d'' represent corrections to the Polanyi–Wigner

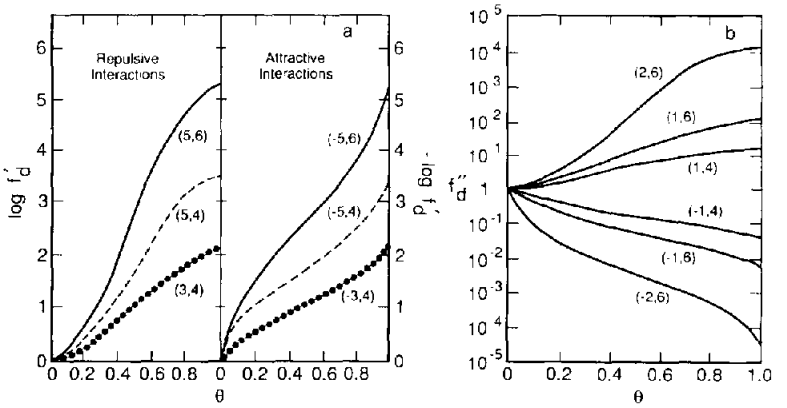

Fig. 7. (a) Variation in f_d' with θ at $T = 300$ K [30]. The nomenclature (5,6) corresponds to $w_{AA} = 5$ kJ/mol and $z = 6$, respectively. (b) Variation in f_d'' with θ [28]. The nomenclature (2,6) corresponds to $w_{AA} = 2k_b T$ and $z = 6$, respectively.

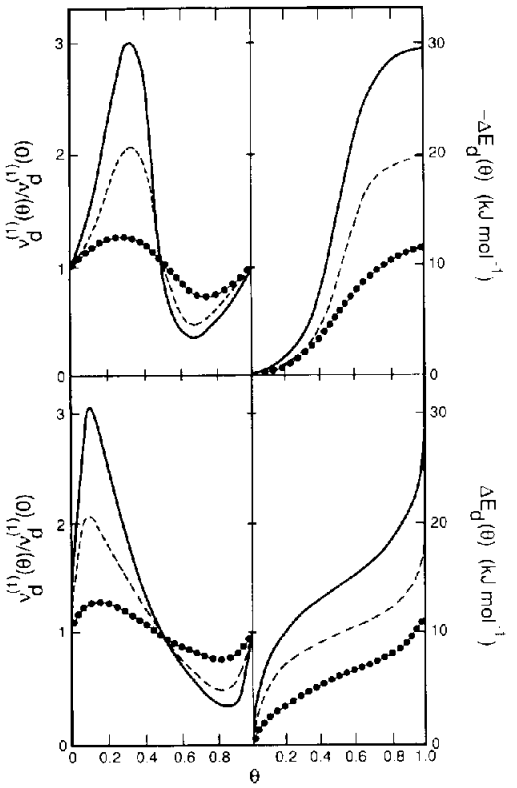

Fig. 8. Variation of $\nu_d^{(1)}(\theta)/\nu_d^{(1)}(0)$ and $\Delta E_d(\theta)$ with θ for repulsive (top panels) and attractive (bottom panels) interactions [30]. Solid line: $|w_{AA}| = 5$ kJ/mol, $z = 6$; dashed line: $|w_{AA}| = 5$ kJ/mol, $z = 4$; dotted line: $|w_{AA}| = 3$ kJ/mol, $z = 6$.

expressions for desorption (eqs. (2.26) and (2.27)) due to lateral interactions. The functions f_d' and f_d'' are plotted in fig. 7 for attractive and repulsive values of w_{AA}/k_bT. It is apparent that even for small values of w_{AA}/k_bT, lateral interactions can have a profound effect on f_d' and f_d''.

Another way of visualizing the effects of lateral interactions is to look at the coverage dependences of the apparent activation energy and the apparent pre-exponential factor. For non-associative desorption, these quantities are defined by [30]:

$$\Delta E_d(\theta) = k_bT^2\, d(\ln f_d')/dT, \tag{2.54}$$

$$\nu_d^{(1)}(\theta)/\nu_d^{(1)}(0) = f_d' \exp\left[\Delta E_d(\theta)/k_bT\right]. \tag{2.55}$$

Fig. 8 shows that the variation in $\Delta E_d(\theta)$ and $\nu_d^{(1)}(\theta)/\nu_d^{(1)}(0)$ with θ is a strong function not only of w_{AA}/k_bT, but also of z. The apparent activation energy is seen to vary monotonically with coverage whereas the apparent pre-exponential factor exhibits a more complex coverage dependence.

The lattice-gas model developed for the description of associative desorption can be extended to describe the kinetics of Langmuir–Hinshelwood processes. The rate of the bimolecular reaction $A_s + B_s \rightarrow C_s$ or C_g can be written as

$$r_r = \nu_r \sum_i P_{AB;i} \exp\left[-\left(E_r^0 - E_s\right)/k_bT\right], \tag{2.56}$$

where ν_r is the pre-exponential factor, $P_{AB;i}$ is the probability that two nearest sites are occupied by an AB pair and that this pair has the environment i, E_r^0 is the activation energy for the reaction of A and B in the absence of nearest-neighbor interactions, and E_s is the contribution to the activation energy due to nearest-neighbor interactions. The lateral interaction energy of the AB pair is determined by k, l, k', and l', where k and l (k' and l') are the numbers of A and B neighbors of A_s (B_s), respectively. Using these indices, E_s is written as

$$E_s = kw_{AA} - (l + k')w_{AB} - l'w_{BB}. \tag{2.57}$$

In the limit of the QCA, the probability $P_{AB;i}$ can be expressed in terms of P_{AA}, P_{AB}, P_{BB}, P_{AV}, P_{BV}, P_{VV}, and P_{AB}. These probabilities are described by the equations

$$P_{AA} + P_{AB} + P_{AV} + P_{BB} + P_{BV} + P_{VV} = 1, \tag{2.58}$$

$$2P_{AA} + P_{AB} + P_{AV} = 2\theta_A, \tag{2.59}$$

$$2P_{BB} + P_{AB} + P_{BV} = 2\theta_B, \tag{2.60}$$

$$P_{AA}P_{VV}/P_{AV}^2 = \tfrac{1}{4}\exp(-w_{AA}/k_bT), \tag{2.61}$$

$$P_{BB}P_{VV}/P_{BV}^2 = \tfrac{1}{4}\exp(-w_{BB}/k_bT), \tag{2.62}$$

$$P_{AA}P_{BB}/P_{AB}^2 = \tfrac{1}{4}\exp[-(w_{AA} + w_{BB} - 2w_{AB})/k_bT]. \tag{2.63}$$

Zhdanov [28,29] has shown that when the QCA is valid, r_r can be written as

$$r_r = \nu_r \exp(-E_r^0/k_bT)P_{AB}\left[\frac{P_{AA}\exp(w_{AA}/k_bT) + 0.5P_{AB}\exp(w_{AB}/k_bT) + 0.5P_{AV}}{\theta_A}\right]^{z-1}$$
$$\times\left[\frac{P_{BB}\exp(w_{BB}/k_bT) + 0.5P_{AB}\exp(w_{AB}/k_bT) + 0.5P_{BV}}{\theta_B}\right]^{z-1}. \tag{2.64}$$

It is apparent from eq. (2.64) that inclusion of interactions between species leads to a rate expression dependent on the sign and magnitude of these interactions. Moreover, the dependence of r_r on θ_A and θ_B is seen to differ significantly from that based on the assumption of a random adsorbate distribution, as described by eq. (2.30). To establish the extent to which eqs. (2.30) and (2.64) differ, it is useful to define the function [29]

$$f_r = \frac{\sum_i P_{AB;i}\exp[\Delta E_r(\theta)/k_bT]}{\theta_A\theta_B}. \tag{2.65}$$

Calculations of f_r for a square lattice are given in fig. 9. Both the magnitude and sign of the A–A, A–B, and B–B interactions influence f_r.

2.3. Diffusion

The diffusion of an adsorbate on a surface can be characterized by two types of motion. When the activation energy for diffusion, E_{diff}, is less than k_bT, the adsorbate translates freely across the surface. This type of motion, which is termed mobile diffusion, is characteristic of physisorbed species. When E_{diff} is significantly greater than k_bT, the adsorbate moves from site to site by hopping over the activation barrier. Diffusion via a hopping mechanism is characteristic of chemisorbed species.

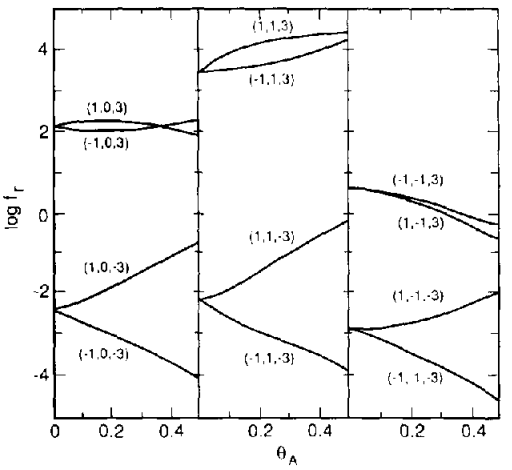

Fig. 9. Variation in f_r with θ [29]. The nomenclature (1,0,3) corresponds to $w_{AA} = k_b T$, $w_{AB} = 0$, and $w_{BB} = 3k_b T$, respectively.

In the absence of a gradient in the concentration of adsorbates, the movement of adsorbates on a metal surface is characterized by the tracer diffusion coefficient, D^T. For two-dimensional motion, D^T can be expressed as

$$D^T = \lim_{t \to \infty} \langle r(t)^2 \rangle / 4t, \tag{2.66}$$

where r is the displaced position at time t and $\langle\ \rangle$ represents an ensemble average over many trajectories. If the adsorbate is freely mobile, D^T can be written in terms of the mean velocity, $\bar{v}$, and the mean-free path, λ, to obtain

$$D^T = \tfrac{1}{2}\bar{v}\lambda. \tag{2.67}$$

For hopping motion, the diffusion coefficient is written as

$$D^T = \tfrac{1}{4}\Gamma\lambda^2, \tag{2.68}$$

where Γ is the hopping frequency and λ now represents the mean-free hopping length. Since hopping is an activated process which is known to depend on temperature, it is customary to express Γ as

$$\Gamma = \nu^T_{diff} \exp\left(-E^T_{diff}/k_b T\right), \tag{2.69}$$

where ν^T_{diff} is the pre-exponential factor for hopping. Substitution of eq. (2.69) into eq. (2.68) leads to:

$$D^T = \tfrac{1}{4}\lambda^2 \nu^T_{diff} \exp\left(-E^T_{diff}/k_b T\right) = D^T_0 \exp\left(-E^T_{diff}/k_b T\right), \tag{2.70}$$

where D^T_0 is referred to as the pre-exponential factor for diffusion.

When the surface concentration of adsorbate is nonuniform, mass transport can occur due to a gradient in the chemical potential, μ, of the adsorbate. The relationship between the flux of adsorbate, J, and the gradient in the chemical potential is given by

$$J = -D^C(C/k_b T)\ \nabla\mu, \tag{2.71}$$

where C is the adsorbate concentration and D^C is the diffusion coefficient defined by eq. (2.71) [33]. Eq. (2.71) can be related to Fick's first law of diffusion in the following manner:

$$J = -D^C\left[\frac{\partial(\mu/k_bT)}{\partial(\ln\theta)}\right]_T \nabla C = -D(\theta)\,\nabla C. \tag{2.72}$$

It is apparent from eq. (2.72) that the Fickian diffusion coefficient $D(\theta)$ is, in general, a function of θ.

A representation of $D(\theta)$ in closed form can be developed assuming that adsorbate diffusion occurs by discrete hops on a well-defined lattice. For such a model,

$$D(\theta) = \tfrac{1}{4}\lambda^2\Gamma(\theta)\left[\frac{\partial(\mu/k_bT)}{\partial(\ln\theta)}\right]_T. \tag{2.73}$$

In the limit as θ goes to zero, eq. (2.73) reduces to

$$D(0) = \tfrac{1}{4}\lambda^2\Gamma(0), \tag{2.74}$$

which is identical to eq. (2.68). Thus, for $\theta = 0$, $D(0) = D^T$.

For $\theta > 0$, $\Gamma(\theta)$ must be evaluated to determine $D(\theta)$. Reed and Ehrlich [33] have shown that for a square lattice in the limit of the QCA, $\Gamma(\theta)$ and $\mu(\theta)$ are given by

$$\Gamma(\theta) = \nu_{diff}^T \exp\left(-E_{diff}^T/k_bT\right)(1+\rho_2)^3/(1+\rho_1\rho_2)^4, \tag{2.75}$$

$$\frac{\mu(\theta)}{k_bT} = \frac{\mu^0}{k_bT} + \ln\left(\frac{\theta}{1-\theta}\right) + 2\ln\left[\frac{(\rho_2-1+2\theta)(1-\theta)}{(\rho_2+1-2\theta)\theta}\right], \tag{2.76}$$

where $\mu^0 = \mu(0)$ and

$$\rho_1 = \exp(-w_1/k_bT), \tag{2.77}$$

$$\rho_2 = (\rho_3 - 1 + 2\theta)/[2\rho_1(1-\theta)], \tag{2.78}$$

$$\rho_3 = [1 - 4\theta(1-\theta)(1-\rho_1)]^{1/2}. \tag{2.79}$$

In eq. (2.77), w_1 represents the average magnitude of the lateral interactions between nearest neighbors, As seen in fig. 10, for repulsive interactions, $D(\theta)/D(0)$ increases with increasing θ up to $\theta = 0.8$ and then decreases slightly. Although not shown here, for attractive lateral

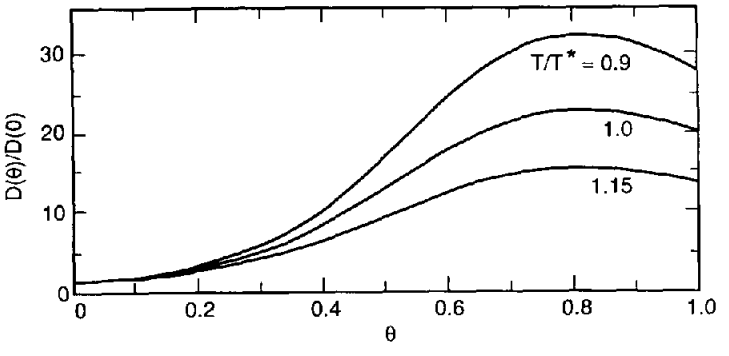

Fig. 10. Variation in $D(\theta)/D(0)$ with θ for repulsive interactions for $w_{AA} = k_bT^*$, where T^* is the standard temperature [33].

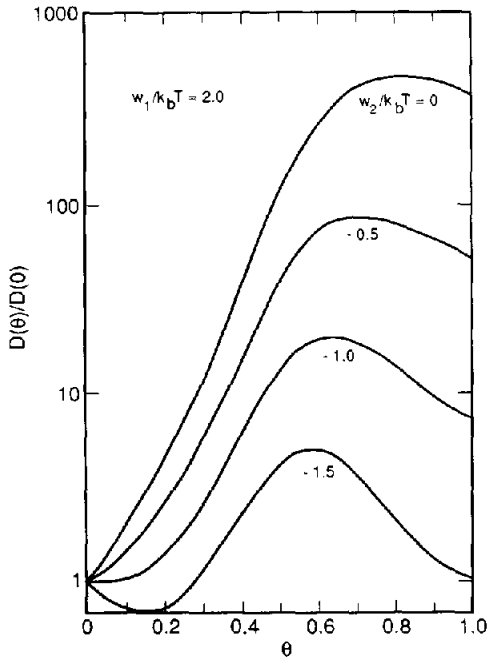

Fig. 11. Variation in $D(\theta)/D(0)$ with θ for nearest- (w_1) and next-nearest- (w_2) neighbor interactions [34].

interactions, $D(\theta)/D(0)$ decreases rapidly from a value of 1.0 at $\theta = 0$ to a value of 0.05 at $\theta = 0.5$ and then remains relatively constant at this value to $\theta = 1.0$.

Using an approach similar to that described above, Zhdanov [34a] has examined how both nearest- (w_1) and next-nearest-neighbor (w_2) interactions influence the dependence of the diffusion coefficient on adsorbate coverage. As seen in fig. 11, $D(\theta)/D(0)$ goes through a maximum with increasing θ. The location of the maximum is sensitive to the magnitude of w_2. Zhdanov [34b] has also examined the effects of coverage when two different species, A and B, are coadsorbed. It was found that $D(\theta)/D(0)$ is sensitive to both the magnitude and sign of the interactions between A and B.

2.4. Theoretical descriptions of surface dynamics

Theoretical descriptions of the dynamics of elementary processes occurring on metal surfaces have been developed on the basis of molecular dynamics, transition-state theory, absolute rate theory, stochastic diffusion theory, and quantum mechanics. Each of these approaches is reviewed to illustrate the manner in which rate or transport coefficients are related to the adsorbate–surface potential.

2.4.1. Molecular dynamics

The motion of an adsorbate near or on a surface can be obtained from molecular dynamics (MD) simulations. Such simulations provide a spatial and temporal description of the adsorbate trajectory, which can, in turn, be used to determine the sticking coefficient and the surface diffusion coefficient. For reasons discussed below, MD simulations are not well suited, in most cases, for determining the rate coefficient for desorption.

If the atoms in the metal surface are assumed to be stationary, then the adsorbate trajectory, $\boldsymbol{Y}(t)$, is given by

$$m\ddot{\boldsymbol{Y}} = -\partial V(\boldsymbol{Y})/\partial \boldsymbol{Y}, \tag{2.80}$$

where m is the adsorbate mass and $V(\boldsymbol{Y})$ is the adsorbate–surface potential. A more realistic description of adsorbate–surface interactions is obtained when the metal atoms are allowed to vibrate. Treating the motion of all the metal atoms, however, is computationally infeasible. To circumvent this, the problem is formulated in the following manner [35]. The adsorbate is assumed to interact strongly with 1–10 atoms of the metal. This cluster constitutes the primary zone, and the interactions between the adsorbate and the metal atoms in the primary zone are described by $V_p(\boldsymbol{x}_p, \boldsymbol{Y})$, where $\boldsymbol{Y}$ describes the position of the adsorbate and $\boldsymbol{x}_p$ describes the positions of the metal atoms in the primary zone. Adsorbate interactions with metal atoms outside the primary zone (i.e., in the secondary zone or heat bath) are described by the potential $V_s(\boldsymbol{Y})$. Thus the total interaction potential is $V(\boldsymbol{x}_p, \boldsymbol{Y}) = V_s(\boldsymbol{Y}) + V_p(\boldsymbol{x}_p, \boldsymbol{Y})$. The motion of the adsorbate is given by

$$m\ddot{\boldsymbol{Y}} = -\partial V(\boldsymbol{x}_p, \boldsymbol{Y})/\partial \boldsymbol{Y}, \tag{2.81}$$

whereas the motion of the metal atoms in the primary zone is given by a generalized Langevin equation

$$m'\ddot{\boldsymbol{x}}_p = -\omega_{pp}^2 m'\boldsymbol{x}_p - \partial V(\boldsymbol{x}_p, \boldsymbol{Y})/\partial \boldsymbol{x}_p + m'\int_0^t \Theta(t-\tau)\, \boldsymbol{x}_p \, d\tau + \boldsymbol{R}(t), \tag{2.82}$$

where m' is the mass of metal atom. The parameter ω_{pp} in eq. (2.82) is the characteristic frequency for vibration of metal atoms in the primary zone, and the functions $\Theta(t)$ and $\boldsymbol{R}$(t) correspond to a memory kernel and a random force. The integral involving $\Theta(t)$ describes the dissipation of energy from the primary zone to the heat bath, whereas $\boldsymbol{R}(t)$ describes the transfer of energy from the heat bath to the primary zone. The last two terms in eq. (2.82) satisfy the second fluctuation–dissipation theorem, so that the surface temperature remains constant.

The solution of eq. (2.80) or eqs. (2.81) and (2.82) gives $\boldsymbol{Y}(t)$, the trajectory of the adsorbate as a function of time. The probability of adsorption can be determined by examining a collection of trajectories calculated for different initial conditions. Since the probability of adsorption is related to the time scale of the observation (i.e., a species which adsorbs may desorb at a later time), a working definition of adsorption must be adopted. As an example of such a definition, an adsorbate can be assumed to be trapped and equilibrated with the surface if at some time in its history the total energy of the adsorbate on the surface becomes less than $-3k_bT$ [36,37]. Alternatively, one can assume that adsorption occurs when the adsorbate–surface separation distance is less than some prescribed value. Thus, the fraction of all adsorbate trajectories satisfying the working definition condition can be defined as the sticking coefficient for non-dissociative adsorption, $S^{(1)}(0)$. For dissociative adsorption of a molecule A_2, the fraction of all trajectories in which the A–A bond distance exceeds a specified value at some time is defined as $S^{(2)}(0)$ [38–43].

MD simulations can also be used to predict the diffusion coefficient of an adsorbate on a surface. For mobile diffusion, D is defined by the Einstein relationship as

$$D = \lim_{t\to\infty} \langle [\boldsymbol{Y}(t) - \boldsymbol{Y}(0)]^2 \rangle / 4t, \tag{2.83}$$

where $\langle [\boldsymbol{Y}(t) - \boldsymbol{Y}(0)]^2 \rangle$ represents the ensemble average of the mean-square displacement.

The use of MD simulations to describe the dynamics of desorption and surface reactions is limited by technical difficulties. The numerical algorithms used for the solution of eq. (2.80) or eqs. (2.81) and (2.82) require integration step lengths comparable with the time scale of the fastest motion, usually a vibrational period of 10^{-14} s. While simulation of processes which occur on the 1 to 10^3 picosecond time scale is practical, direct simulation of slow events which occur over microseconds or longer is usually prohibitive. In the case of desorption and surface reaction, the trajectory of the adsorbate must pass through a narrow region of phase space (i.e., the region of the col on the potential surface). Because such events occur infrequently, very long integration times are required if $E_d \gg k_b T$, and consequently, direct simulation of such events is impractical. As discussed below, the description of infrequent events is best handled by a dynamical form of transition-state theory.

2.4.2. Transition-state theory

In classical transition-state theory (TST), the rate for a species going from state A to state B, A → B, is defined as the equilibrium flux of adsorbate trajectories across a plane in phase space. The plane, S, which lies between the reactants and products, must be traversed at least once in going from A to B. While the location of the plane is arbitrary, it is often convenient to specify the location of S near or at the col on the potential energy surface (i.e., the transition state). Since some trajectories of species A may make multiple crossings of S before finally going to B whereas other trajectories which cross S correspond to the processes A → A or B → B, simply counting adsorbate trajectories leads to an overestimation of the rate. Thus, TST provides an upper limit to the true rate. The derivation of the TST formalism presented in the balance of this section is based on the work of Tully and coworkers [36,44].

For the process A → B, the TST equilibrium rate coefficient, k, is given by [28]

$$k = \frac{\int d\boldsymbol{p} \int d\boldsymbol{q} \int_0^\infty dv_s \, P(\boldsymbol{p}, \boldsymbol{q}, s_0, v_s) v_s \, \xi(\boldsymbol{p}, \boldsymbol{q}, v_s)}{\int d\boldsymbol{p} \int d\boldsymbol{q} \int_{-\infty}^\infty dv_s \int_{-\infty}^{s_0} ds \, P(\boldsymbol{p}, \boldsymbol{q}, s, v_s)}, \tag{2.84}$$

where the vectors $\boldsymbol{q}$ and $\boldsymbol{p}$ denote position and momenta, respectively, s is the coordinate normal to the counting plane located at s_0, and v_s is the component of velocity in the s direction. Reactant A is located in regions of phase space where $s < s_0$; conversely, product B is located in regions of phase space where $s > s_0$. The equilibrium probability density function in phase space is defined as

$$P(\boldsymbol{p}, \boldsymbol{q}, s, v_s) = N \exp[-H(\boldsymbol{p}, \boldsymbol{q}, s, v_s)/k_b T], \tag{2.85}$$

which is valid for a canonical ensemble. Here, H is the classical Hamiltonian of the system and N is a normalization constant. The factor $\xi(\boldsymbol{p}, \boldsymbol{q}, v_s)$ in eq. (2.84) is used to correct for trajectories which make multiple crossings of S or which do not contribute to the process A → B.

It is convenient to factor eq. (2.73) into [36]

$$k = k_{TST} f_s, \tag{2.86}$$

where k_{TST} is the uncorrected equilibrium rate constant given by

$$k_{TST} = \frac{\int d\boldsymbol{p} \int d\boldsymbol{q} \int_0^\infty dv_s \, P(\boldsymbol{p}, \boldsymbol{q}, s_0, v_s) v_s}{\int d\boldsymbol{p} \int d\boldsymbol{q} \int_{-\infty}^\infty dv_s \int_{-\infty}^{s_0} ds \, P(\boldsymbol{p}, \boldsymbol{q}, s, v_s)}, \tag{2.87}$$

and f_s is the dynamic correction factor given by

$$f_s = \frac{\int d\boldsymbol{p} \int d\boldsymbol{q} \int_0^\infty dv_s \; P(\boldsymbol{p}, \boldsymbol{q}, s_0, v_s) v_s \; \xi(\boldsymbol{p}, \boldsymbol{q}, v_s)}{\int d\boldsymbol{p} \int d\boldsymbol{q} \int_0^\infty dv_s \; P(\boldsymbol{p}, \boldsymbol{q}, s, v_s) \; v_s} . \tag{2.88}$$

For a canonical ensemble where H is given as the sum of kinetic and potential energy terms, eq. (2.87) can be reduced to

$$k_{\mathrm{TST}} = \left(\frac{k_b T}{2\pi m} \right)^{1/2} \frac{\int d\boldsymbol{q} \exp[-V(\boldsymbol{q}, s)/k_b T]}{\int d\boldsymbol{q} \int_{-\infty}^{s_0} ds \exp[-V(\boldsymbol{q}, s)/k_b T]} , \tag{2.89}$$

where $(k_b T/2\pi m)^{1/2}$ is the mean velocity.

Eq. (2.89) can be rewritten in terms of a one-dimensional potential of mean force, $W(s)$, defined as [44]

$$W(s) = -k_b T \ln[g(s)/g(\infty)] , \tag{2.90}$$

$$g(s) = G^{-1} \int d\boldsymbol{q} \exp[-V(\boldsymbol{q}, s)/k_b T] , \tag{2.91}$$

where G is an arbitrary normalization factor. Substitution of eqs. (2.90) and (2.91) into eq. (2.89) leads to

$$k_{\mathrm{TST}} = \left(\frac{k_b T}{2\pi m} \right)^{1/2} \frac{\exp[-W(s)/k_b T]}{\int_{-\infty}^{s_0} ds \exp[-W(s)/k_b T]} . \tag{2.92}$$

Thus, the multi-dimensional potential $V(\boldsymbol{q}, s)$ appearing in eq. (2.89) can be represented in the one dimension of the reaction coordinate, s.

In calculating k from eq. (2.84), the product $k_{\mathrm{TST}} f_s$ is independent of the location of S, but the individual terms k_{TST} and f_s are not. The most suitable position for S depends on the rate process under investigation. For desorption, placement of S far enough away from the surface so that adsorbate–surface interactions are negligible allows f_s to be equated with the thermally averaged sticking coefficient. For diffusion, the location for S is specified such that trajectories crossing the bridge sites between two surface atoms are normal to S. An alternative approach for locating is used in variational transition-state theory (VTST). In this approach, the position of S is varied to obtain the minimum value of k_{TST}, i.e., the closest approximation to k. The principal consequence of using VTST is that the effect of multiple crossings of the potential barrier is minimized. From eq. (2.92), it is evident that the VTST location of S corresponds to the maximum value of $W(s)$.

A number of techniques exist for determining the recrossing factor f_s [44–46]. An exact approach is to calculate f_s by forward and backward integration of trajectories initiated at the dividing surface S. The fraction of all trajectories which results in trapping into the product state is defined as f_s. Approximations to f_s have also been proposed. One example is the unified statistical model which predicts that f_s is given by [44]

$$f_s = \frac{\exp(W^\dagger/k_b T)}{\left[\exp(W^\dagger/k_b T) + \exp(W^{\dagger\dagger}/k_b T) - \exp(W^*/k_b T)\right]} , \tag{2.93}$$

where $W^{\dagger}$ is the higher maximum in the potential of mean force, $W^{\dagger\dagger}$ is the lower maximum, and W^{*} is the minimum that lies between the two maxima.

The unified statistical model also provides an approximation for the sticking coefficient $S^{(\alpha)}(T)$ for adsorption into the chemisorbed state [44]

$$S^{(\alpha)}(T) = \left[1 + \exp\left(W^{\mathrm{I}}/k_{\mathrm{b}}T\right) - \exp\left(W^{*}/k_{\mathrm{b}}T\right)\right]^{-1}. \tag{2.94}$$

W^{I} is the potential of mean force at the inner barrier for adsorption. If a secondary maximum or minimum does not exist, then the corresponding potential of mean force W^{I} or W^{*} is simply set equal to zero in eq. (2.94).

Dynamically corrected transition-state theory can also be used to determine the diffusion coefficient for chemisorbed species. In this case, hopping of the adsorbate is treated as if it were a reaction moving the adsorbate from site i to site j. The hopping frequency Γ_{ij} is then given by

$$\Gamma_{ij} = k_{\mathrm{TST}} f_s \tag{2.95}$$

and the diffusion coefficient is related to Γ_{ij} by

$$D = \tfrac{1}{4}\lambda^2 \Gamma_{ij}. \tag{2.96}$$

2.4.3. Absolute rate theory

It is evident from the above discussion that the evaluation of k_{TST} from eq. (2.89) requires a knowledge of $V(\boldsymbol{q}, s)$. If an accurate description of $V(\boldsymbol{q}, s)$ is not available, as is most often the case, then k_{TST} can be estimated using absolute rate theory as

$$k_{\mathrm{TST}} = \frac{k_{\mathrm{b}}T}{h}\frac{q^{\dagger}}{q_0}\exp\left[-\left(E^{\dagger} - E_0\right)/k_{\mathrm{b}}T\right], \tag{2.97}$$

where $q^{\dagger}$ and q_0 are the partition functions for the transition state and the reactant, $E^{\dagger}$ and E_0 are the energies of the transition state and the reactant, and h is Planck's constant.

To evaluate k_{TST} using eq. (2.97), estimates must be made of $q^{\dagger}$ and q_0. An accurate determination of q_0 is possible only if the reactant is in the gas phase. For a reactant in the adsorbed state, q_0 can be estimated provided some reasonable assumptions of the reactant structure and mobility can be made. Estimation of $q^{\dagger}$ is much more difficult since the exact nature of the transition-state complex is unknown, and hence, its structure and mobility cannot be defined with any accuracy. Nevertheless, it has been found [47–50] that reasonable estimates of the pre-exponential factor in k_{TST} can be made using eq. (2.97). Formulas for calculating the contributions to $q^{\dagger}$ and q_0 due to translational, rotational, and vibrational degrees of freedom

Table 1
Translational, rotational, and vibrational partition functions for molecules [47]

Molecule	Translation $r^2 2\pi m k_{\mathrm{b}}T/h^2$	Rotation $8\pi^2 k_{\mathrm{b}}TI/h^2\sigma$	Vibration $1/[1-\exp(-h\nu/k_{\mathrm{b}}T)]$
H_2	33	2.9	1.0
CO	460	180	1.0
Cl_2	1200	710	1.3
Br_2	2600	2100	1.7

Area of a unit cell, $r^2 = 10^{-15}$ cm^2; m, I, ν, and σ are the mass, moment of inertia, vibrational frequency, and symmetry number of a molecule; $T = 500$ K.

Table 2
Range of the pre-exponential factor from absolute rate theory [47]

Process	Pre-exponential factor	Units
Molecular adsorption	10^{-10}–10^{-17}	$cm^3\ s^{-1}$
Dissociative adsorption	10^{-10}–10^{-17}	$cm^3\ s^{-1}$
Molecular desorption	10^{13} –10^{-19}	s^{-1}
Associative desorption	10^{-4} –10^{4}	$cm^2\ s^{-1}$
Langmuir–Hinshelwood reaction	10^{-4} –10^{4}	$cm^2\ s^{-1}$
Eley–Rideal reaction	10^{-6} –10^{-17}	$cm^3\ s^{-1}$
Unimolecular reaction	10^{12} –10^{13}	s^{-1}
Surface diffusion	10^{-2} –10^{-4}	$cm^2\ s^{-1}$

are given in table 1. Also indicated in table 1 are the magnitudes of each partition function for four species. In table 2 are shown the range of values for pre-exponential factors which can be accounted for by absolute rate theory. It is apparent that for some surface processes, the pre-exponential factor can fall in a range which spans several orders of magnitude.

In absolute rate theory, the electronic contributions to the partition functions of the reactant and transition-state complex are factored out and expressed in the exponential factor appearing in eq. (2.97). The difference between the electronic energy states of the transition complex and the reactant, $(E^{\dagger} - E_0)$, is defined as the activation energy, E. Since absolute rate theory does not provide a means for determining E, this parameter must be estimated using one of the methods presented in section 2.1.

2.4.4. Stochastic diffusion theory

Goddard and coworkers [51] have developed a theory for the desorption of atoms and molecules from surfaces based on classical stochastic diffusion theory [52]. This approach uses a one-dimensional representation of the adsorbate–surface interaction. The flux of desorbing atoms or molecules across a plane parallel to the surface and located at s_0 is given by

$$F(s_0, u_0) = \int_{u_0}^{\infty} \mathrm{d}u\, P(s_0, u) u, \tag{2.98}$$

where $P(s_0, u)$ is the probability of finding the adsorbate at $s = s_0$ with velocity u, and u_0 is the smallest (positive) velocity for which a particle at s_0 will desorb. $P(s_0, u)$ is determined by solving the generalized Liouville equation. The effective force acting on the adsorbate and the friction constant for energy dissipation are deduced from a representation of the adsorbate–surface interactions using a generalized Langevin equation (see eqs. (2.81) and (2.82)). The final expression for $k_{\mathrm{d}}^{(1)}$ in the case of atomic desorption is

$$k_{\mathrm{d}}^{(1)} = (\Omega_0/2\pi) \exp(-E_{\mathrm{d}}/k_{\mathrm{b}}T), \tag{2.99}$$

where Ω_0 is the frequency of the vibration for the adsorbate at the bottom of the adsorbate–surface potential well and E_{d} is the apparent activation energy for desorption

$$E_{\mathrm{d}} = V(s_0) + \tfrac{1}{2} m u_0^2. \tag{2.100}$$

For molecular desorption, $k_{\mathrm{d}}^{(1)}$ is given by

$$k_{\mathrm{d}}^{(1)} = \frac{\Omega_0}{2\pi} \left(\frac{2\mu I^2 \Omega_{\mathrm{r}}^2 \gamma_0^2}{\pi k_{\mathrm{b}} T} \right) \exp(-E_{\mathrm{d}}/k_{\mathrm{b}}T), \tag{2.101}$$

where μ is the reduced mass for frustrated rotational motion of the molecule, l is the effective length of the molecule, Ω_r is the rotational frequency, and γ_0 is the maximum bending angle for the molecule. Since the molecule has rotational modes, E_d for molecules must be modified to:

$$E_d = V(s_0) + \tfrac{1}{2}mu_0^2 + \tfrac{1}{2}\mu l^2\dot{\gamma}^2 + \tfrac{1}{2}\mu l^2\Omega_r^2\gamma^2, \tag{2.102}$$

where γ is the bending angle.

2.4.5. Quantum mechanics

Quantum mechanical treatments of the dynamics of adsorption, diffusion, and desorption have, thus far, been limited to atoms and diatomic molecules, and in many instances adsorbate motion has been restricted to one dimension. A number of approaches have been used to determine rate or diffusion coefficients. Thus, for example, dissociative adsorption of a diatomic molecule [53] has been treated by solving the time-dependent Schrödinger equation

$$\psi(r, z; t) = \psi(r, z; 0)\exp[-i\boldsymbol{H}t2\pi/h], \tag{2.103}$$

where $\psi(r, z; t)$ is the wave function for the adsorbate, r is the atom–atom bond distance, z is the distance of the molecule's center of mass above the plane of the adsorption surface, and $\boldsymbol{H}$ is the Hamiltonian operator. Dissociative adsorption is assumed to occur when r exceeds a prescribed critical value. By contrast, phonon-induced desorption of atoms and molecules has been handled by determining the probability of finding an oscillator in the state n at time t, $P_n(t)$ [54,55]. The oscillators can occupy two types of states: bound states separated by discrete energy intervals or free states of continuous energy. The temporal evolution of $P_n(t)$ is governed by the master equation

$$P_n(t) = P_n(0)\exp[-\boldsymbol{W}t], \tag{2.104}$$

where $\boldsymbol{W}$ is the matrix of transition probabilities for bound–bound and bound–free transitions. The rate coefficient for desorption is then given by

$$k_d^{(1)} = \left[\sum_{n,m}(\boldsymbol{W}^{-1})_{nm}P_m(0)\right]^{1}. \tag{2.105}$$

Eq. (2.105) has also been used to determine the hopping frequency for surface diffusion [56]. In such a case, the elements of $\boldsymbol{W}$ are obtained using the potential function appropriate for diffusion.

3. Adsorption

3.1. Molecular dynamics

Arumainayagam et al. [57] have used a Langevin model to calculate $s^{(1)}(0)$ for Xe adsorption on Pt(111). Morse potentials were used to represent the Xe–surface interactions. During the course of a trajectory, adsorbate sticking was assumed to occur when the Xe–surface interactions fell below $-2k_bT$. As seen in fig. 12, the level of agreement between the experimental and predicted values of $S^{(1)}(0)$ is quite high. The authors note that this level of agreement could only be obtained by adjusting the parameters of the Morse potential responsible for the steepness of the repulsive wall and the amount of surface corrugation. The observed reduction

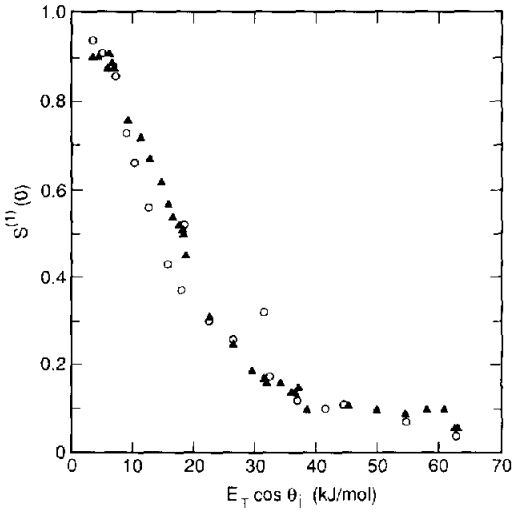

Fig. 12. Simulated (○) and experimental (▲) variation of $S^{(1)}(0)$ versus $E_T \cos \theta_i$ for Xe adsorption on Pt(111) [57]. E_T is the incident kinetic energy and θ_i is the incidence angle measured from the surface normal.

in $S^{(1)}(0)$ with increasing adsorbate kinetic energy is attributed to inefficient energy transfer between the adsorbate and the surface.

Using an approach similar to that described above, Muhlhausen et al. [58] have determined $S^{(1)}(0)$ for NO adsorption on the (111) faces of Pt and Ag. The NO–surface potential included a term to account for the orientation of NO relative to the surface. For both surfaces, $S^{(1)}(0)$ was determined to be ~ 0.7 at 300 K and to decrease monotonically to ~ 0.08 at 2000 K. The dependence of $S^{(1)}(0)$ on the incident kinetic energy of NO was also examined and $S^{(1)}(0)$ was observed to decrease with increasing kinetic energy of NO.

The sticking coefficient of Si on Si(100) has been determined by NoorBatcha et al. [59]. The adsorbate–surface potential was described by adatom–surface Morse potentials and a Keating potential to account for the bending and stretching modes of the lattice. The criterion for adsorbate sticking was an attractive interaction for a duration of more than five vibrational periods. The value of $S^{(1)}(0)$ was determined to be 0.96 at 1500 K and to be relatively insensitive to temperature.

Molecular dynamics simulations of the dissociative adsorption of H_2 on Cu(100) have been carried out by Gelb and Cardillo [38,39]. A LEPS potential energy surface was used to describe the interactions of H_2 and H with the metal surface. Dissociative adsorption was assumed to occur when the H_2 internuclear separation distance exceeded 3.5 Å. As shown in fig. 13, their calculations predict that $S^{(2)}(0)$ passes through a maximum with increasing kinetic energy of the H_2 molecule. The increase in $S^{(2)}(0)$ observed at low kinetic energies is attributed to an increase in the probability of surmounting the activation barrier for dissociative adsorption. For very large values of the kinetic energy, however, the time of interaction of the adsorbate with the surface is so small as to preclude sufficient rearrangement of the H_2 molecules into configurations favorable for dissociation, and hence, the value of $S^{(2)}(0)$ decreases as the kinetic energy increases.

Lee and DePristo [41–43] have reported on the dissociation kinetics of H_2 on Ni and Cu crystal faces. A generalized Langevin model was used to simulate adsorbate trajectories and a LEPS potential energy surface was used to describe the H_2– and H–metal interactions.

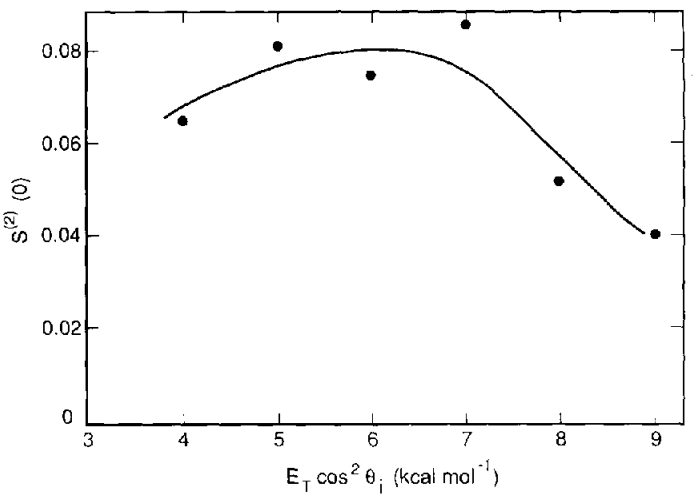

Fig. 13. Simulated (●) variation of $S^{(2)}(0)$ versus $E_T \cos^2\theta_i$ for H_2 adsorption on Cu(100) [39]. E_T is the incident kinetic energy and θ_i is the incidence angle measured from the surface normal. The solid line is a guide to the eye.

Table 3
Dissociative sticking probability of hydrogen on Cu surfaces for $T_s = 1000$ K [41]

Kinetic energy (eV)	Cu(110)		Cu(100)	
	Calc.	Exp. [a]	Calc.	Exp. [a]
0.15	0.03	0.08	< 0.01	0.03
0.20	0.06	0.115	0.01	0.045
0.30	0.11	0.135	0.06	0.095
0.40	0.15	0.14	0.10	0.100
0.60	0.27	–	0.27	–

[a] From refs. [60,61].

Table 4
Dissociative sticking probability of hydrogen on Ni surfaces for $T_s = 300$ K [41]

Kinetic energy (eV)	Ni(100)		Ni(110)		(Ni(111)	
	Calc.	Exp. [a]	Calc.	Exp. [b]	Calc.	Exp. [b]
0.03	0.17	0.4	0.55	0.96	0.09	0.02
0.05	0.18	0.6	0.52	0.96	0.08	0.07
0.07	0.18	0.7	0.52	0.96	0.09	0.10
0.10	0.20	0.8	0.52	–	0.09	0.27
0.14	0.20	–	0.52	–	0.10	–
0.20	0.20	–	0.50	–	0.12	–

[a] From refs. [62].
[b] From refs. [63].

Dissociative adsorption was assumed to occur when the H_2 internuclear separation distance exceeded 2.8 Å. A comparison of the predicted and experimental values of $S^{(2)}(0)$ as a function of incident kinetic energy of the adsorbate is given in tables 3 and 4. For the Cu surfaces, both

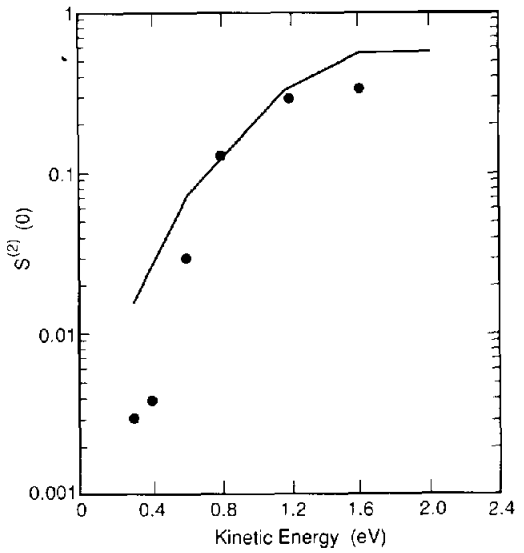

Fig. 14. Simulated (solid line) [64] and experimental (circles) [65] variation of $S^{(2)}(0)$ versus incident kinetic energy for N_2 adsorption on W(110).

the predicted values of $S^{(2)}(0)$ and the dependence of these values on kinetic energy are in fair agreement with the experimental observation [60,61], whereas for the Ni surfaces, the predicted values of $S^{(2)}(0)$ and the dependence on kinetic energy do not agree well with the experimental data [62,63]. Using the same approach, Kara and DePristo [64] have calculated $S^{(2)}(0)$ for N_2 adsorption on W(110). As can be seen in fig. 14, the agreement between theory and experiment [65] is very good in this case.

3.2. Transition-state theory

The influence of precursor states on molecular adsorption has been examined by Doren and Tully [44] using dynamic TST. In their model, adsorbate–surface interactions were described by a one-dimensional potential of mean force $W(z)$, which depends only on z, the distance of the molecular center of mass from the surface. The presence of a precursor state was defined by the occurrence of a secondary minimum in $W(z)$, located between the chemisorbed state and z approaching infinity. As illustrated in fig. 15a for the case of CO adsorption on Ni(111), the depth of the well for the precursor state decreases with increasing temperature, whereas the height of the activation barrier for dissociative adsorption increases. Fig. 15b shows that the sticking coefficient for molecular adsorption of CO first decreases and then gradually increases with increasing temperature. This behavior can be explained as follows. At low temperatures, the kinetic energy of the impinging adsorbate is small and consequently very little energy transfer is required for the adsorbate to be trapped into the precursor state. Since the barrier for subsequent trapping into the adsorbate state is small at low temperatures, adsorption into that state proceeds rapidly and hence $S^{(1)}(0)$ is large. At intermediate temperatures, the activation energy barrier becomes more pronounced (see fig. 15a), and the inability of adsorbates to surmount this higher barrier leads to lower values of the sticking coefficient. At high temperatures, the kinetic energy of the incident molecules is now sufficient to directly overcome the activation energy barrier without initial trapping into the precursor state. The

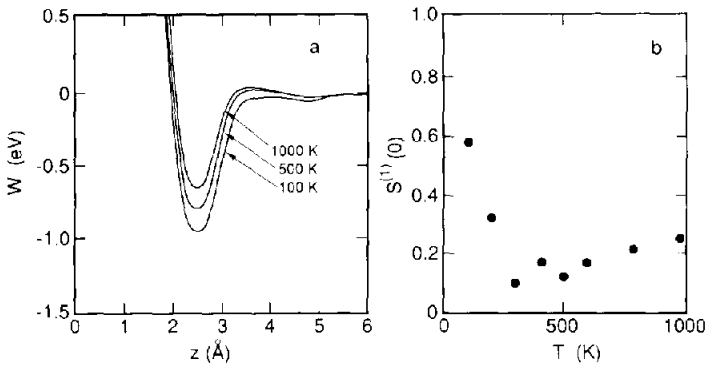

Fig. 15. (a) Potential of mean force versus height above the surface for CO on Ni(111). (b) Simulated variation of $S^{(1)}(0)$ versus T for CO adsorption on Ni(111) [44].

Table 5
Activation energy (kcal/mol) for dissociative adsorption of hydrogen and deuterium on Ni surfaces [66]

T (K)	Ni(100)		Ni(110)		Ni(111)	
	H_2	D_2	H_2	D_2	H_2	D_2
100–140	−0.87	−1.31	0.29	0.10	0.99	0.61
140–200	−1.23	−1.02	0.35	0.09	0.92	0.63
200–300	−1.01	−0.67	0.40	0.05	0.86	0.70
300–500	−0.71	−0.30	0.37	−0.05	0.94	1.11
500–800	0.16	0.54	−0.28	−0.29	1.59	2.21

behavior observed at low and high temperatures is referred to in the literature as precursor-mediated adsorption and direct adsorption, respectively.

Truong et al. [66] have used a variational TST approach which included quantum effects to determine the activation energy for dissociative adsorption, E_{diss}, of H_2 and D_2 on Ni(100), (111), and (110) surfaces. The adsorbate–surface interactions were described by a LEPS potential energy surface. To account for the quantum effects of tunneling and reflection, k_{TST} was multiplied by a ground-state transmission coefficient. The apparent activation energies are listed in table 5. As can be seen, the value of E_{diss} depends on the crystal face, the temperature, and the molecular weight of the adsorbate. For H_2 adsorption on Ni(100), E_{diss} is negative up to 500 K, indicating that the classical barrier to desorption lies below the reactant energy. On Ni(110), the value of E_{diss} is less than or equal to 0.4 kcal/mol below 500 K, whereas on Ni(111), it is about 1.0 kcal/mol below 500 K. The complex dependence of E_{diss} with temperature for both H_2 and D_2 is partially attributable to the effects of tunneling.

Adams and Doll [67] have also used a dynamic TST model to examine the influence of precursor states on the sticking coefficient for dissociatively adsorbed species. Their calculations suggest that $S^{(2)}(0)$ decreases with increasing temperature and is sensitive to the well depth in the precursor state and the rate of energy dissipation in the adsorbed state.

3.3. Quantum mechanical models

A quantum mechanical description of H_2 adsorption on Ni(100) has been developed by Jackson and Metiu [53]. The interactions of H_2 and H with the metal surface were described by

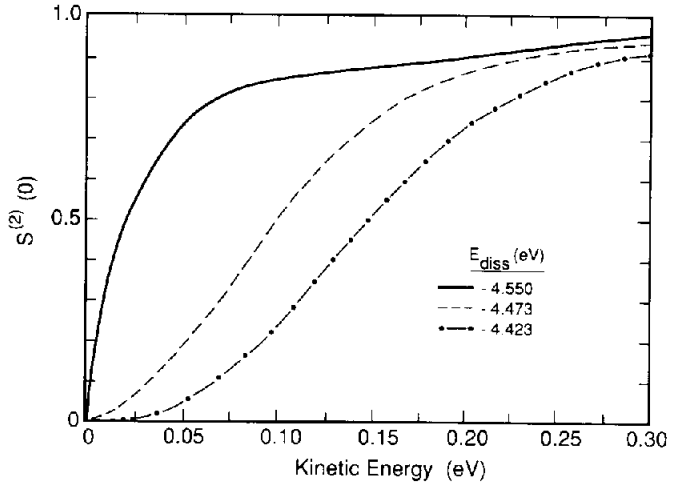

Fig. 16. Simulated variation of $S^{(2)}(0)$ versus incident kinetic energy for H_2 adsorption on Ni(100) [53]. E_{diss} is the activation barrier for H_2 dissociation.

a LEPS potential energy surface. The principal features of the energy surface are the barriers for molecular adsorption, E_a, dissociation, E_{diss}, and atomic diffusion, E_{diff}. The adsorption behavior depends on the relative magnitudes of E_a and E_{diss}. When $E_a = 0$ and $E_{diss} < E_{diff}$ (restricted adsorbate mobility), the dissociation probability $S^{(2)}(0)$ is larger than when $E_a = 0$ and $E_{diss} > E_{diff}$ (mobile adsorbate). This behavior is attributed to the fact that restriction of adsorbate mobility increases the probability for H-atom recombination and hence, lowers the value of $S^{(2)}(0)$. As can be seen in fig. 16, $S^{(2)}(0)$ increases with increasing kinetic energy and is smaller for the larger values of E_{diss}. The quantum nature of the dissociation process is especially evident for $E_{diss} = -4.423$ eV. Classically, dissociation should occur with unit probability for all kinetic energies, since E_{diss} is below the zero-point energy of H_2. The process of quantum reflection upon traversing a potential change, however, leads to much lower values of $S^{(2)}(0)$.

Using an approach similar to the one described above, Chiang and Jackson [40] have investigated the isotope effect for adsorption of H_2, D_2 and T_2 on Ni(100). Their calculations show that for a fixed value of the incident kinetic energy, $S^{(2)}(0)$ decreases with increasing molecular weight. This behavior arises from the influence of the zero-point energy on the apparent barrier to dissociation. In qualitative agreement with this prediction, Hamza and Madix [62] have observed larger values of $S^{(2)}(0)$ for H_2 dissociation on Ni(100) than for D_2.

Asscher et al. [68] have calculated $S^{(2)}(0)$ for N_2 on Re(0001) and Fe(111). The principal feature of the potential energy surface is an activation energy barrier to dissociation $E_{diss} = 73$ kJ/mol. The calculated value of $S^{(2)}(0)$ increases exponentially with increasing incident kinetic energy, in agreement with the experimental results for N_2 on Fe(111) [69]. The low values of $S^{(2)}(0)$ observed for low initial kinetic energies are attributed to the large activation energy for dissociation. It is interesting to note that classically, non-zero values of $S^{(2)}(0)$ would not have been expected at low kinetic energies for such a large value of E_{diss}; the observation of a finite value of $S^{(2)}(0)$ is thus attributable to tunneling of the molecular wave function through the barrier.

A quantum wave packet calculation for dissociative adsorption of H_2 on Cu(100) has recently been reported by Nielsen et al. [70]. In this study, the adsorbate–metal potential was

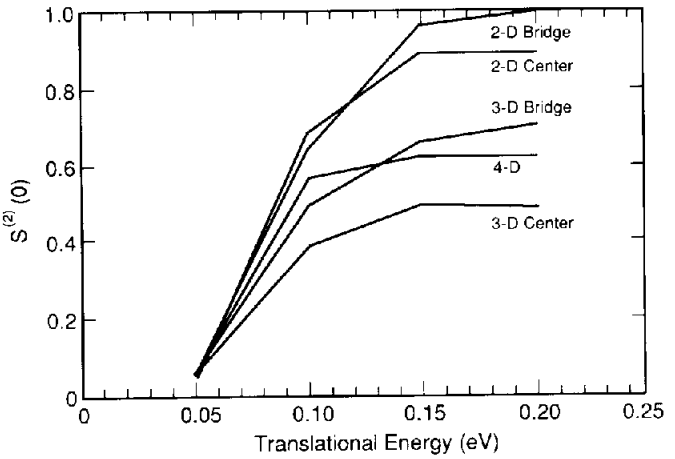

Fig. 17. Simulated variation of $S^{(2)}(0)$ versus incident kinetic energy for H_2 adsorption on Cu(100) [70].

defined within the effective medium approximation [71]. Calculations of $S^{(2)}(0)$ versus translational energy were obtained for two-, three-, and four-dimensional simulations. In the two-dimensional simulations the H–H axis was chosen to be parallel to the surface and the center of mass was constrained to be either above a bridge site or a center (four-fold hollow) site. For the three-dimensional simulations the center of mass was again constrained to be over a bridge or center site, but the H_2 molecule could undergo "cartwheel" rotations in a plane parallel to the metal surface. The four-dimensional calculations were similar to the three-dimensional calculations but the center of mass was allowed to translate freely within the plane of rotation. The results presented in fig. 17 show that by including the rotational degrees of freedom, the dissociation probability at high energies saturates at a value significantly less than unity. This is because those molecules aligned with their axis parallel to the surface normal, have an unfavorable dissociation geometry, and are scattered into the gas phase. The authors note, however, that comparison with measured values of $S^{(2)}(0)$ for H_2 on Cu surfaces [72,73], suggests that the potential used in their calculations underestimates the magnitude of the activation barrier.

3.4. Effects of lateral interactions

As discussed in section 2.2, lateral interactions can affect the sticking coefficient for both dissociative and non-dissociative adsorption. King and Wells [32] have used a lattice-gas model in combination with a precursor mechanism to describe the dissociative adsorption of N_2 on a

Table 6
Values of the parameters used to represent the data in fig. 18 [32]

T_s (K)	N_s (10^{14} cm^{-2})	L	$\eta/2$	$S^{(2)}(0)$
300	9.5	0.082	0.989	0.585
433	10.0	0.157	0.987	0.49
663	10.5	0.256	0.977	0.31
773	9.5	0.517	0.986	0.21

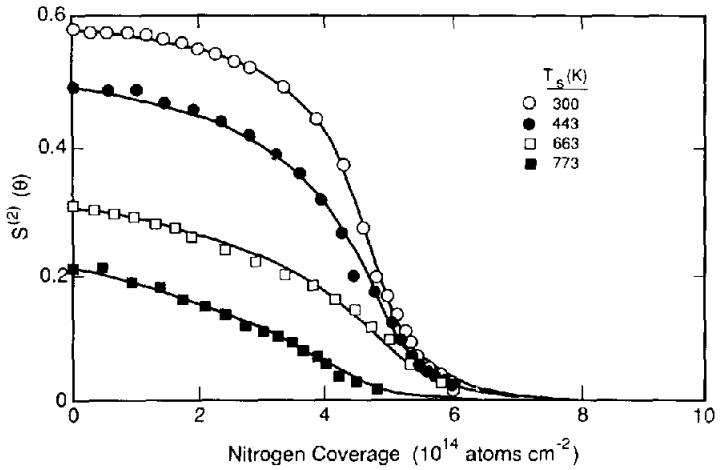

Fig. 18. Experimental and predicted variation in $S^{(2)}(\theta)$ versus coverage for N_2 adsorption on W(100) [32].

W(100) surface (see eq. (2.47)). Values of the parameters required to fit eq. (2.47) to the experimental data are listed in table 6, and a comparison of the fitted and experimental results is shown in fig. 18. Good agreement is observed at both low and high temperatures. It is interesting to note that L increases with increasing temperature, a trend which reflects the temperature dependence of the desorption rate.

The adsorption of molecular N_2 on Ru(001) has been simulated by Hood et al. [74] using a Monte Carlo model. Adsorption was assumed to proceed via a precursor mechanism in which both intrinsic and extrinsic precursor sites could be occupied. Repulsive nearest-neighbor interactions between precursor and chemisorbed species were taken to be 0.25 kcal/mol and attractive next-nearest neighbor interactions were taken to be 0.45 kcal/mol. As seen in fig. 19, the predicted variation in $S^{(1)}(\theta)$ is in fair agreement with the experimentally observed trend [75,76]. The initial rise in $S^{(1)}(\theta)$ is attributed to the formation of energetically favorable islands in which molecules are arranged in $\sqrt{3} \times \sqrt{3}\,\mathrm{R}30^\circ$ domains, whereas the decrease in $S^{(1)}(\theta)$ at high coverage is attributed to crowding effects.

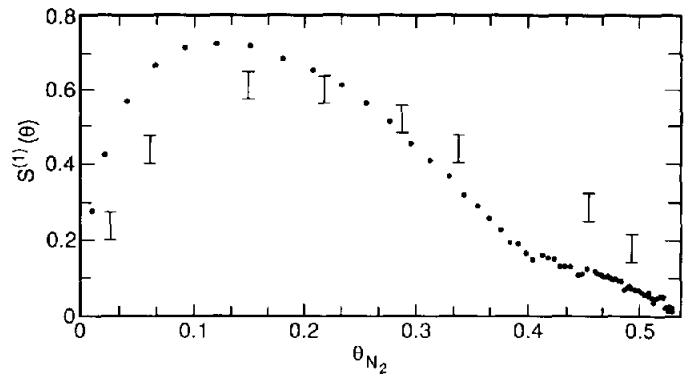

Fig. 19. Experimental (error bars) [75,76] and predicted (●) [74] variation in $S^{(1)}(\theta)$ versus coverage for N_2 adsorption on Ru(001).

4. Diffusion

4.1. Molecular dynamics

McDowell and Doll [77–80] have used MD simulations to determine the self-diffusivity of W and Rh atoms on well-defined surfaces of these metals. The interactions of the adsorbate and surface atoms in all the simulations were described by Lennard-Jones potentials, and motion of the top 1–2 layers of the surface was included in the calculations. Table 7 lists the predicted and experimental values of E_{diff} and D_0. In general, the predicted values of E_{diff} and D_0 agree well with the experimentally determined quantities. It was also noted that increasing the number of moving layers from 1 to 2 led to only a small increase in the calculated diffusivities.

The diffusivities of C and O on Pt(111) have been calculated by Doll and Freeman [87] from MD simulations in which the adsorbate–metal interactions were described by Lennard-Jones potentials. The pre-exponential factor D_0 and the activation energy E_{diff} for carbon were determined to be 3.4×10^{-3} cm^2/s and 26.1 kcal/mol whereas for oxygen these quantities were 1.5×10^{-3} cm^2/s and 18.1 kcal/mol. The predicted value of E_{diff} for carbon is smaller than the experimentally observed value of 31 ± 4 kcal/mol [88], and for oxygen, the predicted value of E_{diff} is somewhat larger than that observed experimentally, 16 kcal/mol for oxygen [89].

Levine and Garofalini [90] have also examined the diffusivity of O on Pt(111) with an MD approach. The predicted values of E_{diff} and D_0 from these simulations agree reasonably with the values determined by Doll and Freeman [87] quoted above.

The self-diffusion of Si on Si(100) has been modelled by NoorBatcha et al. [59]. The adsorbate–metal potential energy surface was described by Morse potentials and the interactions between Si atoms in the lattice were represented by a Keating potential. The values of D_0

Table 7
Arrhenius parameters for atomic self-diffusion [77]

Atom/surface	D_0 (cm^2/s)		E_{diff} (kcal/mol)	
	Exp.	Calc.	Exp.	Calc.
W/W(110)	2.1×10^{-3} [a]		19.8 [a]	
	2.6×10^{-3} [b]		21.2 [b]	
	6.2×10^{-3} [c]		20.8 [c]	
Average	3.6×10^{-3}	$3.59 \pm 1.77 \times 10^{-3}$	20.6	22.7 ± 3.0
W/W(211)	3.0×10^{-4} [d]		17.5 [d]	
	1.2×10^{-4} [e]		16.8 [e]	
	2.0×10^{-2} [f]		19.7 [f]	
	2.0×10^{-3} [f]		17.8 [f]	
Average	5.6×10^{-3}	$2.18 \pm 2.72 \times 10^{-3}$	18.0	20.5 ± 5.2
Rh/Rh(111)	2×10^{-4} [b]	$7.10 \pm 1.28 \times 10^{-4}$	3.6 [b]	6.2 ± 0.6
Rh/Rh(100)	1×10^{-3} [b]	$4.06 \pm 2.34 \times 10^{-3}$	20.2 [b]	20.8 ± 3.7

[a] From ref. [81].
[b] From ref. [82].
[c] From ref. [83].
[d] From ref. [84].
[e] From ref. [85].
[f] From ref. [86].

and E_{diff} for Si diffusion were determined to be $6.35 \pm 1.44 \times 10^{-4}$ cm^2/s and 3.63 ± 0.47 kcal/mol. The predicted activation energy is comparable to that determined experimentally, 4.6 kcal/mol for Si on Si(111) [91].

4.2. Transition-state theory

Voter and Doll [92] have used dynamic TST to determine the self-diffusivity of Rh on Rh(100). The adsorbate–surface interactions were described by Lennard-Jones potentials and the diffusivities were calculated using eq. (2.85). As shown in fig. 20, the predicted and experimentally determined self-diffusivities are in good agreement. The predicted values of D_0 and E_{diff} for Rh atoms are $6.6 \pm 0.06 \times 10^{-3}$ cm^2/s and 23.82 ± 0.05 kcal/mol, whereas the experimentally determined quantities are 10^{-3} cm^2/s and 20.2 ± 1.7 kcal/mol [82].

The diffusivity of hydrogen on a rigid Cu(100) surface has been investigated by Valone et al. [93] and Lauderdale and Truhlar [94]. Although the approaches used by these authors were based on classical TST, quantum effects were included in both models. Valone et al. [93] treated all motion classically. Quantum effects were incorporated by use of an effective potential which accounts for the effects of zero-point energies and tunneling. Lauderdale and Truhlar [94], on the other hand, treated motion along the reaction coordinate classically, whereas other modes of motion were treated quantum mechanically. The classical motion in the reaction coordinate, however, was multiplied by a semi-classical transmission coefficient to account for zero-point energies and tunneling. In both studies, the inclusion of quantum effects was shown to lead to a non-Arrhenius dependence of the diffusivity at low temperatures. Lauderdale and Truhlar [94] were able to show that the major source of the non-Arrhenius behavior is tunneling. Both Valone [93] and Lauderdale and Truhlar [94] found the ratio of the diffusion coefficient determined from quantum mechanics to that determined from classical mechanics to be of order 10^3 for H and 10 for D at 120 K. This level of agreement is remarkable in view of the differences in the formalisms used.

The two models discussed above were extended to examine the influence of the lattice motion on the diffusivity of hydrogen. In the work reported by Valone et al. [95], only atoms in the topmost layer were allowed to move, whereas in the work reported by Lauderdale and Truhlar [96] and Truong and Truhlar [97,98], both surface and subsurface atom movement was

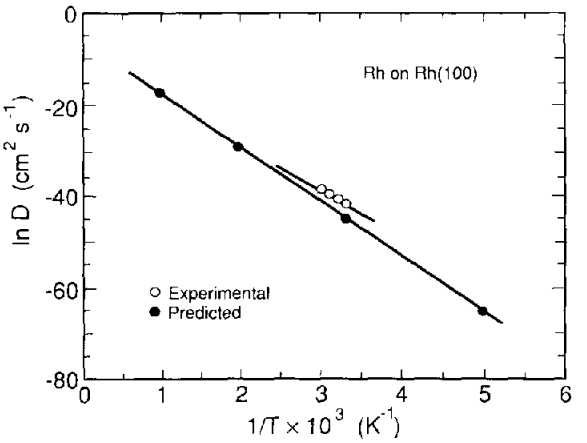

Fig. 20. Experimental [82] and predicted [92] variation in D versus $1/T$ for Rh diffusion on Rh(100).

included. Each of these studies showed that movement of the substrate resulted in larger values of the diffusivity for both H and D, the effect being most pronounced at low temperature. At 100 K, the diffusivity for H on a moving surface was 10 to 10^3 larger than that for H on a rigid surface.

The diffusion of H on Ru(001) in the temperature range 260–330 K has been simulated by two groups. In the work of Mak and George [99], the H–surface potential was described by a sum of pairwise-additive Morse potentials whereas in the study by Truong et al. [100], an ab-initio potential was used. The values of D_0 and E_{diff} determined by Mak and George [99] were 2.2×10^{-3} cm^2 s^{-1} and 3.84 kcal/mol, respectively, whereas the corresponding values calculated by Truong et al. [100] were 10^{-3} cm^2 s^{-1} and 4.1 ± 0.5 kcal/mol. The values of D_0 predicted in both studies are larger than the experimentally determined value of $D_0 = 6.3 \times 10^{-4}$ cm^2 s^{-1} [101]. The value of E_{diff} determined experimentally is 4.0 kcal/mol [101] and falls between the two predicted values.

4.3. Quantum mechanical models

Auerbach et al. [102] have used a quantum mechanical model to treat the diffusion of hydrogen at low coverage on W(110). The model takes into account the effects of phonon–adsorbate interactions on the motion of the adsorbate. At low temperature, the adsorbate motion arises from phonon-assisted tunneling whereas at high temperature, the motion occurs by an activated hopping process. Fig. 21 shows the predicted and experimentally determined [103,104] diffusivities as a function of temperature. It can be seen that the model successfully represents the experimentally observed trends. The model developed by Auerbach et al. [102] also predicts that in the activated diffusion regime, the pre-exponential factor for diffusion increases exponentially with increasing mass of the adsorbate, a trend which, although opposite to the classical isotope dependence, is in accord with the experimentally observed mass dependence of the pre-exponential factor for hydrogen on W(110) [104].

The coverage dependence of the diffusivity of hydrogen on W(110) has been determined by Whaley et al. [105] using a model which accounts for the band structure of hydrogen atoms in a

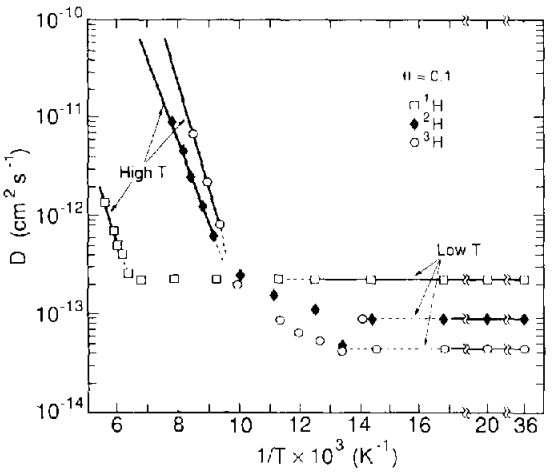

Fig. 21. Variation in D with $1/T$ for hydrogen diffusion on W(110). Symbols are the experimental data [103,104] and the lines are the model predictions [102].

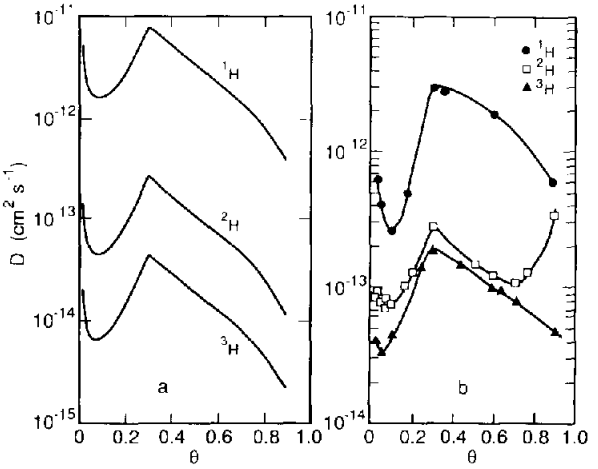

Fig. 22. (a) Predicted variation in D with θ for hydrogen diffusion on a metal surface at 27 K [105]. (b) Experimental variation in D with θ for hydrogen diffusion on W(110) at 27 K [104].

periodic surface potential. The model differentiates between low- and high-coverage diffusion. At low coverage, the hydrogen motion is described by a random collision process in a uniform potential, whereas at high coverage, the hydrogen motion is affected by the perturbations of nearest-neighbor H–H interactions on the surface potential. The predicted diffusivities for the isotopes of hydrogen are shown in fig. 22a and display a complex coverage dependence. For comparison, the experimentally observed diffusivity profiles with coverage are shown in fig. 22b [104]. With the exception of the deuteron profile at high coverage, the model predictions agree qualitatively with the experimental results.

4.4. Effects of lateral interactions

Monte Carlo simulations of the diffusive motion of an ensemble of adsorbates have been carried out to explore the effects of lateral interactions on $D(\theta)$. The advantage of this approach is that is does not require use of the QCA, and, hence, allows consideration of the effects of non-equilibrium adsorbate configurations.

Adsorbate atoms or molecules are assumed to be located at fixed positions on a lattice of surface sites. The hopping of adsorbates from site i to site j can be described by P_{ij}, a transition probability which depends on the configuration of nearest-neighbor sites surrounding the initial and final sites. Simulations begin by first choosing an adsorbate at random and then selecting one of the z nearest-neighbor sites. If the neighboring site is occupied, the procedure is begun again. If the neighboring site is unoccupied, the hopping probability P_{ij} is computed and compared to a random number R ($0 \leq R \leq 1$). The adsorbate is moved from site i to site j if $R \leq P_{ij}$, otherwise it remains in its original position. Each time an adsorbate is selected, the time is increased by an amount $\Delta t = \tau/N$, where $1/\tau$ is the attempt frequency of hops and N is the number of adsobates in the ensemble. The surface diffusion coefficient, D, is calculated from the ensemble average of the mean-square displacement of adsorbates using eq. (2.83).

The transition probability P_{ij} discussed above can be described in terms of an activation energy for diffusion, E_{diff}, or an energy difference between sites i and j, $\Delta E = Q_j - Q_i$. In the

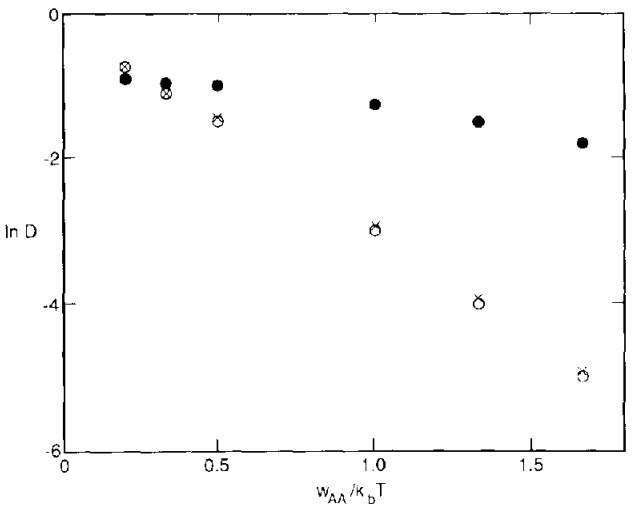

Fig. 23. Variation in D with w_{AA}/k_bT [108]. The open circles are from simulations using eq. (4.1) and the closed circles are from simulations using eq. (4.3). The crosses are the rescaled diffusivities from eq. (4.3).

presence of lateral interactions, both E_{diff} and ΔE depend on the configuration of nearest-neighbor sites surrounding the initial and final sites. If adsorbate diffusion is characterized by E_{diff}, P_{ij} is given by

$$P_{ij} = \exp(-E_{diff}/k_bT). \tag{4.1}$$

If the representation of adsorbate diffusion is in terms of the energy difference ΔE, P_{ij} can be described by either Metropolis [106] or Kawasaki [107] dynamics. For Metropolis dynamics,

$$P_{ij} = \begin{cases} \exp(-\Delta E/k_bT), & \text{for } \Delta E > 0, \\ 1, & \text{for } \Delta E \leq 0. \end{cases} \tag{4.2}$$

For Kawasaki dynamics,

$$P_{ij} = \frac{\exp(-\Delta E/k_bT)}{1 + \exp(-\Delta E/k_bT)}. \tag{4.3}$$

Kang and Weinberg [108] have recently discussed the proper specification of P_{ij} and τ required to correctly represent the dynamics of diffusion. Their analysis shows that P_{ij} must be written as given in eq. (4.1) and $\tau = 1/\nu_{diff}$, where ν_{diff} is the frequency of frustrated translation motion parallel to the surface. It was also shown that specification of P_{ij} using either Kawasaki or Metropolis dynamics does not produce a proper description of the surface dynamics. This is demonstrated in fig. 23 which shows plots of D versus $1/T$ for two representations of P_{ij}. In one case, P_{ij} is given by the energy barrier model (eq. (4.1)) whereas in the other, P_{ij} is given by Kawasaki dynamics (eq. (4.3)). As seen in fig. 23, the two models lead to different dependences of the diffusivity with temperature. Kang and Weinberg [108] indicate, however, that the diffusivities determined from Kawasaki dynamics can be brought into agreement with those determined from the energy barrier model by rescaling τ. The diffusivities determined from the rescaled Kawasaki model are also shown in fig. 23 and are seen to be in good agreement with the diffusivities predicted from the energy barrier model. In general, though, the rescaling factor is not known and thus accurate diffusivities can only be obtained from the energy barrier model.

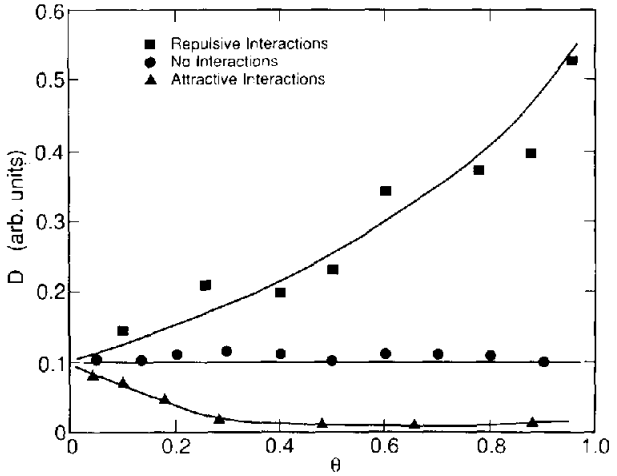

Fig. 24. Variation of D with θ for repulsive (■), attractive (▲), and no nearest-neighbor interactions (●) [109].

Bowker and King [109] have used a Monte Carlo model to investigate the influence of lateral interactions on the diffusivity. Lateral interactions were described in a pairwise additive manner. Concentration gradients were established on a two-dimensional array and jumps of adsorbates between sites were monitored as a function of coverage and time. Coverage-dependent diffusivities were then obtained for the three cases of repulsive, attractive, and no interactions between adsorbates. As seen in fig. 24, D increases with increasing θ for repulsive interactions, whereas it decreases with increasing θ for attractive interactions. In the absence of

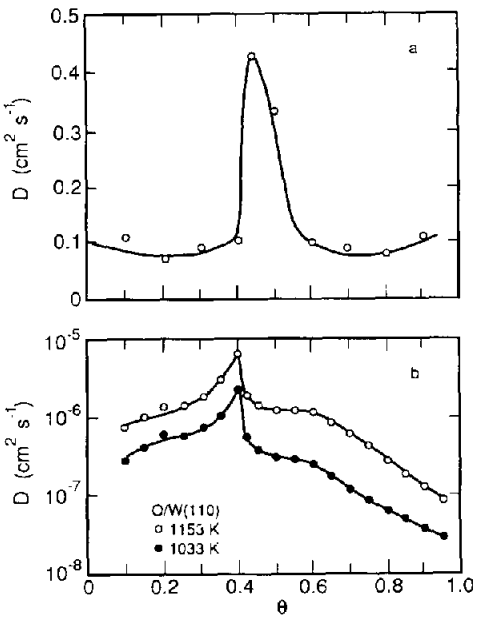

Fig. 25. (a) Simulation of the θ dependence of D for repulsive nearest-neighbor and attractive next-nearest-neighbor interactions [110]. (b) Experimental variation in D with θ for oxygen on W(110) [111].

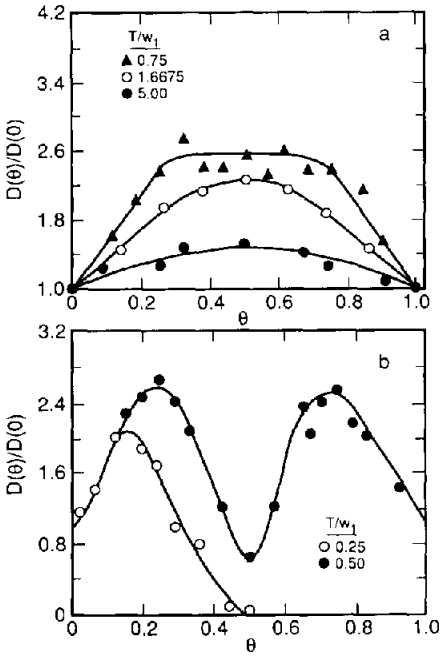

Fig. 26. Variation in $D(\theta)/D(0)$ with θ for equivalent nearest- (w_1) and next-nearest- (w_2) neighbor repulsive interactions [114]; (a) disordered region; (b) ordered region.

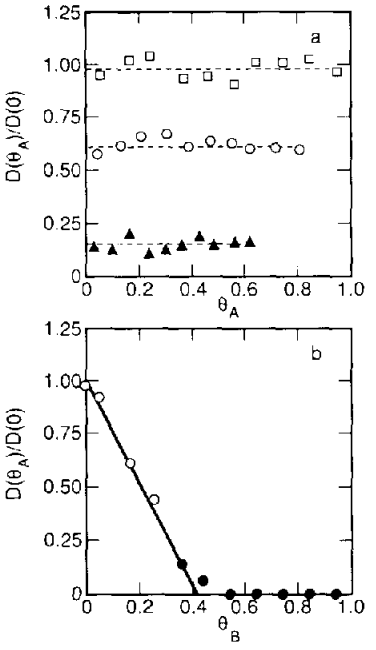

Fig. 27. (a) Variation in $D(\theta_A)/D(0)$ with θ_A in the presence of an immobile adsorbate B for $\theta_B = 0$ (□), $\theta_B = 0.15$ (○), and $\theta_B = 0.36$ (△). (b) Variation in $D(\theta_A)/D(0)$ with θ_B. The filled symbols represent upper limits [115].

lateral interactions, D is coverage-independent. Bowker and King [110] have also examined the influence of repulsive nearest-neighbor and attractive next-nearest neighbor interactions on D. Fig. 25a shows that the predicted profile of D goes through a maximum near $\theta = 0.45$. This type of coverage dependence is qualitatively similar to that observed experimentally for oxygen diffusion on W(110), which is shown in fig. 25b [111].

Tringides and Gomer [112] have also simulated the diffusion of oxygen on W(110) using a Monte Carlo model. Both pairwise and triplet interactions between adsorbates were considered. The experimentally observed [113] increase in the activation energy and pre-exponential factor with increasing coverage were accounted for with nearest-neighbor interactions of 2.1 kcal/mol, next-nearest-neighbor interactions of -0.7 kcal/mol, and triplet interactions of -1.2 or 0 kcal/mol.

The effects of adsorbate coverage on the diffusion coefficient for ordered or disordered adsorbates have been modelled by Sadiq and Binder [114]. Fig. 26a shows that for disordered adsorbates, the diffusivity goes through a maximum as a function of coverage. Simulations were also conducted for a case in which the adsorbates can form an ordered overlayer at $\theta = 0.5$. As seen in fig. 26b, the diffusion coefficient exhibits maxima at $\theta = 0.33$ and $\theta = 0.67$. The minimum at $\theta = 0.5$ is attributed to the formation of an ordered surface overlayer which causes a reduction in the diffusivity.

Mak et al. [115] have examined the effect of an immobile species B on the diffusivity of a mobile species A assuming no lateral interactions. Fig. 27a displays the dependence of $D(\theta_A)/D(0)$ on θ_B. $D(\theta_A)/D(0)$ is seen to decrease with increasing coverage of B. On the other

hand, $D(\theta_A)/D(0)$ decreases linearly with θ_B, as shown in fig. 27b. The intercept with the abscissa at $\theta_B = 0.408$ is in agreement with percolation estimates for the coverage of B above which no further diffusion of A can occur.

5. Desorption

5.1. Transition-state and stochastic diffusion theory

Tully and coworkers [36,37] have calculated the rate coefficients for Xe and Ar desorption from Pt(111) using both dynamically corrected (eq. (2.75)) and classical (eq. (2.76)) TST. The results of these calculations are illustrated in fig. 28. At low temperatures, both approaches give identical results, indicating that f_s goes to 1.0 as the temperature decreases. It is also observed that at low temperatures, $k_d^{(1)}$ exhibits Arrhenius behavior. The apparent activation energies for Ar and Xe desorption are 8.8 and 28.8 kJ/mol, respectively, in good agreement with the experimental values of 9.2 and 29.3 kJ/mol [116,117]. In the limit of low temperatures, the apparent pre-exponential factors for Ar and Xe are 5.2×10^{11} and 6.8×10^{11} s^{-1}, respectively, which agree approximately with the vibrational frequencies of the rare-gas atoms on the surface: 9.8×10^{11} s^{-1} for Ar and 9.2×10^{11} s^{-1} for Xe. Fig. 28 shows that with increasing temperature above 200 K, the value of $k_d^{(1)}$ predicted by dynamically corrected TST becomes progressively smaller than that calculated by classical TST. This deviation is a reflection of the decreasing value of f_s [i.e., $S^{(1)}(0)$] as T increases. The non-Arrhenius behavior of $k_d^{(1)}$ is explained in the following way. At high temperatures, the mean energy transferred upon impact of the rare-gas atom with the surface is relatively small and so consequently equilibrium can no longer be maintained among adsorbates located near the top of the potential well. This causes a depletion in the population of the precursor levels due to desorption into the gas phase and hence, to a reduction in the rate of desorption.

Using an approach similar to that described above, Muhlhausen et al. [58] have examined the molecular desorption of NO from Pt(111). The rate of NO desorption exhibited Arrhenius

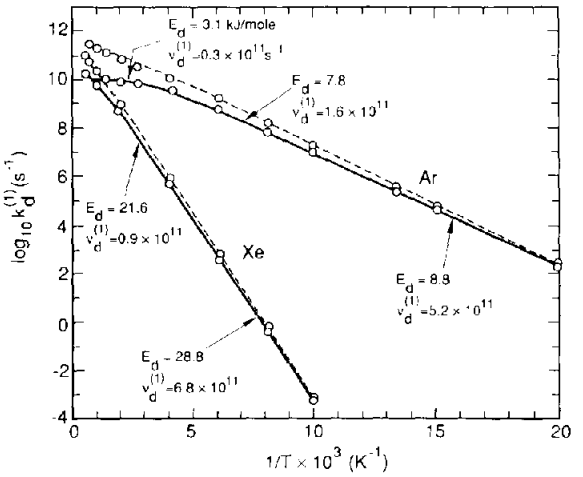

Fig. 28. Arrhenius plot for Ar and Xe desorption from Pt(111). Solid and dashed curves are dynamically corrected and uncorrected TST, respectively [37].

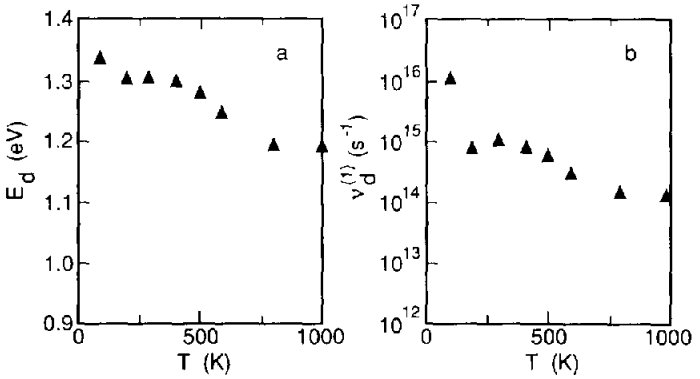

Fig. 29. Activation energy (a) and pre-exponential factor (b) profiles versus T for CO desorption from Ni(111) [44].

behavior at low temperature, but at temperatures above 1000 K, curvature was observed. This high temperature behavior was explained in the same manner as that for Xe and Ar desorption, discussed above. The pre-exponential factor determined from the low-temperature portion of the Arrhenius plot was $10^{16\pm0.4}$ s^{-1}, in excellent agreement with the experimental value of 10^{16} s^{-1} [118]. This value of $\nu_d^{(1)}$, which is larger than the value of 10^{13} s^{-1} often assumed, is ascribed by the authors to the reduced entropy of chemisorption associated with the alignment of the molecule perpendicular to the surface.

Doren and Tully [44] have calculated $k_d^{(1)}$ for CO desorption from Ni(111) using dynamic TST. Fig. 29 illustrates plots of the apparent Arrhenius parameters E_d and $\nu_d^{(1)}$ versus temperature. Both the activation energy and the pre-exponential factor are seen to be temperature-dependent and to decrease with increasing temperature. For temperatures between 400 and 600 K, $\nu_d^{(1)}$ is in the range of 10^{14} to 10^{15} s^{-1}. The explanation for this large value of $\nu_d^{(1)}$ for CO is identical to that presented above for NO.

The associative desorption of H_2 from Si(111) has been modelled by Raff et al. [119] with a variational TST approach. The potential energy surface was defined by the sum of three terms corresponding to the lattice potential, adatom–lattice interactions, and adatom–adatom interactions. The rate coefficient $k_d^{(2)}$ exhibited Arrhenius behavior over the temperature range investigated. The apparent activation energy and pre-exponential factor were 55 kcal/mol and 0.20 cm^2 s^{-1}, respectively. These values lie within the range of the experimentally observed values of 41–59 kcal/mol for the activation energy and 0.03–136 cm^2 s^{-1} for the pre-exponential factor [120–122].

Stochastic diffusion theory has been used by Zeiri et al. [51] to describe the desorption of K and Xe from a W(111) surface and the molecular desorption of CO from a Ni(110) surface. The values of the parameters appearing in eqs. (2.88) and (2.90) were specified on the basis of independent experimental results. The temperature dependence of the rate was in excellent agreement with experimental observation [123–126] for the three adsorbate–metal systems studied. The pre-exponential factor for adsorbed CO was found to be a factor of 100 larger than the value of 10^{13} s^{-1} for adsorbed K or Xe. This difference was attributed to the frustrated surface rotational modes of chemisorbed CO.

5.2. *Quantum mechanical models*

The earliest quantum models, developed by Lennard-Jones, Strachan, and Devonshire [127–131], treated the one-dimensional motion of an adsorbate bonded to a single surface

atom. The motion of the adsorbate was only considered in the direction perpendicular to the surface, and only single-phonon exchanges between the substrate and adsorbate were taken into account. As a consequence of the one-dimensional nature of the adsorbate motion, all exchange of energy between the adsorbate and the substrate leads to motion perpendicular to the surface, with the net result that the transition probabilities from bound to continuum states are overestimated [132].

De et al. [133] have used a one-dimensional, multiphonon model to represent the desorption of K and Xe from a W surface. The phonon spectrum of the substrate was described by a Debye model, and either a harmonic or a Morse potential was used to describe the interactions between the adsorbate and the substrate. Although the rate of desorption predicted by the model was found to be sensitive to the type of potential used in the calculations, both harmonic and Morse potentials resulted in an Arrhenius dependence of the desorption rate. Good agreement between theory and experiment [123] was obtained for the desorption rates of K from a W surface when the interactions between the adsorbate and the surface were described by a Morse potential. On the other hand, for the desorption of Xe from a W surface, the predicted rates of desorption, using either a harmonic or a Morse potential, were smaller by a factor of 100 than the rates determined experimentally [125]. No explanation for this discrepancy was given by the authors.

Hood et al. [55] have used a one-dimensional quantum model with a Morse potential to analyze the desorption of Ar from a W surface. Included in the model were multiphonon exchange processes between the Ar atoms and the substrate. The rates of desorption predicted by the model exhibited weakly non-Arrhenius behavior. The apparent pre-exponential factor increased from 10^{10} to 10^{11} s^{-1} with increasing temperature, and the apparent activation energy increased from 1.3 to 1.5 kcal/mol. These authors noted that the apparent activation energy was 25%–35% lower than the binding energy of 1.9 kcal/mol used in the Morse potential. This was ascribed to the high desorption probability of adsorbates promoted to bound states of intermediate energy. As a consequence, the apparent desorption activation energy barrier is the energy necessary to reach intermediate bound states rather than that required to reach the top of the potential well.

Hood et al. [55] have also examined the desorption kinetics of CO from a Cu surface using the model discussed above. The CO molecule was treated as a quasi-atom, i.e., no account was made for the CO bending and stretching modes of vibration. The calculated rates of desorption were observed to exhibit strongly non-Arrhenius behavior as a function of temperature and to vary over approximately one order of magnitude depending on the mode of phonon relaxation used in the calculations. The apparent pre-exponential factor for desorption ranged from 10^{13} to 10^{17} s^{-1}, with the smaller values being observed at lower temperatures. The activation energies for desorption were found to be 5%–20% smaller than the binding energy value of 16.6 kcal/mol used in the Morse potential. This observation was explained in the same manner as that for the case of Ar desorption from W, discussed above.

5.3. Simulation of TPD spectra

Both continuum lattice-gas models and Monte Carlo models have been used to simulate TPD spectra of adsorbates from well-defined surfaces. In the continuum approach, both the explicit coverage dependence of the desorption rate and the dependence of the rate coefficient, $k_d^{(\alpha)}$, are described in terms of the average coverage, θ. By contrast, Monte Carlo models of desorption represent the desorption process in terms of a probability which is specific to each site and its configuration of nearest neighbors. As will be shown below, the influence of finite

rates of surface diffusion and the presence of coadsorbates can be incorporated into either type of model.

5.3.1. Simulations based on continuum models

To simulate TPD spectra within the continuum framework, a balance is written between the rate of desorption and the rate at which the surface coverage decreases. Thus,

$$r_d = -\beta \, d\theta/dT, \tag{5.1}$$

where $\beta = dT/dt$ is the rate at which the surface is heated. If lateral interactions between adsorbates can be neglected,

$$r_d = \nu_d^{(\alpha)} \exp(-E_d/k_b T)\theta^{\alpha}.$$

Integration of eq. (5.1) then yields $\theta(T)$, from which it is possible to determine r_d as a function of T, for an initial adsorbate coverage, θ_0.

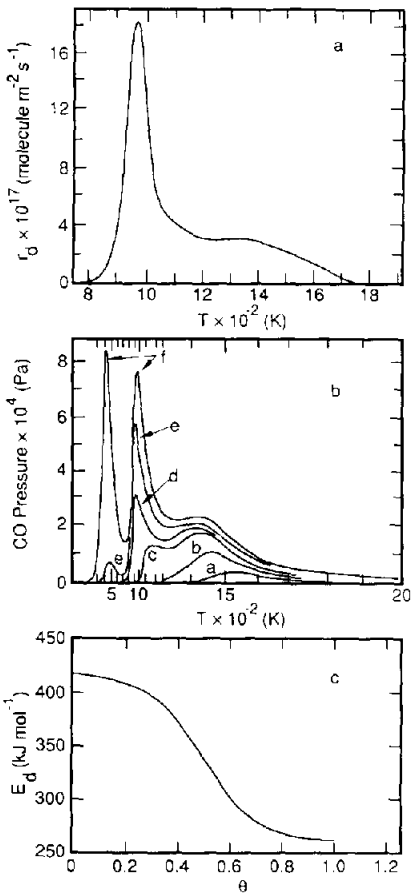

Fig. 30. (a) Predicted CO TPD spectra from a W ribbon [134]. (b) Experimental CO TPD spectra from a W ribbon [135]. The CO exposures (Pa·s) are: (a) 1.9×10^{-5}; (b) 6.0×10^{-5}; (c) 1.6×10^{-4}; (d) 1.9×10^{-4}; (e) 2.5×10^{-4}; and (f) 3.1×10^{-3}. (c) Predicted activation energy profile versus coverage [134].

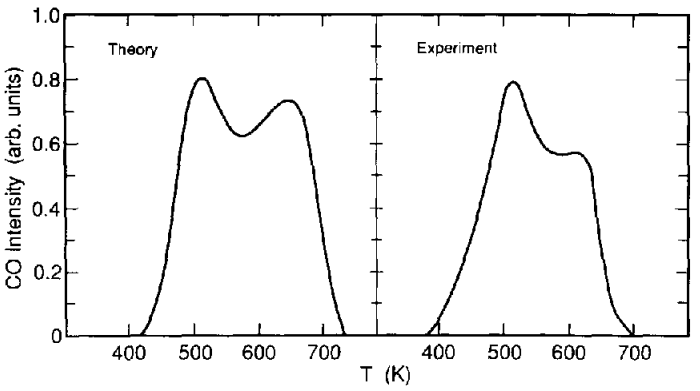

Fig. 31. Predicted [136] and experimental [137] CO TPD spectra from Ir(110) for $\theta_{CO}^{0} = 0.82$.

Experience has shown that the assumption of coverage-independent rate parameters does not adequately represent the full shape of TPD spectra observed experimentally. Substantially better agreement between theory and experiment can be achieved using a lattice-gas model of adsorbate–adsorbate interactions. Several examples of the use of lattice-gas models to simulate TPD spectra are presented below. In all but one case, the distribution of adsorbates on the surface is based on the quasi-chemical approximation (QCA).

Goymour and King [134] have simulated the associative desorption of the high-temperature states of dissociated CO from a tungsten ribbon. The adsorbed C and O atoms were assumed to have equivalent binding energies and the activation energy for associative desorption was set equal to the differential heat of adsorption. The values of the pre-exponential factor ($\nu_d^{(2)} = 3 \times 10^{14}$ s^{-1}), the activation energy at low coverage ($E_d^0 = 100$ kcal/mol), and the nearest-neighbor interaction energies ($w_{CO} = w_{OO} = w_{CC} = 4.8$ kcal/mol) were determined by fitting the TPD spectrum predicted by the model to the experimentally observed TPD spectrum. As illustrated in figs. 30a and 30b, the predicted CO TPD spectrum agrees with that observed experimentally [135]. The coverage dependence of the activation energy for CO desorption was also determined from the model and, as seen in fig. 30c, decreases with increasing CO coverage as a consequence of the repulsive C–O, O–O, and C–C interactions.

Zhdanov [136] has also evaluated the applicability of a lattice-gas model for describing desorption from well-defined metal surfaces. Fig. 31 shows a comparison of the theoretical and experimental [137] TPD spectra for CO desorption from Ir(110). The shape and location of the predicted spectrum is in fair agreement with the experimental results. To obtain this level of agreement, the following parameters were used: $E_d^0 = 33$ kcal/mol, $w_{CO-CO} = 2.2$ kcal/mol, and $\nu_d^{(1)} = 10^{11}$ s^{-1}. It should be noted that the value of $\nu_d^{(1)}$ used to fit the data is considerably smaller than values reported in the experimental literature, which range from 10^{14}–10^{16} s^{-1}.

A second example from the work of Zhdanov [136] is shown in fig. 32. In this instance, the TPD spectra are for the associative desorption of O_2 from an Ir(110) surface. The parameters $E_d^0 = 67$ kcal/mol, $w_{OO} = 3.6$ kcal/mol, and $\nu_d^{(2)} = 3.5 \times 10^{11}$ s^{-1} (3.5×10^{-4} cm^2/s) were used to represent the data, and reasonable agreement between the theoretical and experimental [138] results is observed. The activation energy for O_2 desorption determined from the model was seen to decrease as a function of increasing coverage as a consequence of the repulsive O–O interactions.

While most applications of lattice-gas models have been restricted to a rigid lattice of adsorption sites, Zhdanov [31] has demonstrated the extension of this model to cases where

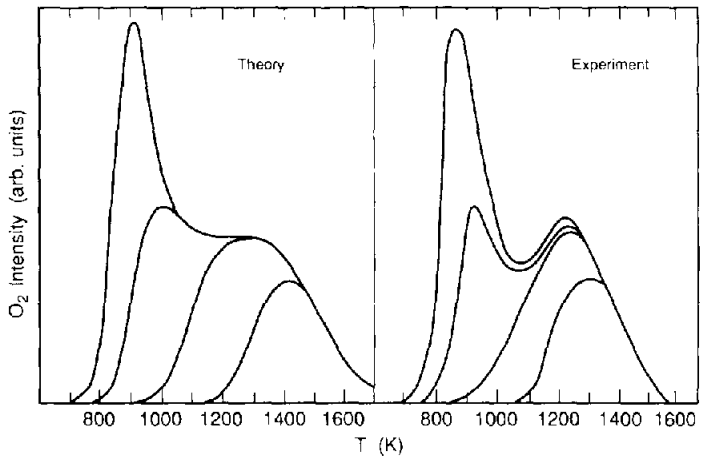

Fig. 32. Predicted [136] and experimental [138] O_2 TPD spectra from Ir(110). Curves in both panels correspond to oxygen coverages of 1.0, 0.75, 0.50, and 0.25.

surface reconstruction occurs. The rate of desorption was written in terms of a chemical potential which included contributions from adsorbate–adsorbate interactions, adsorbate–surface interactions, and the surface-free energy. Illustrations of the variations of $\Delta E_d(\theta)$ and $\nu_d^{(1)}(\theta)/\nu_d^{(1)}(0)$ determined from the model are shown in fig. 33. Both the pre-exponential factor and the activation energy are seen to decrease with increasing coverage. The variation in the apparent pre-exponential factor over 8 orders of magnitude is in accord with what has been determined for the associative desorption of H_2 from a W(110) surface [139]. More recently, Myshlyavtsev and Zhdanov [140] have re-examined the role of surface reconstruction with a more accurate approach. In this study, the variation of the pre-exponential factor with coverage was much smaller, spanning only two orders of magnitude.

Implicit in the QCA is the assumption that surface diffusion is much more rapid than desorption so that an equilibrium configuration of adsorbates is maintained at all times.

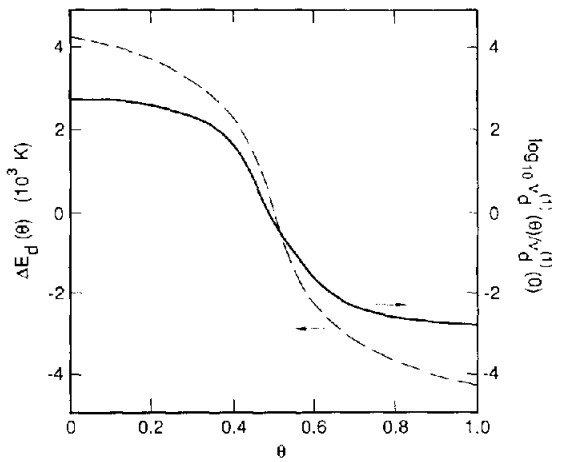

Fig. 33. Variation in $\Delta E_d(\theta)$ and $\nu_d^{(1)}(\theta)/\nu_d^{(1)}(0)$ versus coverage when surface reconstruction occurs [31].

Sundaresan and Kaza [141] have investigated the effects of limited adspecies mobility on the rates of desorption when two species are coadsorbed on a surface. A lattice-gas model was used to describe the effects of lateral interactions. To account for the mobility of the adsorbate, a set of three differential equations was used to describe the change in the occupation probabilities of pairs of sites with time. It was demonstrated that the TPD spectra for coadsorbed species are sensitive to the sequence in which the adsorbates are dosed on the surface as well as to the relative coverages and mobilities of the two species, but no direct comparison was made between theory and experiment.

5.3.2. Simulations based on Monte Carlo models

In the Monte Carlo approach for simulating TPD spectra, adsorbates are assumed to occupy well-defined sites on a fixed lattice. The occupancy of a given site can change as a consequence of either desorption or hopping (diffusion) of the adsorbate to an adjacent site. The probability of desorption from site i is defined by P_i and the probability for diffusion from site i to site j is defined by P_{ij}.

The probability of desorption of a given species from site i in the time interval Δt can be defined as

$$P_i = \nu_{\mathrm{d},i} \exp(-E_{\mathrm{d},i}/k_{\mathrm{b}}T)\Delta t, \tag{5.2}$$

where $\nu_{\mathrm{d},i}$ and $E_{\mathrm{d},i}$ are the pre-exponential factor and the activation energy for the local environment i, respectively. The value of Δt in eq. (5.2) is chosen so that P_i goes to unity at a temperature sufficiently high to guarantee virtually complete desorption from all sites of type i.

The rate of desorption, r_{d}, expressed as a turnover frequency based on the number of surface atoms, N_{s}, is given by

$$r_{\mathrm{d}} = N_{\mathrm{d}}/(\alpha\, N_{\mathrm{s}}\, \Delta t), \tag{5.3}$$

where N_{d} is the number of adsorbate atoms or molecules desorbing in the time interval Δt. The parameter α is 1 for atomic or molecular desorption and 2 for associative desorption. Consequently, r_{d} is the rate of desorption as observed from the gas phase.

The diffusion of adsorbates can be handled using the Monte Carlo techniques described in section 4.4. If the rate of diffusion is of comparable magnitude to the rate of desorption, then the dynamics of diffusion are represented with an energy barrier model and P_{ij} is given by

$$P_{ij} = \exp(-E_{\mathrm{diff}}/k_{\mathrm{b}}T). \tag{5.4}$$

If diffusion occurs very rapidly relative to desorption, the spatial distribution of adsorbates on the surface will remain very close to equilibrium. Under such circumstances, the probability of moving an adsorbate can be represented by Kawasaki dynamics:

$$P_{ij} = \frac{\exp\left[-(Q_i - Q_j)/k_{\mathrm{b}}T\right]}{1 + \exp\left[-(Q_i - Q_j)/k_{\mathrm{b}}T\right]}, \tag{5.5}$$

where Q_i and Q_j are the heats of adsorption for an adsorbate at sites i and j, respectively. Application of eq. (5.5) for a large number of hops leads to an equilibrium distribution of adsorbates on the surface.

The probability and rate formulations described above are incorporated into a Monte Carlo algorithm for simulating the temperature-programmed desorption of adsorbates. The algorithm presented below is for simulations in which adsorbate diffusion is described by Kawasaki dynamics, the case most frequently treated in the literature.

The surface is represented by an array of numbered sites, and periodic boundary conditions are used to eliminate edge effects. Adsorbate atoms or molecules are placed on the surface lattice to achieve a desired initial coverage, θ_0. The temperature is initialized at T_0 and taken to be constant at this value for the time interval Δt. During this time interval, the desorption of adsorbates from occupied sites is determined by the outcome of a comparison between a random number, R, and the probability condition for desorption P_i. When $R \leq P_i$, the adsorbate (or pair of adsorbates for associative desorption) is removed from the lattice, and N_d is incremented by one (two for associative desorption). If, on the other hand, $R > P_i$, the adsorbate remains on the lattice. After sampling of the surface is completed, the rate of desorption for this time interval is calculated from eq. (5.3).

Following the calculation of the rate of desorption, the remaining adsorbates are redistributed on the lattice to account for the effects of surface diffusion. Redistribution of the adsorbates to achieve a new equilibrium configuration is achieved as follows. Movement of an adsorbate at site i to a vacant site j is determined by comparing a random number R with the value of P_{ij} given by eq. (5.5). If $R \leq P_{ij}$, the adsorbate is moved from site i to site j, whereas if $R > P_{ij}$, the adsorbate is not moved. Application of this test to the ensemble of adsorbates for a sufficiently large number of hops leads to a minimization of the surface energy and a re-establishment of equilibrium.

The desorption/diffusion calculations described above constitute a Monte Carlo step (MCS). As noted above, the time interval associated with an MCS is Δt, and over this interval the temperature is constant. At the end of an MCS, the temperature is increased by the increment $\beta \Delta t$, where β is the heating rate. A new MCS is then carried out at the next temperature. This process is repeated until a temperature is reached for which the surface is depleted of adsorbate. A plot of the desorption rate as a function of temperature then yields a TPD spectrum. Several examples of the simulation of TPD spectra using Monte Carlo methods are presented below.

In the absence of lateral interactions, Lombardo and Bell [142] have demonstrated that the

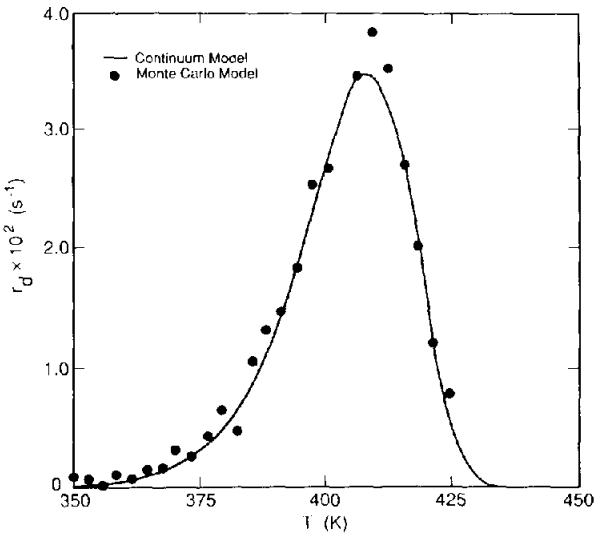

Fig. 34. Comparison of Monte Carlo and continuum models for the simulation of non-associative TPD spectra in the absence of lateral interactions [142].

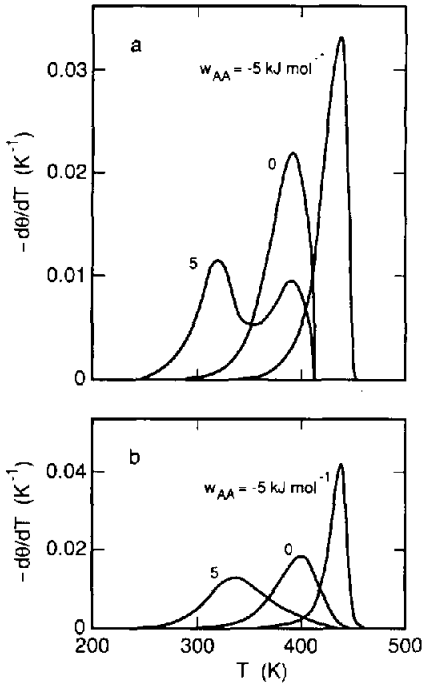

Fig. 35. (a) Monte Carlo simulation of TPD spectra [143]. (b) Continuum simulation of TPD spectra [144]. Lateral interactions between adsorbates in the continuum simulations are described with the Braggs–Williams approximation.

continuum and stochastic representations of TPD lead to identical spectra. An illustration of this point for non-associative desorption is given in fig. 34. The slight deviations of the Monte Carlo simulations from the curve for the continuum model are attributable to the combined effects of finite lattice size, finite step size, and statistical, random-number fluctuations.

Sales and Zgrablich [143] have utilized a Monte Carlo approach to model the influence of lateral interactions between adsorbates on TPD spectra. Pairwise-additive interactions were used to account for the lateral interactions between adsorbates. Fig. 35a shows the simulated TPD spectra for non-associative desorption from a one-dimensional surface for selected values of the interaction parameter w_{AA}. The predicted TPD spectra based on a continuum lattice-gas model using the Bragg–Williams approximation ($E_d = E_d^0 - zw_{AA}\theta$, where z is the number of nearest-neighbor sites around a given site) [144] are presented in fig. 35b. A comparison of the two figures demonstrates that, for $w_{AA} = 0$ (no interactions) and for $w_{AA} < 0$ (attractive interactions), the TPD spectra determined by the Monte Carlo and continuum lattice-gas models are in good agreement. For $w_{AA} > 0$ (repulsive interactions), however, the Monte Carlo model predicts two peaks whereas the continuum lattice-gas model predicts one. The authors indicate that the difference between the two models arises from the incorrect assumption of a random distribution of adsorbates in the Bragg–Williams approximation. The influence of the number and distribution of surface binding sites with different energies on TPD spectra was also examined by Monte Carlo simulations, and it was shown that the shape and location of simulated TPD spectra are sensitive to the distribution of adsorbates on the surface as well as to the magnitude and sign of the energetic interactions between species.

In another study, Sales et al. [145] have compared the desorption kinetics predicted from a Monte Carlo model using pairwise-additive energetics for nearest- and next-nearest neighbor

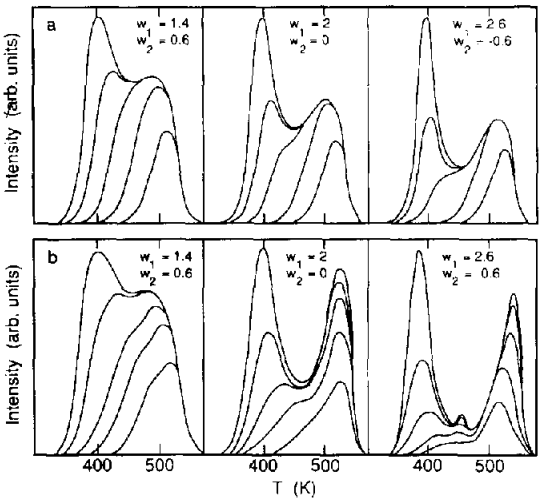

Fig. 36. Simulation [145] of TPD spectra for both nearest-neighbor interactions w_1 and next-nearest neighbor interactions w_2: (a) continuum model; (b) Monte Carlo model. The lateral interactions are in kcal/mol.

interactions with the desorption kinetics predicted from a continuum lattice-gas model using the quasi-chemical approximation for nearest-neighbor interactions and the Bragg–Williams approximation for next-nearest neighbor interactions. As seen in fig. 36, the two models predict many of the same features for selected values of the lateral interaction parameters. The number of peaks, the peak locations, and the coverage dependence of the peak positions predicted by the two models, however, are different. The differences in the spectra predicted from the two models are especially pronounced for the simulations incorporating repulsive nearest-neighbor interactions with attractive next-nearest neighbor interactions.

Hood et al. [74] have combined Monte Carlo simulations and continuum rate expressions to describe molecular desorption of N_2 from a Ru(001) surface. The Monte Carlo segment of the algorithm was used to determine the local environment of each adsorbate and hence the local activation energy for desorption. The coverage and activation energy for each type of surface environment were then used in a continuum rate expression such as eq. (5.1) to solve for the rate of desorption. The parameters used to simulate the TPD spectra were repulsive nearest-neighbor interactions of 0.25 kcal/mol, attractive next-nearest neighbor interactions of 0.45 kcal/mol, and a pre-exponential factor of 10^{12} s^{-1}. In addition, the pre-exponential factor was postulated to have an increasing exponential dependence with increasing global surface coverage of N_2. As illustrated by figs. 37a and 37b, the simulated TPD spectra agree with experimental observation [75,76]. The low-coverage peak was attributed to desorption of N_2 molecules located at the perimeter of N_2 islands in which the molecules were arranged in $(\sqrt{3} \times \sqrt{3})R30°$ domains, whereas the high-coverage peak was attributed to desorption of N_2 from antiphase $(\sqrt{3} \times \sqrt{3})R30°$ domains located within the N_2 islands.

Lombardo and Bell [142] have developed a Monte Carlo algorithm in which the BOC-MP method [19,20] was used to calculate the activation energy for desorption. For non-associative desorption, E_d is given by

$$E_d = Q^*_{A,n}, \tag{5.6}$$

and for associative desorption of A_2, E_d is given by

$$E_d = Q^*_{A,n} Q^*_{A',n} / (Q^*_{A,n} + Q^*_{A',n}), \tag{5.7}$$

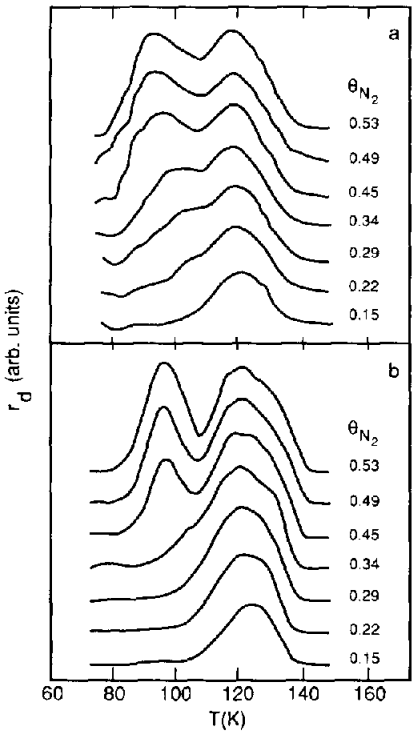

Fig. 37. Experimental (a) [75,76] and simulated (b) [74] TPD spectra of molecular N_2 from Ru(001).

where $Q^*_{A,n}$ and $Q^*_{A',n}$ represent the heats of adsorption of A and A′, respectively. (Eq. (5.7) represents a simplified version of eq. (2.14).) The two recombining atoms are designated A and A′ to denote that the local environments of each may be different. In order to account for coverage effects, $Q^*_{A,n}$ and $Q^*_{A',n}$ are determined from eq. (2.9).

When metal–adsorbate and adsorbate–adsorbate interactions between adsorbates were included, Lombardo and Bell [142] observed multiple peaks in the simulated TPD spectra, and the activation energy profile of the desorbing species was found to decrease in a non-linear fashion with increasing coverage. It was also shown that the activation energy of the desorbing species is less than or equal to the average value for the entire adlayer. Physically, this means that for a given coverage, adsorbates which are in less stable configurations have a lower activation energy for desorption and hence desorb preferentially.

In the same study, Lombardo and Bell [142] reported simulations of the associative desorption of H_2 from Mo(100). As illustrated by figs. 38a and 38b, the simulated TPD spectra for H_2 desorption from a Mo(100) surface agree with the experimentally observed spectra [146]. Figs. 39a and 39b show a comparison of the simulated and experimentally observed [147] profiles of the activation energy as a function of coverage. Both plots exhibit a step-wise decrease in activation energy as the coverage increases. The observed decrease in the activation energy with increasing coverage is caused by a decrease in the heat of adsorption of H atoms when more than one atom is bonded to a given metal atom.

Monte Carlo models have also been used to simulate the desorption of coadsorbed species. Gupta and Hirtzel [148] have investigated the effects of lateral interactions on the non-associative desorption of coadsorbed species A and B. Both nearest- and next-nearest neighbor

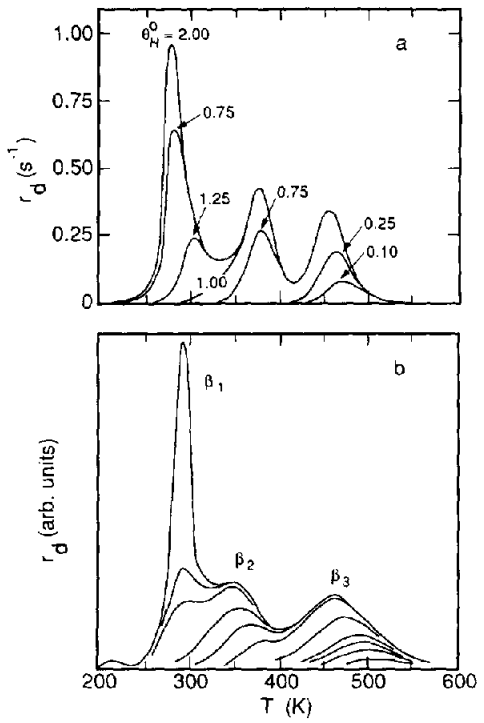

Fig. 38. Simulated (a) [142] and experimental (b) [146] TPD spectra of H_2 from Mo(100).

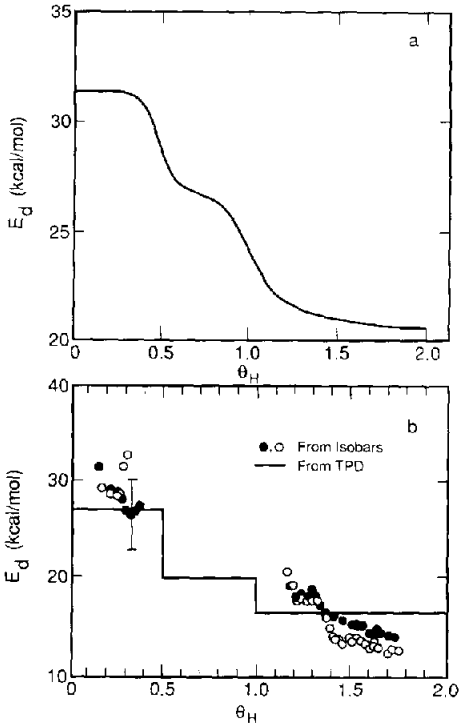

Fig. 39. Simulated (a) [142] and experimental (b) [147] variation in E_d with θ_H for H_2 desorption from Mo(100).

interactions between species were represented in a pairwise-additive fashion. It was shown that the number of peaks in the TPD spectrum and the spectrum shape and location are sensitive to the lateral interactions and to the relative coverage of each species. These authors also demonstrated that A–B interactions only affect the spectrum of the species desorbing at lower temperatures whereas A–A and B–B interactions only affect the spectra of the respective A and B species.

More recently, Lombardo and Bell [149] have simulated TPD spectra for coadsorbed species using the BOC-MP approach to describe the effects of adsorbate coverage on the energetics of desorption. Nearest-neighbor interactions between the adsorbates and the metal surface as well as nearest-neighbor interactions between the coadsorbates were taken into account. The presence of a strongly bound coadsorbate on a bcc(100) surface was shown to shift the associative desorption spectrum of adsorbed atoms to lower temperatures. The simulated TPD spectra were found to be in qualitative agreement with experimental results for H_2 coadsorbed with strongly bound atomic species such as C, O, or N on Mo(100) [150] and Fe(100) [151] surfaces.

In the same paper, Lombardo and Bell [149] describe simulation of TPD spectra for the concurrent desorption of B molecules and the associative desorption of A atoms from an fcc(100) surface [149]. Two types of behavior were observed: in one case, both species exhibited new low-temperature features not present in the TPD spectra of A and B when each species was adsorbed alone. In the second case, only the more weakly bound species displayed new spectral features. These types of behavior are in qualitative agreement with what has been

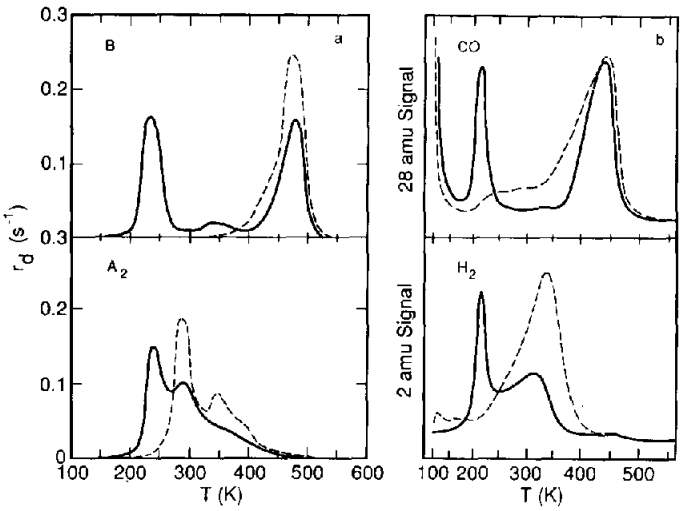

Fig. 40. (a) Simulated TPD spectra of B and A_2 [149]. (b) Experimental TPD spectra of CO and H_2 [152]. The dashed curves correspond to desorption of each species adsorbed separately, and the solid curves correspond to desorption of both species coadsorbed.

observed for the codesorption of CO and H_2 from Ni(100) [152] and Rh(100) [153] surfaces, respectively. Fig. 40a shows TPD spectra for A_2 and B when each species is adsorbed separately, and when both species are coadsorbed. The experimentally observed TPD spectra for CO and H_2 on a Ni(100) are shown in fig. 40b [152]. A comparison of the two figures demonstrates the qualitative agreement between the model predictions and the experimental observations. In fig. 41 are shown the activation energy profiles versus coverage for both the pure component and codesorption simulations. For the A_2 and B activation energy profiles when both species are coadsorbed, the activation energy profiles are lower than for the respective pure component activation energies and show larger variation with coverage.

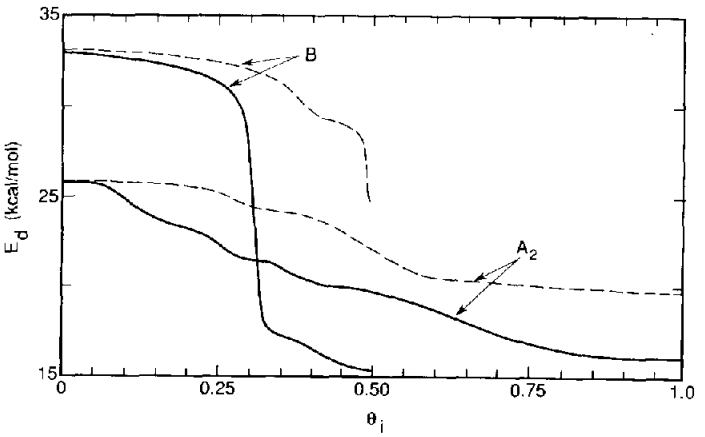

Fig. 41. Variation in E_d with θ_i for the simulations in fig. 40a [149]. The dashed curves correspond to desorption of each species adsorbed separately, and the solid curves correspond to desorption of both species coadsorbed.

5.4. Compensation effect

Analysis of experimental TPD spectra using empirical rate expressions of the form

$$r_d = \nu_d^{(\alpha)}(\theta)\,\exp\left[-E_d(\theta)/k_b T\right]\theta^{\alpha} \tag{5.8}$$

have shown evidence of a compensation effect, namely that $\nu_d^{(\alpha)}(\theta)$ and $E_d(\theta)$ vary in the same manner for changes in coverage and temperature [154–159]. In particular, it has often been observed that both $\nu_d^{(\alpha)}(\theta)$ and $E_d(\theta)$ decrease with increasing adsorbate coverage. While the decrease in $E_d(\theta)$ is readily attributable to repulsive lateral interactions, the large decreases in $\nu_d^{(\alpha)}(\theta)$ (e.g., up to nine orders in magnitude) have not been explained satisfactorily. Seebauer et al. [156] have recently reviewed different theoretical representations for the pre-exponential factor. Although several of the theories predict compensation behavior, none are able to account for the large variations such as those determined from the analysis of experimental data. Seebauer et al. suggested, however, that models which account for the phonon vibrational modes of the solid and for surface reconstruction may be able to account for the large variations observed in the pre-exponential factor as a function of coverage.

The apparent inconsistency between the large variations in $\nu_d^{(\alpha)}(\theta)$ deduced from experimental data and the significantly smaller variations suggested by various physical models can be reconciled in the following manner. To begin with, it must be recognized that eq. (5.8) is written intuitively as a generalization of eqs. (2.26) and (2.27) rather than on the basis of a physical theory of desorption. For example, reference to eqs. (2.50)–(2.53) shows that the rate of desorption cannot be factored naturally into a pre-exponential factor, an exponential factor, and a factor describing the coverage dependence. This indicates that eq. (5.8) is not a valid physical representation of the kinetics of desorption. As a consequence, while eq. (5.8) can be fitted to experimental desorption data, the values of $\nu_d^{(\alpha)}(\theta)$ and $E_d(\theta)$ determined by this means must be regarded as apparent values. Consistent with this interpretation, fig. 5 shows that the apparent pre-exponential factor deduced from a lattice-gas model in the quasi-chemical approximation exhibits a strong dependence on θ, even though the pre-exponential factor incorporated into the model is, in fact, assumed to be constant. Inspection of eqs. (2.50)–(2.53) reveals further that the observed coverage dependence of the apparent pre-exponential factor can be ascribed to $f_d'(\theta, w_{AA})$ and $f_d''(\theta, w_{AA})$ which are each comprised of weighted terms of the probabilities of finding an adsorbate in a specific configuration of nearest neighbors. Viewed in this fashion, the large variations in the apparent pre-exponential factor can be attributed to the configurational and energetic effects of nearest-neighbor interactions, rather than to an explicit dependence of the pre-exponential factor on coverage.

6. Reactions

6.1. Theoretical prediction of k_r

With the exception of absolute rate theory, none of the theoretical approaches described in section 2 have been used to predict rate coefficients for reactions occurring on metal surfaces. Estimates from absolute rate theory of the pre-exponential factor ν_r for Langmuir–Hinshelwood reactions range from 10^{-4}–10^{4} cm^2 s^{-1} [47]. This approach suffers, however, from the need to make a number of ad-hoc assumptions regarding the structure and molecular properties of the transition state. Estimates of the activation energy for surface reactions can be made using the BOC-MP approach. Shustorovich [21] has shown that where comparison can be made with

Table 8
Activation energy barriers (kcal/mol) for selected surface reactions determined from the BOC-MP method [21]

Reaction	Surface	Activation calc.	Energy exp.	Ref.
$CO_{2,g} \rightarrow CO_s + O_s$	Rh(111)	17	17	[160]
	Re(001)	−5	≤ 0	[161]
$CO_s + O_s \rightarrow CO_{2,g}$	Rh(111)	24	27	[162]
	Pd(111)	24	25	[2]
	Pt(111)	23	25	[2]
	Ag(110)	6.0	5.3	[163]
$NO_s + N_s \rightarrow N_2O_s$	Rh(111)	22	21	[164]
	Rh(100)	21	21	[165]
	Pt(111)	22	20	[166]
$N_2O_s \rightarrow N_{2,s} + O_s$	Rh(111)	−63	–	–
	Pt(111)	−46	–	–

experiment, the BOC-MP method provides good estimates of E_r. This conclusion is illustrated by the examples presented in table 8.

6.2. Simulation of TPSR spectra and steady-state dynamics

Numerous authors have reported theoretical descriptions of reactions occurring on well-defined metal surfaces and compared the results of such simulations with experiment. Two types of reaction studies have been considered. The first involves coadsorption of both reactants followed by a progressive heating of the surface to raise the temperature. The rates at which the reactants and products desorb from the surface are then followed as a function of time or temperature. In the second type of experiment, reactants are passed over a surface maintained at a constant temperature, and the steady-state rates of product formation are observed. Simulations of both types of experiments have been carried out using continuum models.

Bridge and Lambert [167] have used a lattice-gas model with the QCA to treat the associative recombination of N_s and O_s produced by dissociative adsorption of NO on Pt, Ni, and Ru surfaces. The associative desorption kinetics were simulated for two cases of interactions between the atomic adsorbates. In the first case, repulsive interactions between all atomic species (N–N, O–O, and N–O) were taken into account. In the second case, only repulsive N–N interactions were considered. For both cases, N_2 desorbed at low temperature, O_2 desorbed at high temperature, and no appreciable NO was formed. This selectivity to N_2 and O_2 products was explained as follows. At low temperatures, formation of N_2 is energetically favored, and atomic nitrogen is depleted from the surface. At intermediate temperatures for which the formation of NO is energetically favorable, the amount of nitrogen remaining on the surface is too small to form appreciable NO. At still higher temperatures, atomic oxygen is the only species remaining on the surface and it desorbs as O_2. The negligible selectivity to NO product formation is thus seen to result from the lack of atomic nitrogen on the surface at temperatures favorable for NO formation. Comparison of the simulated TPD spectra with those observed experimentally [166,168,169] led to the conclusion that O–O repulsions are significant for all three metals. In contrast, the N–N interactions were found to be either zero or slightly attractive on Pt and Ni, but definitely repulsive on Ru.

The oxidation of CO to CO_2 on an Ir(110) surface has been simulated by Zhdanov [136] with a lattice-gas/QCA model. Since the oxidation of CO is accompanied by CO desorption, both elementary processes were included in the model. The values of $\nu_{d,CO}^{(1)} = 10^{11}$ s^{-1}, $E_{d,CO}^{0} = 33$

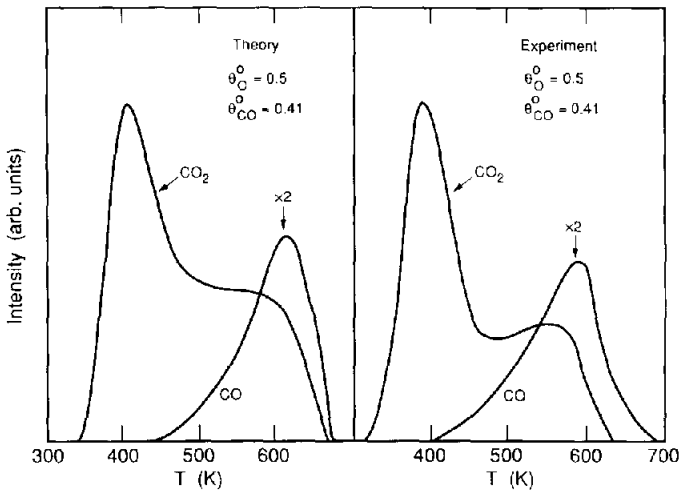

Fig. 42. Theoretical [136] and experimental [170] TPSR spectra for CO oxidation and CO desorption on Ir(110).

kcal/mol, and $w_{CO-CO} = 2.2$ kcal/mol used in these simulations were chosen to obtain a successful representation of the TPD spectrum of CO in the absence of adsorbed oxygen. Likewise, the values of $\nu_{d,O_2}^{(2)} = 3.5 \times 10^{-4}\,\text{cm}^2\,\text{s}^{-1}$, $E_{d,O_2}^0 = 67$ kcal/mol, and $w_{OO} = 3.6$ kcal/mol were chosen to obtain a good representation of the TPD spectrum of O_2 in the absence of adsorbed CO. The remaining parameters, $\nu_r = 10^{13}\ \text{s}^{-1}$, $E_r^0 = 37$ kcal/mol, and $w_{CO-O} = 1.7$ kcal/mol, were chosen by trial and error to obtain the best representation of the TPSR spectra. A comparison between theory and experiment [170] is shown in fig. 42. It is seen that most features of the experimentally observed TPSR spectra are reproduced in the simulation.

As an additional part of his study, Zhdanov [136] determined the apparent activation energies for CO desorption and oxidation using the following relationships

$$E_{d,CO} = -k_b T \ln\left(k_{d,CO}^{(1)}/\nu_{d,CO}^{(1)}\right), \tag{6.1}$$

$$E_r = -k_b T \ln\left(k_r/\nu_r 2\theta_{CO}\theta_O\right). \tag{6.2}$$

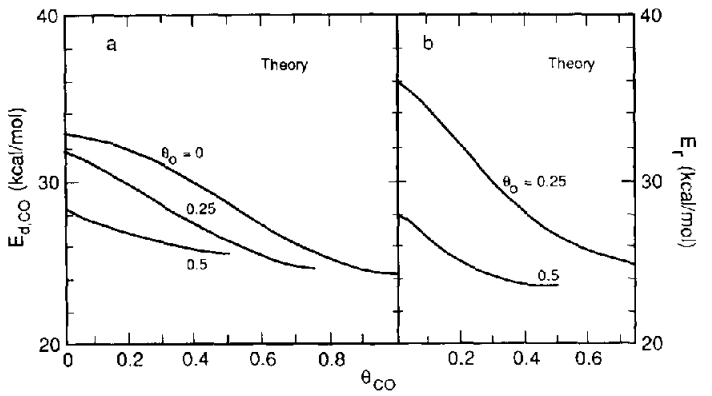

Fig. 43. (a) Predicted variation of E_d versus θ for CO desorption from Ir(110) [136]. (b) Predicted variation of E_r versus θ for CO oxidation [136].

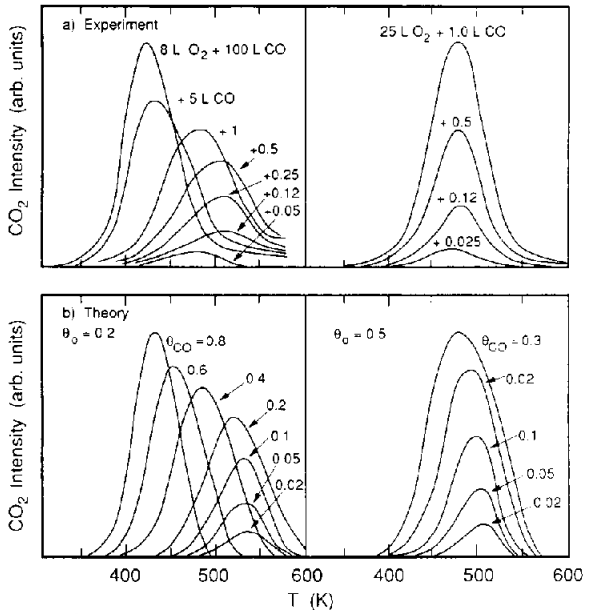

Fig. 44. TPSR spectra for CO oxidation on Ir(111): (a) experimental spectra as a function of gas exposure [173]; (b) theoretical spectra as a function of coverage [171].

Fig. 43 shows that both $E_{d,CO}$ and E_r decrease with increasing θ_{CO} and θ_O as a consequence of the repulsive CO–CO, CO–O and O–O interactions.

Zhdanov has also simulated the oxidation of CO over Ir(111) under both TPSR [171] and steady-state conditions [172]. The parameters used to represent the TPSR spectra were $\nu_r = 10^{13}$ s^{-1}, $E_r^0 = 31$ kcal/mol, and $w_{CO-CO} = 0.7$ kcal/mol, $w_{OO} = 0.8$ kcal/mol, and $w_{CO-O} = 0.5$ kcal/mol. The experimental TPSR spectra [173] are shown in fig. 44a and the corresponding simulations of these spectra are presented in fig. 44b. Comparison of these figures indicates that the TPSR spectra determined from the lattice-gas model are in semi-quantitative agreement with those observed experimentally. Of particular interest is the fact that the lattice-gas model correctly predicts the strong upscale shift in the position of the CO_2 peak with increasing initial oxygen coverage. This trend cannot be represented successfully if lateral interactions are neglected.

The steady-state oxidation of CO over Ir(111) was described by Zhdanov [172] in terms of the following mechanism:

$$CO_g \rightleftarrows CO_s,$$

$$O_{2,g} \rightarrow 2\ O_s,$$

$$CO_s + O_s \rightarrow CO_g.$$

At steady state, the kinetics of the reaction are given by

$$S_{CO}^{(1)}(\theta) F_{CO} = r_{d,CO} + r_r, \tag{6.3}$$

$$2S_{O_2}^{(2)}(\theta) F_{O_2} = r_r, \tag{6.4}$$

where $S_i^{(\alpha)}(\theta)$ and F_i are the sticking coefficient and the flux of component i, respectively. The rate parameters appearing in the expressions for $r_{d,CO}$ and r_r are identical to those used for

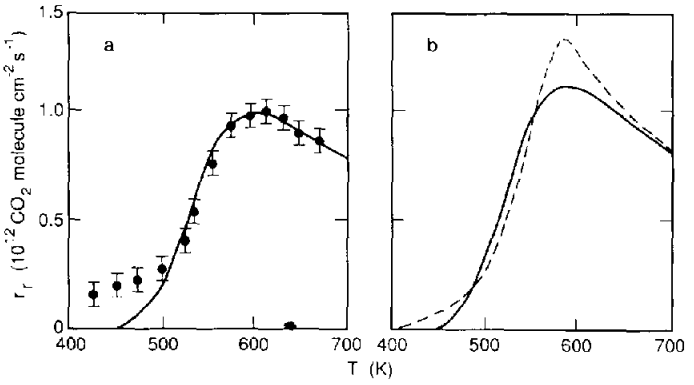

Fig. 45. Steady-state rate of CO oxidation versus T on Ir(111). Solid lines are theoretical calculations [172]; circles are experimental data in arbitrary units [173]; and dashed line is experimental data [174]: (a) $P_{CO} = P_O = 1.1 \times 10^{-7}$ Torr; (b) $P_{CO} = 5 \times 10^{-8}$ Torr and $P_O = 1.2 \times 10^{-7}$ Torr.

describing the oxidation of CO during TPSR. The dependence of the CO and O_2 sticking coefficients on coverage was approximated by:

$$S_{CO}^{(1)}(\theta) = S_{CO}^{(1)}(0)(1 - \theta_{CO} - \theta_O), \tag{6.5}$$

$$S_{O_2}^{(2)}(\theta) = S_{O_2}^{(2)}(0) P_{VV}, \tag{6.6}$$

where $S_{CO}^{(1)}(0) = 1.0$, $S_{O_2}^{(2)}(0) = 0.5$, and P_{VV} is the probability that two nearest-neighbor sites are vacant. A plot of the steady-state oxidation rate as a function of temperature and pressure is shown in fig. 45. It is evident that the theoretical model provides a good description of the experimental data [173,174], and in particular, the maximum in the rate at 600 K.

The steady-state oxidation of H_2 over Pt(111) has been analyzed by Zhdanov [175] using an approach similar to that used for the description of CO oxidation over Ir(111). The reaction mechanism is assumed to be:

$$H_{2,g} \rightleftarrows 2\ H_s,$$

$$O_{2,g} \rightarrow 2\ O_s,$$

$$H_s + O_s \rightarrow OH_s,$$

$$OH_s + H_s \rightarrow H_2O.$$

Fig. 46 compares the steady-state reaction rates observed experimentally [176] with those predicted on the basis of the lattice-gas model. The theoretical model provides a qualitatively correct description of the experimental data.

Sundaresan and Kaza [177] have explored the effects of limited adsorbate mobility on the rates of surface reactions. The formulation of the lattice-gas model used for this study was based on that used to treat the effects of adsorbate mobility on non-associative desorption described in section 5.3 [141]. It was demonstrated that limited adsorbate mobilities can significantly alter the rates of surface reactions depending on the lateral interactions and mobilities of the adsorbed species.

An analysis of the steady-state kinetics of the $CO-O_2$ and CO–NO reactions over single-crystal Rh(111) and supported Rh/Al_2O_3 has been reported by Oh et al. [178]. The oxidation

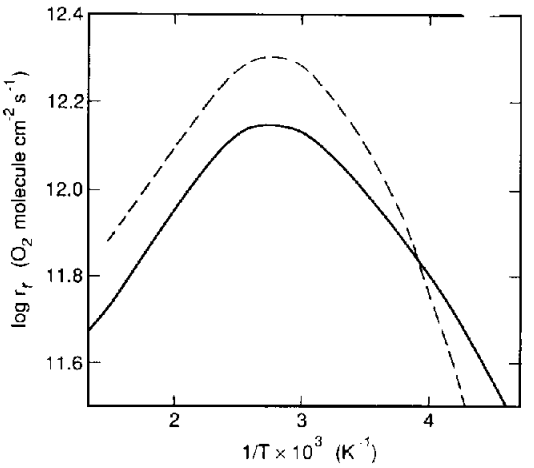

Fig. 46. Steady-state rate of hydrogen oxidation versus T on Pt(111) for $P_H = 1.34 \times 10^{-5}$ Pa and $P_O = 6.7 \times 10^{-6}$ Pa. Solid line is the theoretical calculation [175] and the dashed line is the experimental result [176].

of CO is represented by the mechanism described above. In the limit of high CO coverage, the authors show that the rate of CO_2 formation can be written as

$$r_r = \frac{2k_{a,O_2}}{k_{a,CO}} \frac{P_{O_2}}{P_{CO}} \left\{ \nu_{d,CO}^{(1)} \exp\left[\frac{-\left(E_{d,CO}^0 - \phi_{CO}\theta_{CO}\right)}{k_b T} \right] \right\}. \tag{6.7}$$

In this expression, the activation energy for CO desorption is seen to depend linearly on the coverage of CO. With the values of $E_{d,CO}^0 = 31.6$ kcal/mol, $\phi_{CO} = 4.5$ kcal/mol, and $\nu_{d,CO}^{(1)} = 1.6 \times 10^{14}$ s^{-1}, a quantitative fit of rate data versus $1/T$ could be achieved for both single-crystal and supported Rh catalysts over four orders of magnitude in the rate.

In the same study, Oh et al. [178] modelled the kinetics of the CO–NO reaction for the same Rh catalysts using the following mechanism:

$$\begin{aligned}
&CO_g \rightleftarrows CO_s, \\
&NO_g \rightleftarrows NO_s, \\
&NO_s \rightarrow N_s + O_s, \\
&NO_s + N_s \rightarrow N_{2,g} + O_s, \quad \delta\text{-}N_2, \\
&2\,N_s \rightarrow N_{2,g}, \quad \beta\text{-}N_2, \\
&CO_s + O_s \rightarrow CO_{2,g}.
\end{aligned}$$

The rate of CO desorption was assumed to decrease linearly with both CO and N coverage and the rate of N_2 desorption was assumed to decrease linearly with N coverage. Although an analytical expression for the rate of N_2 formation could not be obtained in this case, a numerical solution of the problem was achieved. Using the parameter values listed in table 9, good agreement was obtained between the measured and predicted rates of NO reduction by CO over a Rh(111) surface. A similar level of agreement was achieved for simulations of NO reduction over Rh/Al_2O_3; however, in this instance a smaller value of the rate coefficient for NO dissociation was required than for Rh(111). The difference in the rate coefficients for

Table 9
Parameters used to represent the CO–NO reaction network [168]

Process	Oh et al.	Literature values	Refs.
CO adsorption			
$S_{CO}^{(1)}(\theta)$	0.5	0.5	[179,180]
CO desorption			
$\nu_d^{(1)}$ (s^{-1})	1.6×10^{14}	$1\times10^{13.6\pm0.3}$	[181]
E_d^0 (kcal/mol)	31.6	31.6 ± 1	[181]
ϕ_{CO} (kcal/mol)	4.5	–	–
ϕ_{NO} (kcal/mol)	10	10	[182]
CO_2 formation			
$\nu_d^{(2)}$ (s^{-1})	1×10^{12}	3×10^{5}	[179]
E_d (kcal/mol)	14.3	14.3	[179]
NO adsorption			
$S_{NO}^{(1)}(\theta)$	0.5	~1	[183]
NO desorption			
$\nu_d^{(1)}$ (s^{-1})	5×10^{13}	2×10^{12}	[164]
E_d (kcal/mol)	26	26	[164]
NO dissociation			
ν_r (s^{-1})	6×10^{13}	6×10^{13}	[184]
E_r (kcal/mol)	19	19	[184]
δ-N_2 formation			
ν_r (s^{-1})	2×10^{9}	2×10^{9}	[164]
E_r (kcal/mol)	21	21	[164]
β-N_2 formation			
$\nu_d^{(2)}$ (s^{-1})	3×10^{10}	3×10^{10}	[164]
E_d^0 (kcal/mol)	31	31	[164]
ϕ_N (kcal/mol)	4	..	–

Rh(111) and Rh/Al_2O_3 was attributed to the structure sensitivity of the NO dissociation process.

6.3. Effects of adsorbate islanding

Lateral interactions between adsorbed species favor their organization into non-random, two-dimensional distributions. Under appropriate conditions, an adsorbate may even form islands of macroscopic dimensions. Such a situation can arise for coadsorbed reactants A and B when $w_{AA} < 0$, $w_{BB} = w_{AB} = 0$, and $T < T_c$, where T_c is the critical temperature of A, below which islands of A form. If the reactant B cannot penetrate the A islands, reaction will only occur at the island boundaries. Consequently, the rate of product formation will depend on the number of A islands, the length and shape of their boundaries, and on related dynamical properties such as the rates of island growth and diffusion of B. These characteristics depend in turn on initial conditions such as initial coverages, order, and time delay between A and B adsorption, and temperature. A well-known system exhibiting the behavior just described is $O_s + CO_s \rightarrow CO_{2,g}$ on various metal surfaces [2,185]. In this case, the oxygen atoms are the aggregating species and CO is the mobile reactant. Both Monte Carlo and continuum models have been used to simulate the effects of island formation on reaction kinetics.

Silverberg et al. [186] have used a Monte Carlo model to examine the consequences of the issues raised in the preceding paragraph. The reaction considered was $A_s + B_s \rightarrow AB_g$ with only attractive interactions between A adsorbates being taken into account. In the initial segment of

the simulation, species A was adsorbed on the surface and then allowed to diffuse in order to either fully or partially reach an equilibrium adsorbate configuration. Species B was subsequently adsorbed randomly on unoccupied surface sites. As a consequence of the attractive interactions between A adsorbates, islands of A form, and the reaction occurs primarily at the ramified perimeters of the A islands. The power law dependence of the reaction on the coverage of A was determined to be 0.60, which is larger than the value of 0.50 assumed for perfectly uniform islands. The rate of reaction was further shown to be sensitive to the initial coverage of reactants and to the time allowed for the A species to form islands.

In a series of related studies, Silverberg and Ben-Shaul [187–190] have applied a combination of Monte Carlo and lattice-gas models to simulate the TPSR of $A_s + B_s \rightarrow AB_g$. Interactions between all species (A–A, A–B, and B–B) were included in the model. As a consequence of attractive A–A interactions, species A formed islands on the surface. The Monte Carlo segment of the algorithm was used to determine the non-equilibrium, non-uniform distribution of A atoms and the rate of AB formation. The lattice-gas models were used to determine the equilibrium distribution of B on surface sites not occupied by A. The shape and location of the simulated TPSR spectra were sensitive to the magnitude and sign of the A–B and B–B interactions as well as to the amount of time allowed for the formation of A islands. It was observed that the two peaks in the AB TPSR spectrum occurred from the reaction of AB species from two types of surface environments. The low-temperature peak corresponds to the reaction of isolated AB pairs whereas the high-temperature peak corresponds to desorption of AB pairs located in the vicinity of other A species.

The effects of lateral interactions and phase separation on the oxidation of SO_2 to SO_3 over Pt have been investigated by Kaza and Sundaresan [191]. The reaction system was analyzed using a lattice-gas model together with the Bragg–Williams approximation. The reaction was postulated to proceed via the following steps:

$$O_2 \rightarrow 2\ O_s,$$

$$O_s + SO_{2,g} \rightleftarrows SO_{3,s},$$

$$SO_{3,s} \rightleftarrows SO_{3,g}.$$

It was observed that the assumption of sufficiently strong attractive interactions between adsorbed SO_3 molecules resulted in a phase separation into a condensed (liquid-like) and a dilute (gas-like) phase. The inclusion of attractive SO_3–SO_3 interactions and SO_3 phase separation resulted in a qualitatively correct prediction of the dependence of the rate of SO_2 oxidation on reactant partial pressures [192]. Similar agreement could not be achieved if a random distribution of SO_3 was assumed.

While lattice-gas models provide a sound theoretical basis for predicting the conditions under which island formation can occur, such models require knowledge of the strength of adsorbate–adsorbate interactions. Several authors have shown that many of the consequences of island formation can be explained using Langmuir–Hinshelwood models in which the presence of islands is postulated a-priori. An example of this approach is given by Barteau et al. [185], who simulated the isothermal oxidation of CO on a reconstructed Pt(100)-(5 × 20) surface. The rate of reaction between CO and preadsorbed O_2 was written as

$$r_r = k_r \theta_{CO} \theta_O^{1/2} \tag{6.8}$$

on the assumption that the reaction occurs solely at the perimeter of oxygen islands. An analytical solution to eq. (6.8) was obtained by writing species conservation equations and by

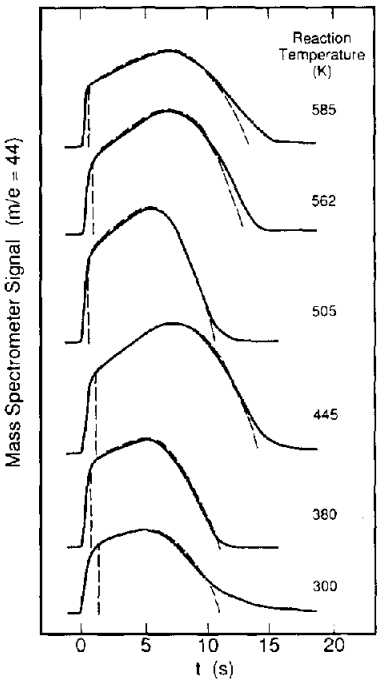

Fig. 47. Rate of CO_2 production versus t for the reaction of CO with preadsorbed oxygen for $P_{CO} = 1.0 \times 10^{-8}$ Torr and $\theta_O = 2/3$ monolayer [185]. Solid lines are the experimental results and the dashed lines are the model predictions.

assuming that the rates of CO adsorption and desorption were much greater than the rate of reaction. As can be seen in fig. 47, it is found that for a range of temperatures, the Langmuir–Hinshelwood model provides an adequate description of the reaction dynamics.

Mukesh et al. [193] have also investigated the oxidation of CO at the perimeter of islands. Two models were examined. In the first, it was assumed that CO_s aggregates into islands and is surrounded by O_s. If the number of CO islands is assumed to be constant, independent of CO coverage, then $r_r \propto \theta_O(\theta_{CO})^{1/2}$. In the second model, CO_s and O_s are assumed to form separate islands, and hence, $r_r \propto (\theta_O \theta_{CO})^{1/2}$. A comparison of the agreement between the CO islands model and experimental data obtained for supported Pt catalysts is shown in fig. 48. The authors note that a similar level of agreement could be achieved if both reactants were assumed to form islands.

The kinetics of H_2 reacting with preadsorbed oxygen on a Pt(111) surface have been modelled by Gland et al. [194]. Oxygen was assumed to form a regular array of islands. The rate of water formation was shown to depend on the size and shape of the oxygen islands as well as on the availability of atomic hydrogen in the peripheral region around each oxygen island. The model provides a qualitatively correct description of the high reaction rates observed at low oxygen coverages, as well as the first-order dependence of the reaction rate on the hydrogen flux to the surface.

TPSR spectra of CO and NO coadsorbed on Pt(100) have been simulated by Fink et al. [195]. The reaction mechanism was identical to that given earlier for NO reduction by CO, with the rate-limiting step assumed to be the dissociation of NO. A further assumption of the model was that CO and NO adsorb into mixed islands. The simulated TPSR spectra were in good agreement with the experimentally observed spectra. In particular, the model accurately

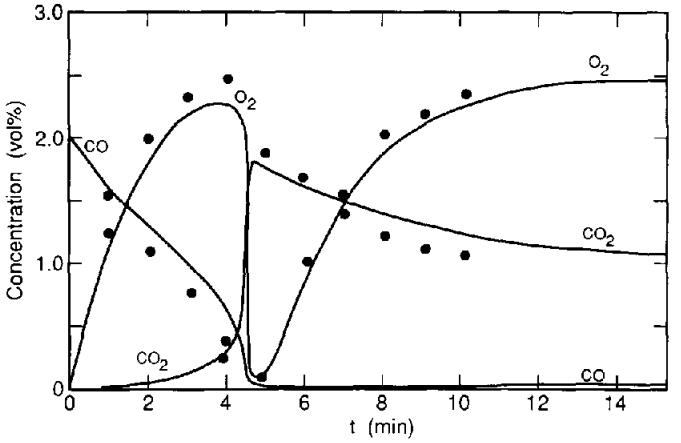

Fig. 48. Concentration profiles versus t for CO oxidation for an inlet step change from 2% CO to a 1% CO and 3% O_2 mixture [193]. Circles are the experimental data and the solid line is the model prediction.

predicted the narrowness of the CO_2 peak and the insensitivity of the peak position to equal coverages of coadsorbed CO and NO.

7. Concluding remarks

Considerable progress has been made in developing theoretical methods for predicting the dynamics of elementary processes occurring on metal surfaces. The starting point in all cases is a description of the potential governing the interactions between gas molecules and the atoms at the surface of the metal. At high adsorbate coverages, additional information must be supplied to describe the effects of adsorbate–adsorbate interactions. Accurate potential functions based on a quantum mechanical treatment of gas–metal interactions are not yet available and consequently, resort must be made to empirical potential functions. While such functions can be constructed in an ad-hoc fashion, there do not appear to be generally accepted criteria for establishing the suitability of such functions for dynamic calculations. At a minimum, it would seem that the potential function chosen should give the experimentally observed heat of adsorption and the vibrational frequency for adsorbate–metal vibrations in the ground state.

As noted in section 2, both classical and quantum descriptions of the dynamics of gas–metal interactions have been developed. At this time, only the classical approaches offer a way of predicting rate and diffusion coefficients for a wide range of processes and adsorbed species. Direct simulation of molecular dynamics is practical provided that the process of interest is $\sim 10^3$ times slower than the time constant for the fastest mode of motion (e.g., vibration). Experience has shown that molecular dynamics simulation provides estimates of the diffusion coefficient and of the sticking coefficient for dissociative adsorption of diatomic molecules that are in good quantitative agreement with experiment. By use of either MD or stochastic (Langevin) dynamics, it is also possible to include the effects of lattice vibrations. Where this has been done, it has been found that lattice vibrations slightly increase the calculated values of the sticking and diffusion coefficients.

The constraints of molecular dynamics with respect to describing the dynamics of infrequent events for which the time constants are $> 10^{-9}$ s can be overcome through the use of

dynamically corrected TST. This approach provides a rigorously correct theoretical framework for calculating rate and diffusion coefficients. Dynamically corrected TST provides a rational basis for identifying conditions under which precursor states affect the adsorption and desorption of adsorbates. Calculations of diffusion coefficients and rate coefficients for desorption obtained by means of dynamically corrected TST show good quantitative agreement with experimental measurements. Moreover, this theoretical approach explains why desorption rate coefficients exhibit a deviation from Arrhenius behavior at high temperatures, and why the rate coefficients for the desorption of molecular species are a factor of 100–1000 larger than those for the desorption of atomic species.

Absolute rate theory is useful only for crude estimation of pre-exponential factors, in as much as ad-hoc assumptions regarding the transition-state structure are necessary in order to estimate partition functions. This represents a severe limitation which limits the accuracy of the estimates of the pre-exponential factor to within a factor of 10 to 10^3.

Several theoretical models based on quantum mechanics have been developed. Such models can include the exchange of energy between the adsorbate and the surface as well as the effects of barrier tunneling and reflection. For small molecules and atoms (e.g., H_2 and H), quantum effects such as barrier tunneling and reflection are observed. For more massive adsorbates, quantum effects are projected to be less important.

The effects of lateral interactions can be neglected at low adsorbate coverages but can become significant at higher coverages. Such interactions can alter both the spatial distribution of adsorbates on a metal surface and the apparent activation energy barriers. To date, only empirical or semi-empirical representations of lateral interactions have been developed which are capable of describing rate or diffusion coefficients for a wide range of surface processes and adsorbate coverages. The simplest and the most frequently used approach is to treat lateral interactions by a sum of pairwise-additive contributions to the activation energy. With this approach, both the magnitude and sign of the interaction are treated as adjustable parameters. An alternative technique for describing lateral interactions is the BOC-MP method. In this case, interactions between adsorbates arise as a consequence of through-metal and direct adsorbate–adsorbate interactions.

Analytical expressions for the kinetics of adsorption, diffusion, desorption, and reaction in the presence of lateral interactions can be written using a lattice-gas model with the quasi-chemical approximation. While this approach captures the effects of lateral interactions, the lattice-gas model requires two rather restrictive assumptions. The first is that lateral interactions can be represented by a sum of pairwise contributions of equivalent strength and the second is that adsorbates always maintain an equilibrium configuration on the metal surface.

An alternative approach to account for the effects of lateral interactions is to incorporate the energetics predicted either from the sum of pairwise-additive contributions or from the BOC-MP method into Monte Carlo simulations. The Monte Carlo models treat the kinetics of surface processes in terms of probabilities which are specific to each site and its local environment, and thus require no assumptions about the distribution of adsorbates on the surface.

The present review has shown that both continuum and Monte Carlo models account for the experimentally observed kinetics of surface processes. The temperature-programmed desorption and reaction of adsorbates on metal surfaces can also be described with these techniques. Proper representation of lateral interactions has led to the conclusion that the appearance of multiple peaks in TPD and TPSR spectra are a consequence of such interactions.

Both continuum and Monte Carlo models have been used to describe the effects of island formation on the dynamics of surface reactions. Continuum models require assumptions to be

made about the number, size, and shape of the islands. Such models have been successful, though, in representing the effects of adsorbate islands on reaction dynamics. By contrast, Monte Carlo models make no assumptions about the concentration of islands or their size and shape. To date, though, kinetics predicted with Monte Carlo models have not been compared extensively with experimental observation.

Theoretical methods for predicting rate coefficients for other than very simple surface reactions have yet to be developed. The principal difficulty is the absence of accurate methods for generating the relevant potential energy hypersurface. Should it become possible to generate such functions, then the desired rate coefficients could be calculated using dynamically corrected TST. For reactions involving the removal or addition of a hydrogen atom, quantum effects might be expected to be important.

It is evident from this review that theoretical methods are now available for explaining many of the phenomena observed when gases interact with metal surfaces. One area for future research is the development of realistic potential hypersurfaces for describing surface reactions. Such calculations should preferably be based on ab-initio quantum chemical methods, to the extent possible. Another area that should be considered is the influence of adsorbate coverage on the reconstruction of metal surfaces and the effects of surface reconstruction on the dynamics of elementary processes occurring on metal surfaces. Finally, the suitability of stochastic models for describing reaction kinetics over a wide range of conditions should be explored more fully.

Acknowledgment

This work was supported by the Director, Office of Energy Research, Office of Basic Energy Science, Chemical Sciences Division of the US Department of Energy under contract DE-AC03-76SF00098.

Nomenclature

A, A_2, B, AB	Adsorbates
A^*, A_2^*	Precursor species
A_s	Chemisorbed species
A–A	Adsorbate–adsorbate interaction
a	Morse potential parameter
a_s	Area per reaction site
C	Concentration
$D(\theta)$	Fickian diffusion coefficient
D_{AB}	Dissociation energy of AB
D^C	Diffusion coefficient defined by eq. (2.71)
D_0	Pre-exponential factor for diffusion
D^T	Tracer diffusion coefficient
E	Activation energy
E_a	Activation energy for adsorption
E_d	Activation energy for desorption
E_{diff}	Activation energy for diffusion
E_{diff}^T	Activation energy for tracer diffusion

E_{diss}	Activation energy for dissociation
E_r	Activation energy for reaction
E_s	Lateral interaction energy
E^0	Activation energy in the absence of lateral interactions
E_a^0	Activation energy for adsorption in the absence of lateral interactions
E_d^0	Activation energy for desorption in the absence of lateral interactions
E_r^0	Activation energy for reaction in the absence of lateral interactions
$E^\dagger$	Energy of the transition state
E_0	Energy of the reactant
E_T	Incident kinetic translational energy
F	Flux of adsorbate
f_r	Correction factor for reaction due to lateral interactions
f_s	Dynamical correction factor in TST
f_a', f_a''	Correction factors for adsorption due to lateral interactions
f_d', f_d'	Correction factors for desorption due to lateral interactions
G	Normalization constant
H	Classical Hamiltonian
$\boldsymbol{H}$	Quantum Hamiltonian operator
h	Planck's constant
J	Diffusive flux
K	$= k_a^*/k_d^*$
k	Rate coefficient
k_b	Boltzmann constant
k_a	Rate coefficient for adsorption
$k_d^{(\alpha)}$	Rate coefficient for desorption
k_{TST}	Rate coefficient from TST
k_a^*	Rate coefficient for adsorption from the precursor state
k_d^*	Rate coefficient for desorption from the precursor state
L	$= r_d^*/(r_a^{**} + r_d^{**})$
l	Effective length of an adsorbate
M–A	Metal–adsorbate interaction
m	Molecular weight or mass of an adsorbate
m_B	Molecular weight of species B
m_i	Number of adsorbates bonded to ith metal atom
m_1	Number of nearest neighbors
m'	Mass of a surface atom
N	Normalization constant
N_d	Number of species which desorb
N_s	Number of surface metal atoms
n	Number of metal atoms bonded to an adsorbate
n_1	Number of nearest neighbors
n_2	Number of next-nearest neighbors
P	Probability
$P(\boldsymbol{p}, \boldsymbol{q})$	Probability density in phase space
P_B	Pressure of species B
$P_n(t)$	Probability of finding an adsorbate in state n at time t
P_{AA}	Probability that two nearest-neighbor sites are occupied by A

$P_{AA;n_1,m_1}$	Probability that two nearest-neighbor sites are occupied by A atoms such that one atom is surrounded by n_1 nearest neighbors and the other atom is surrounded by m_1 nearest neighbors
P_{AV}	Probability that of two nearest-neighbor sites, one is occupied by A and the other is vacant
P_{VV}	Probability that two nearest-neighbor sites are vacant
P_{A,n_1}	Probability that a site occupied by A has n_1 nearest neighbors
$P_{AB;i}$	Probability that a pair of sites occupied by A and B has the environment i
P_i	Probability of desorption from the ith site
P_{ij}	Probability of diffusion from site i to site j
$\boldsymbol{p}$	Momentum
Q, Q_i	Heat of adsorption
Q^0	Heat of adsorption in the absence of lateral interactions
Q_{0A}	Heat of adsorption of A in the on-top position
$Q_{A,n}$	Heat of adsorption of A as a function of coordination
$Q_{A,n}^{(1)}$	Heat of adsorption of A due to M–A interactions
$Q_{A,n}^{(2)}$	Heat of adsorption of A due to A–A interactions
$Q_{A,n}^*$	Total heat of adsorption of A
$\boldsymbol{q}$	Position
q_0	Partition function for adsorbates in the reactant state
$q^\dagger$	Partition function for adsorbates in the transition state
R	Random number
$\boldsymbol{R}$	Random force
r, r_i	Distance
r_a	Rate of adsorption
r_d	Rate of desorption
r_0	Equilibrium bond distance
r_r	Rate of reaction
S	Dividing plane
$S^{(\alpha)}(\theta)$	Sticking coefficient
$S^{(\alpha)}(0)$	Sticking coefficient at zero coverage
$S_0^{(\alpha)}$	Pre-exponential factor for adsorption
S_0	Reactive sticking coefficient
s	Reaction coordinate
s_0	Location of the dividing plane
T	Temperature
T_c	Critical temperature
T_s	Temperature of the surface
t	Time
u_0	Velocity required for an adsorbate located at s_0 to desorb
V	Potential
V_{0A}	Equilibrium energy
V_p	Interaction potential in the primary zone
V_s	Interaction potential in the secondary zone
v	Mean velocity
v_s	Velocity in the s direction
W	Potential of mean force
$\boldsymbol{W}$	Matrix of transition probabilities

w_{AA}	Interaction energy between an AA pair
x, x_i	Bond order
x_p	Position in the primary zone
$\boldsymbol{Y}$	Adsorbate trajectory
z	Number of nearest-neighbor sites or distance
α	Order of a rate process
β	Heating rate
Γ, Γ_{ij}	Hopping frequency
γ	Bending angle
γ_0	Maximum bending angle
δ_{ij}	A–A bond order
ϵ	Lennard-Jones parameter
ζ	Trapping probability
η	$2[1-\exp(-w_{AA})/k_bT]$
Θ	Memory kernel
θ	Coverage
θ_A^0	Initial coverage of A
θ_V	Coverage of vacant sites
θ_i	Angle of incidence from the surface normal
λ	Mean-free path or mean-free hopping length
μ	Chemical potential
μ_i	Reduced mass of species i
μ_r	Reduced mass for rotation
$\nu_d^{(\alpha)}$	Pre-exponential factor for desorption
ν_{diff}^T	Pre-exponential factor for hopping
ν_r	Pre-exponential factor for reaction
ξ	Correction factor in TST
ρ_i	Dimensionless quantity (see eqs. (2.77)–(2.79))
ρ_{ij}	Coulomb integral
σ	Lennard-Jones parameter
τ	Time
ϕ	Coefficient for describing how E varies with total coverage
χ_{ij}	Exchange integral
ψ	Wave function
Ω_0	Vibration frequency of an adsorbate at the bottom of the potential well
Ω_r	Rotational frequency
ω_{pp}	Vibration frequency for the metal atoms in the primary zone

References

[1] M.A. Morris, M. Bowker and D.A. King, in: Simple Processes at the Gas–Solid Interface, Comprehensive Chemical Kinetics, Eds. C.H. Bamford, C.F.H. Tipper and R.G. Compton (Elsevier, Amsterdam, 1984) ch. 1.

[2] G. Ertl, in: Catalysis, Science and Technology, Vol. 4, Eds. J.R. Anderson and M. Boudart (Springer, Berlin, 1983) ch. 3.

[3] G.A. Somorjai, Chemistry in Two Dimensions: Surfaces (Cornell University Press, Ithaca, NY, 1981).

[4] W.H. Weinberg, in: Dynamics of Gas–Surface Collisions, Eds. M.N.R. Ashfold and C.T. Rettner (Royal Society of Chemistry, Cambridge, 1991).

[5] (a) G. Ehrlich and K. Stolt, Ann. Rev. Phys. Chem. 31 (1980) 603;
(b) G. Ehrlich, CRC Crit. Rev. Solid State Mater. Sci. 10 (1982) 391.
[6] A.G. Naumovets and Yu.S. Medula, Surf. Sci. Rep. 4 (1985) 365.
[7] R.C. Baetzold, in: Reaction Energetics on Metal Surfaces: Theory and Applications, Ed. E. Shustorovich (Springer, Berlin, in press) ch. 3.
[8] A. Kapoor, R.T. Yang and C. Wong, Catal. Rev.-Sci. Eng. 31 (1989) 129.
[9] L.D. Schmidt, Catal. Rev.-Sci. Eng. 9 (1974) 115.
[10] D.A. King, Surf. Sci. 47 (1975) 384.
[11] R.J. Madix, in: The Chemical Physics of Solid Surfaces and Heterogeneous Catalysis, Vol. 4, Eds. D.A. King and D.P. Woodruff (Elsevier, Amsterdam, 1982) ch. 1.
[12] J.C. Tully, Annu. Rev. Phys. Chem. 31 (1980) 319.
[13] S.A. Adelman and J.D. Doll, Acc. Chem. Res. 10 (1977) 378.
[14] J.D. Doll and A.F. Voter, Annu. Rev. Phys. Chem. 38 (1987) 413.
[15] A.T. Bell, in: Reaction Energetics on Metal Surfaces: Theory and Applications, Ed. E. Shustorovich (Springer, Berlin, in press) ch. 3.
[16] For example, see refs. [34–37,46].
[17] T.B. Grimley, in: The Chemical Physics of Solid Surfaces and Heterogeneous Catalysis, Vol. 2, Eds. D.A. King and D.P. Woodruff (Elsevier, Amsterdam, 1983) ch. 5.
[18] T.B. Grimley, in: The Nature of the Surface Chemical Bond, Eds. T.N. Rhodin and G. Ertl (North-Holland, Amsterdam, 1979) ch. 1.
[19] E. Shustorovich, Surf. Sci. Rep. 6 (1986) 1.
[20] E. Shustorovich, Acc. Chem. Res. 21 (1988) 189.
[21] E. Shustorovich, in: Advances in Catalysis, Vol. 37, Eds. D.D. Eley, H. Pines and P.B. Weisz (Academic Press, New York, 1990) p. 101.
[22] W.H. Weinberg, in: Springer Series in Surface Sciences, Vol. 8, Eds. M. Grunze and H.J. Kreuzer (Springer, Berlin, 1987) p. 94.
[23] R. Gorte and L.D. Schmidt, Surf. Sci. 76 (1978) 559.
[24] A. Cassuto and D.A. King, Surf. Sci. 102 (1981) 388.
[25] P.J. Kisliuk, J. Phys. Chem. Solids 3 (1957) 95; 5 (1958) 78.
[26] D.A. King, Surf. Sci. 64 (1977) 43.
[27] K. Schönhammer, Surf. Sci. 83 (1979) L633.
[28] V.P. Zhdanov, Surf. Sci. 102 (1981) L35.
[29] V.P. Zhdanov, Surf. Sci. 111 (1981) 63.
[30] V.P. Zhdanov, Surf. Sci. 111 (1981) L662.
[31] V.P. Zhdanov, Surf. Sci. 209 (1989) 523.
[32] D.A. King and M.G. Wells, Proc. R. Soc. London A 339 (1974) 245.
[33] D.A. Reed and G. Ehrlich, Surf. Sci. 102 (1981) 588.
[34] V.P. Zhdanov, (a) Surf. Sci. 149 (1985) L13; (b) Surf. Sci. 194 (1988) 1.
[35] S.A. Adelman and J.D. Doll, J. Chem. Phys. 61 (1974) 4242; 62 (1975) 2518; 64 (1976) 2375.
[36] E.K. Grimmelmann, J.C. Tully and E. Helfand, J. Chem. Phys. 74 (1981) 5300.
[37] J.C. Tully, Surf. Sci. 111 (1981) 461.
[38] A. Gelb and M.J. Cardillo, Surf. Sci. 59 (1976) 128; Surf. Sci. 64 (1977) 197.
[39] A. Gelb and M.J. Cardillo, Surf. Sci. 75 (1978) 199.
[40] C. Chiang and B. Jackson, J. Chem. Phys. 87 (1987) 5497.
[41] C. Lee and A.E. DePristo, J. Chem. Phys. 85 (1986) 4161.
[42] C. Lee and A.E. DePristo, J. Chem. Phys. 87 (1987) 1401.
[43] C. Lee and A.E. DePristo, J. Vac. Sci. Technol. A 5 (1987) 485.
[44] D.J. Doren and J.C. Tully, Langmuir 4 (1988) 256.
[45] D. Chandler, J. Chem. Phys. 68 (1978) 2959.
[46] A.F. Voter and J.D. Doll, J. Chem. Phys. 82 (1985) 80.
[47] V.P. Zhdanov, J. Pavlicek and Z. Knor, Catal. Rev.-Sci. Eng. 30 (1988) 501.
[48] O.V. Krylov, M.U. Kisliuk, B.R. Shub, A.A. Gezalov, N.D. Maksimova and Y.N. Rufov, Kinet. Katal. 13 (1972) 598.
[49] R.C. Baetzold and G.A. Somorjai, J. Catal. 45 (1976) 94.
[50] K.J. Laidler, S. Glasstone and H. Eyring, J. Chem. Phys. 8 (1940) 659; 8 (1940) 667.
[51] Y. Zeiri, A. Redondo and W.A. Goddard III, Surf. Sci. 131 (1983) 221; 136 (1984) 41; J. Vac. Sci. Technol. B 2 (1984) 550.

[52] H.A. Kramers, Physica 7 (1940) 284.
[53] B. Jackson and H. Metiu, J. Chem. Phys. 86 (1987) 1026.
[54] S. Efrima, C. Jedrzejek, K.F. Freed, E. Hood and H. Metiu, J. Chem. Phys. 79 (1983) 2436.
[55] E. Hood, C. Jedrzejek, K.F. Freed and H. Metiu, J. Chem. Phys. 81 (1984) 3277.
[56] K.F. Freed, J. Chem. Phys. 82 (1985) 5264.
[57] C.R. Arumainayagam, R.J. Madix, M.C. McMaster, V.M. Suzawa and J.C. Tully, Surf. Sci. 226 (1990) 180.
[58] C.W. Muhlhausen, L.R. Williams and J.C. Tully, J. Chem. Phys. 83 (1985) 2594.
[59] I. NoorBatcha, L.M. Raff and D.L. Thompson, J. Chem. Phys. 81 (1984) 3715.
[60] M. Balooch, M.J. Cardillo, D.R. Miller and R.E. Stickney, Surf. Sci. 46 (1974) 358.
[61] M.J. Cardillo, M. Balooch and R.E. Stickney, Surf. Sci. 50 (1975) 263.
[62] A.V. Hamza and R.J. Madix, J. Phys. Chem. 89 (1985) 5381.
[63] H.J. Robota, W. Vielhaber, M.C. Lin, J. Segner and G. Ertl, Surf. Sci. 155 (1985) 101.
[64] A. Kara and A.E. DePristo, Surf. Sci. 193 (1988) 437.
[65] H.E. Pfnür, C.T. Rettner, J. Lee, R.J. Madix and D.T. Auerbach, J. Chem. Phys. 85 (1986) 7452.
[66] T. Truong, G. Hancock and D.G. Truhlar, Surf. Sci. 214 (1989) 523.
[67] J.E. Adams and J.D. Doll, Surf. Sci. 103 (1981) 472; 111 (1981) 492.
[68] M. Asscher, O.M. Becker, G. Haase and R. Kosloff, Surf. Sci. 206 (1988) L880.
[69] C.T. Rettner and H. Stein, Phys. Rev. Lett. 59 (1987) 2768.
[70] U. Nielsen, D. Halstead, S. Holloway and J.K. Nørskov, J. Chem. Phys. 93 (1990) 2879.
[71] J.K. Nørskov, J. Chem. Phys. 90 (1989) 7461.
[72] G. Auger, A. Winkler and K.D. Redulic, Surf. Sci. 220 (1989) 1.
[73] B.E. Hayden and C.L. Lambert, (a) Chem. Phys. Lett. 160 (1989) 331; (b) Phys. Rev. Lett. 63 (1989) 1823.
[74] E.S. Hood, B.H. Toby and W.H. Weinberg, Phys. Rev. Lett. 55 (1985) 2437.
[75] P. Feulner and D. Menzel, Phys. Rev. B 25 (1982) 4295.
[76] D. Menzel, H. Pfnür and P. Feulner, Surf. Sci. 126 (1983) 374.
[77] H.K. McDowell and J.D. Doll, J. Chem. Phys. 78 (1983) 3219.
[78] J.D. Doll and H.K. McDowell, J. Chem. Phys. 77 (1982) 479.
[79] J.D. Doll and H.K. McDowell, Surf. Sci. 123 (1982) 99.
[80] H.K. McDowell and J.D. Doll, Surf. Sci. 121 (1982) L537.
[81] D.W. Bassett and M.J. Parsley, Brit. J. Appl. Phys. 2 (1969) 13.
[82] G. Ayrault and G. Ehrlich, J. Chem. Phys. 60 (1974) 281.
[83] P. Cowan and T.T. Tsong, Phys. Lett. A 53 (1975) 383.
[84] W.R. Graham and G. Ehrlich, Thin Solid Films 25 (1975) 85; Phys. Rev. Lett. 31 (1973) 1407.
[85] P.P. Cowan and T.T. Tsong, 22nd Int. Field Emission Symp., Atlanta, 1975.
[86] P.G. Flahive and W.R. Graham, Surf. Sci. 91 (1980) 463.
[87] J.D. Doll and D.L. Freeman, Surf. Sci. 134 (1983) 769.
[88] R.L. Palmer, J. Vac. Sci. Technol. 12 (1975) 1403.
[89] M.T. Martin and J.B. Hudson, J. Vac. Sci. Technol. 15 (1978) 474.
[90] S.M. Levine and S.H. Garofalini, Surf. Sci. 167 (1986) 198.
[91] H.C. Abbink, R.M. Broudy and G.P. McCarthy, J. Appl. Phys. 39 (1968) 4673.
[92] A.F. Voter and J.D. Doll, J. Chem. Phys. 82 (1985) 80.
[93] S.M. Valone, A.F. Voter and J.D. Doll, Surf. Sci. 155 (1985) 687.
[94] J.G. Lauderdale and D.G. Truhlar, Surf. Sci. 164 (1985) 558.
[95] S.M. Valone, A.F. Voter and J.D. Doll, J. Chem. Phys. 85 (1986) 7480.
[96] J.G. Lauderdale and D.G. Truhlar, J. Chem. Phys. 84 (1986) 1843.
[97] T.N. Truong and D.G. Truhlar, J. Phys. Chem. 91 (1987) 6229.
[98] T.N. Truong and D.G. Truhlar, J. Chem. Phys. 88 (1988) 6611.
[99] C.H. Mak and S.M. George, Chem. Phys. Lett. 135 (1987) 381.
[100] T.N. Truong, D.G. Truhlar, J.R. Chelikowsky and M.Y. Chou, J. Phys. Chem. 94 (1990) 1973.
[101] C.H. Mak, J.L. Brand, A.A. Deckert and S.M. George, J. Chem. Phys. 85 (1986) 1676.
[102] A. Auerbach, K.F. Freed and R. Gomer, J. Chem. Phys. 86 (1987) 2356.
[103] R. DiFoggio and R. Gomer, Phys. Rev. B 25 (1982) 3490.
[104] S.C. Wang and R. Gomer, J. Chem. Phys. 83 (1985) 4193.
[105] K.B. Whaley, A. Nitzan and R.B. Gerber, J. Chem. Phys. 84 (1986) 5181.
[106] M. Metropolis, A.W. Rosenbluth, A.N. Teller and E. Teller, J. Chem. Phys. 21 (1953) 1087.
[107] K. Kawasaki, Phys. Rev. B 145 (1966) 224; 148 (1966) 375; 150 (1966) 285.
[108] H.C. Kang and W.H. Weinberg, J. Chem. Phys. 90 (1989) 2824.

[109] M. Bowker and D.A. King, Surf. Sci. 71 (1978) 583.
[110] M. Bowker and D.A. King, Surf. Sci. 72 (1978) 208.
[111] R. Butz and G. Wagner, Surf. Sci. 63 (1977) 448.
[112] M. Tringides and R. Gomer, Surf. Sci. 145 (1984) 121.
[113] J.R. Chen and R. Gomer, Surf. Sci. 79 (1979) 413.
[114] A. Sadiq and K. Binder, Surf. Sci. 128 (1983) 350.
[115] C.H. Mak, H.C. Andersen and S.M. George, J. Chem. Phys. 88 (1988) 4052.
[116] T. Engel and R. Gomer, J. Chem. Phys. 52 (1970) 5572.
[117] B.E. Nieuwenhuys, D.Th. Meijer and W.M.H. Sachtler, Phys. Status Solidi (a) 24 (1974) 115.
[118] R.J. Gorte, L.D. Schmidt and J.L. Gland, Surf. Sci. 109 (1981) 367.
[119] L.M. Raff, I. NoorBatcha and D.L. Thompson, J. Chem. Phys. 85 (1986) 3081.
[120] K.D. Brzoska and Ch. Kleint, Thin Solid Films 34 (1976) 131.
[121] Yu.I. Belyakov, N.I. Ionov and T.N. Kompaniets, Sov. Phys. Solid State A 1 (1973) 2567.
[122] G. Schulze and M. Henzler, Surf. Sci. 124 (1983) 336.
[123] L. Schmidt and R. Gomer, J. Chem. Phys. 42 (1965) 3573.
[124] L.M. Kahn and S.C. Ying, Solid State Commun. 16 (1975) 799.
[125] G. Ehrlich, in: Advances in Catalysis, Vol. 14, Eds. D.D. Eley, H. Pines and P.B. Weisz (Academic Press, New York, 1963) p. 255.
[126] C.R. Helms and R.J. Madix, Surf. Sci. 52 (1975) 677.
[127] J.E. Lennard-Jones and C. Strachan, Proc. R. Soc. London A 150 (1935) 442.
[128] C. Strachan, Proc. R. Soc. London A 150 (1935) 456.
[129] J.E. Lennard-Jones and A.F. Devonshire, Proc. R. Soc. London A 156 (1936) 6, 29; 158 (1937) 242, 253.
[130] A.F. Devonshire, Proc. R. Soc. London A 156 (1936) 37; 158 (1937) 269.
[131] J.E. Lennard-Jones and A.F. Devonshire, Nature 137 (1936) 1069.
[132] F.O. Goodman, Surf. Sci. 24 (1971) 667.
[133] G.S. De, U. Landman and M. Rasolt, Phys. Rev. B 21 (1980) 3256.
[134] C.G. Goymour and D.A. King, J. Chem. Soc. Faraday Trans. I, 6 (1973) 749.
[135] C.G. Goymour and D.A. King, J. Chem. Soc. Faraday Trans. I, 6 (1973) 736.
[136] V.P. Zhdanov, Surf. Sci. 123 (1982) 106.
[137] J.L. Taylor and W.H. Weinberg, Surf. Sci. 78 (1978) 259.
[138] J.L. Taylor, D.E. Ibbotson and W.H. Weinberg, Surf. Sci. 79 (1979) 349.
[139] A.H. Smith, R.A. Barker and P.J. Estrup, Surf. Sci. 136 (1984) 327.
[140] A.V. Myshlyavtsev and V.P. Zhdanov, J. Chem. Phys. 92 (1990) 3909.
[141] S. Sundaresan and K.R. Kaza, Surf. Sci. 160 (1985) 103.
[142] S.J. Lombardo and A.T. Bell, Surf. Sci. 206 (1988) 101.
[143] J.L. Sales and G. Zgrablich, Phys. Rev. B 35 (1987) 9520.
[144] A. Córdoba and J.J. Luque, Phys. Rev. B 26 (1982) 4028.
[145] J.L. Sales, G. Zgrablich and V.P. Zhdanov, Surf. Sci. 209 (1989) 208.
[146] H.R. Han and L.D. Schmidt, J. Phys. Chem. 75 (1971) 227.
[147] P.J. Estrup, Department of Chemistry, Brown University, unpublished results.
[148] D. Gupta and C.S. Hirtzel, Chem. Phys. Lett. 149 (1988) 527; Surf. Sci. 210 (1989) 322.
[149] S.J. Lombardo and A.T. Bell, Surf. Sci. 224 (1989) 451.
[150] E.I. Ko, Department of Chemical Engineering, Carnegie-Mellon University, unpublished results.
[151] J. Benziger and R.J. Madix, Surf. Sci. 94 (1980) 119.
[152] J.M. White, J. Phys. Chem. 87 (1983) 915.
[153] Y. Kim, H.C. Peebles and J.M. White, Surf. Sci. 114 (1982) 363.
[154] A.K. Galwey, in: Advances in Catalysis, Vol. 26, Eds. D.D. Eley, H. Pines and P.B. Weisz (Academic Press, New York, 1977) p. 247.
[155] H.C. Kang, T.A. Jachimowski and W.H. Weinberg, J. Chem. Phys., to be published.
[156] E.G. Seebauer, A.C.F. Kong and L.D. Schmidt, Surf. Sci. 193 (1988) 417.
[157] M. Alnot and A. Cassuto, Surf. Sci. 112 (1981) 325.
[158] P.J. Estrup, E.F. Greene, M.J. Cardillo and J.C. Tully, J. Phys. Chem. 90 (1986) 4099.
[159] J.B. Miller, H.R. Siddiqui, S.M. Gates, J.N. Russell, Jr., J.T. Yates, Jr., J.C. Tully and M.J. Cardillo, J. Chem. Phys. 87 (1987) 6725.
[160] D.W. Goodman, D.E. Peebles and J.M. White, Surf. Sci. 140 (1984) L239.
[161] H. Peled and M. Asscher, Surf. Sci. 183 (1987) 201.
[162] W.H. Weinberg, Surf. Sci. 128 (1983) L224.

[163] M. Bowker, M.A. Barteau and R.J. Madix, Surf. Sci. 92 (1980) 528.
[164] T.W. Root, L.D. Schmidt and G.B. Fisher, Surf. Sci. 134 (1983) 30.
[165] P. Ho and J.M. White, Surf. Sci. 137 (1984) 103.
[166] C.M. Comrie, W.H. Weinberg and R.M. Lambert, Surf. Sci. 57 (1976) 619.
[167] M.E. Bridge and R.M. Lambert, Proc. R. Soc. London A 370 (1980) 545.
[168] H. Conrad, G. Ertl, J. Küppers and E.E. Latta, Surf. Sci. 50 (1975) 296.
[169] P.D. Reed, C.M. Comrie and R.M. Lambert, Surf. Sci. 72 (1978) 423.
[170] J.L. Taylor, D.E. Ibbotson and W.H. Weinberg, Surf. Sci. 90 (1979) 37.
[171] V.P. Zhdanov, Surf. Sci. 137 (1984) 515.
[172] V.P. Zhdanov, Surf. Sci. 169 (1986) L278.
[173] J. Küppers and A. Plagge, Z. Naturforsch. 34a (1979) 81.
[174] V.P. Ivanov, G.K. Boreskov, V.I. Savchenko, V.L. Tataurov, W.H. Weinberg and W.F. Egelhoff, Dokl. Akad. Nauk SSSR 249 (1979) 622 (in Russian).
[175] V.P. Zhdanov, Surf. Sci. 169 (1986) 1.
[176] V.A. Sobyanin, G.K. Boreskov and A.R. Cholach, Dokl. Akad. Nauk SSSR 278 (1984) 1422 (in Russian).
[177] S. Sundaresan and K.R. Kaza, Chem. Eng. Commun. 35 (1985) 1.
[178] S.H. Oh, G.B. Fisher, J.E. Carpenter and D.W. Goodman, J. Catal. 100 (1986) 360.
[179] C.T. Campbell, S.-K. Shi and J.M. White, Appl. Surf. Sci. 2 (1979) 382.
[180] C.T. Campbell and J.M. White, J. Catal. 54 (1978) 289.
[181] P.A. Thiel, E.D. Williams, J.T. Yates, Jr. and W.H. Weinberg, Surf. Sci. 84 (1979) 54.
[182] T.W. Root, G.B. Fisher and L.D. Schmidt, Surf. Sci. 150 (1985) 173.
[183] C.T. Campbell and J.M. White, Appl. Surf. Sci. 1 (1978) 347.
[184] T.W. Root, G.B. Fisher and L.D. Schmidt, J. Chem. Phys. 85 (1986) 4679.
[185] M.A. Barteau, E.I. Ko and R.J. Madix, Surf. Sci. 104 (1981) 161.
[186] M. Silverberg, A. Ben-Shaul and F. Rebentrost, J. Chem. Phys. 83 (1985) 6501.
[187] M. Silverberg and A. Ben-Shaul, J. Chem. Phys. 87 (1987) 3178.
[188] M. Silverberg and A. Ben-Shaul, Chem. Phys. Lett. 134 (1987) 491.
[189] M. Silverberg and A. Ben-Shaul, Surf. Sci. 214 (1989) 17.
[190] M. Silverberg and A. Ben-Shaul, J. Stat. Phys. 52 (1988) 1179.
[191] K.R. Kaza and S. Sundaresan, Chem. Eng. Commun. 32 (1985) 333.
[192] C.G. Vayenas and H.M. Saltsburg, J. Catal. 57 (1979) 206.
[193] D. Mukesh, W. Morton, C.N. Kenney and M.B. Cutlip, Surf. Sci. 138 (1984) 237.
[194] J.L. Gland, G.B. Fisher and E.B. Kollin, J. Catal. 77 (1982) 263.
[195] Th. Fink, J.-P. Dath, M.R. Bassett, R. Imbihl and G. Ertl, Vacuum, to be published.